EPFL

Thèse n° 9206

Soft functional fibers for mechanical sensing and actuation

Présentée le 16 septembre 2021

Faculté des sciences et techniques de l'ingénieur
Laboratoire des fibres et matériaux photoniques
Programme doctoral en science et génie des matériaux

pour l'obtention du grade de Docteur ès Sciences

par

Andreas LEBER

Acceptée sur proposition du jury

Prof. V. Michaud, présidente du jury
Prof. F. Sorin, directeur de thèse
Prof. M. Kolle, rapporteur
Dr S. Danto, rapporteur
Prof. H. Shea, rapporteur

École polytechnique fédérale de Lausanne

2021

To my family.

Acknowledgements

During my time at EPFL, I have had the chance to meet and learn from many inspiring people.

First, I would like to thank Professor Fabien Sorin. Throughout my entire PhD journey, he has been an excellent advisor, who guided me with enthusiasm and clear insights when I needed it, but also trusted me to steer the research in the directions that I was most interested in. He also got me involved in many exciting activities, such as the teaching of fundamental materials science and the collaboration with industrial partners. Most importantly, he has been a caring and supportive person. Thank you, Fabien!

I feel very lucky to have been part of the FIMAP lab, which brings together a group of interesting, happy, and crazy people, and I am thankful to all of them. Anne Roy for always helping us out. The FIMAP 'first gen', Tung Nguyen-Dang, Wei Yan, Alexis Page, Yunpeng Qu, and Federica Sordo, for teaching me everything about thermal drawing and creating the great atmosphere in the lab. Bastien Schyrr for his unique brand of humor. Tapajyoti Das Gupta for his kindness and insanity. Inès Richard for her contagious fondness of the mountains and skiing. Shahrzad Shadman for her, sometimes kind, sometimes brutal, honesty. Rajasundar Chandran for his amazing perspective on life and his strong desire to create things. Nicola Bartolomei for showing me the Lausanne life and being a true friend. My office mate Chaoqun Dong for her clever ideas, countless shared laughs, and for being there during all the highs and lows of research. And of course the 'next gen' of the lab William Esposito, Pierre-Luc Piveteau, Hritwick Banerjee, Xue Wan, and especially Stella Laperrousaz, who made an immense contribution to the work on nanocomposites. I am sure they will continue to make FIMAP a stimulating and fun place for research.

I would also like to extend my gratitude to all the other members of the EPFL community who have had a profound impact on my work. Professor Véronique Michaud and the members of the LPAC group, especially Yves Leterrier, Alexandre Mordasini, Damiano Salvatori, Adrien Demongeot, Raphaël Charvet, and Baris Çaglar, for helping me out with polymer processing and characterization. Professor Pedro Reis and Dong Yan for a fruitful collaboration on the mechanical analysis of soft fibers. Professor Farhad Rachidi-Haeri, Hamidreza Karami, Zhaoyang Wang, and Lukas Riemer for their invaluable support for reflectometry experiments. Professor Holger Frauenrath and the LMOM group, especially Nicolas Candeau and Michael Giffin, for their helpful input on polymer extrusion. The talented members of the ATMX and ATPR workshops, including Pierre-André Despont, Jean-Pierre Rougnon, and Yves Ruschetta. Professor Dirk Grundler, Chrystelle Demierre, and Anne Kolly for a great organization of the EDMX school, including stimulating events. Professor Jürgen Brugger and Professor Maartje Bastings for helpful advice on the research directions.

Finally, I would like to thank my family, without whom none of this would have been possible. My parents Manfred and Monika, who have always supported and encouraged me unconditionally. My brother Moritz, who so often has shown me the way and whom I can always count on. My partner in life Cécile, who is an endless source of strength and joy.

Soft functional fibers for mechanical sensing and actuation

Andreas Leber

Abstract

The measurement and generation of mechanical deformations is a key functionality in health monitoring, human–machine interaction, and soft robotics. However, current methods typically rely on small and hard transducers, which result in poor performance, cumbersome implementation, and incompatibility with the human body. An alternative approach consists of imparting functionality within long and soft fibers. However, the multi-material assemblies, which are required for advanced functionalities, are challenging to realize in fibers. Additionally, the 1-dimensional geometry of fibers, which stands in stark contrast to traditional 0-dimensional devices, requires novel schemes to extract meaningful information and induce targeted movements.

In this Thesis, four distinct innovations to fiber-based transducers are made, which are composed of soft materials and fabricated by the thermal drawing technique. The first three works are each aimed at one of the three conceptual elements of a sensor: the structural design, the constituting materials, and the signal processing. In the fourth work, actuation is coupled with sensing to develop robotic fibers.

(i) Considering the design element of a sensor first, fibers with an asymmetric elastomer architecture are developed, featuring several electrodes separated by an air gap. Compressive loads on the meter-long fibers result in the selective contacting of electrodes within the deformed fiber structure, triggering pronounced electrical signals at distinct pressure levels. This developed sensing concept enables the facile functionalization of large surfaces, demonstrated by a fiber-augmented gymnastic mat for the monitoring of human body position, posture, and motion. (ii) Focusing on the materials next, a novel polymer nanocomposite with carefully engineered rheological, mechanical, and electrical properties is introduced. In particular, controlled changes to the nanoparticle network and the intertwined electrical conduction of the material are explored – induced either by viscous flow during thermal drawing fiber fabrication or elastic deformation in applications. The nanocomposite represents a platform upon which a family of fiber devices can be developed. (iii) As the third pillar of sensing, signal processing is addressed by employing electrical reflectometry within microstructured elastomeric fibers that integrate tens of liquid metal conductors. Reflected electrical waves, triggered by multimodal deformations of the fiber structure, are investigated experimentally and theoretically. This unprecedented physical mechanism enables multiplexed measurements of the mode, magnitude, and position of multiple simultaneous pressing and stretching events. By integrating a single fiber with a single interface port into a larger fabric, the technique can be used to create an electronic textile that can decipher convoluted mechanical stimulation. (iv) Finally, both actuation and sensing schemes are combined, resulting in robotic fibers with closed-loop control. Thanks to three integrated tendons pulling on the distal fiber end, bending with two degrees of freedom is achieved. Envisioned as steerable

catheters, the fibers can autonomously avoid obstacles to minimize tissue damage, scan the environment to execute the best navigation path, and accurately deliver mechanical tools, fluids, as well as optical and electrical stimulation.

Key words: soft materials, thermoplastic elastomers, multi-material fibers, electromechanical sensors, soft electronics, smart textiles, actuators, robotics

Des fibres fonctionnelles souples comme capteurs mécaniques et actionneurs

Andreas Leber

Résumé

La mesure et la génération de déformations mécaniques est une fonctionnalité clé dans la surveillance de la santé, l'interaction homme-machine et la robotique molle. Les méthodes de transduction actuelles reposent généralement sur des éléments petits et durs, ce qui se traduit par des performances limitées, une mise en œuvre complexes et une incompatibilité avec le corps humain. Une autre approche consiste à intégrer des fonctionnalités dans des fibres longues et souples. Cependant, les assemblages multi-matériaux, qui sont nécessaires pour ces fonctionnalités avancées, sont difficiles à réaliser dans des fibres. En outre, la géométrie 1-dimensionnelle des fibres, qui contraste fortement avec les dispositifs traditionnels 0-dimensionnelles, nécessite de nouvelles méthodes pour extraire des informations significatives et induire des mouvements ciblés.

Dans cette Thèse, quatre innovations distinctes sont apportées aux transducteurs en forme de fibres, qui sont composés de matériaux mous et fabriqués par la technique du tirage à chaud. Les trois premiers projets visent chacun l'un des trois composants conceptuels d'un capteur : la structure, les matériaux constitutifs et le traitement du signal. Dans le quatrième projet, l'actionnement est couplé à la détection afin de développer des fibres robotiques.

(i) En considérant en premier la structure du capteur, des fibres avec une architecture élastomère asymétrique sont développées, qui contiennent plusieurs électrodes séparées par un espace d'air. Des contraintes de compression exercées sur les fibres entraînent le contact sélectif des électrodes dans la structure déformée, ce qui déclenche alors des signaux électriques prononcés à des niveaux de pression distincts. Ce concept de détection permet la fonctionnalisation de grandes surfaces, comme le démontre un tapis de gymnastique augmenté par des fibres pour la mesure de la position, de la posture et du mouvement du corps humain. (ii) Secondement, en examinant les matériaux, un nouveau nanocomposite polymère est présenté, qui se distingue par des propriétés définies de type rhéologique, mécanique et électrique. En particulier, les changements contrôlés du réseau de nanoparticules et sa conduction électrique sont explorés - induits soit par un écoulement visqueux pendant la fabrication par le tirage à chaud, soit par des déformations lors d'applications. Le nanocomposite représente une plateforme sur laquelle une famille de fibres fonctionnelles peut être développée. (iii) Le traitement du signal, comme troisième pilier de la détection, est abordé en utilisant la réflectométrie électrique dans des fibres élastomères microstructurées qui intègrent des conducteurs en métal liquide. Les ondes électriques réfléchies, déclenchées par des déformations multimodales de la structure de la fibre, sont étudiées expérimentalement et théoriquement. Ce mécanisme physique permet des mesures multiplexées du mode, de l'intensité et de la position de plusieurs événements simultanés de pression et d'étirement. En intégrant une seule fibre avec un seul port d'interface dans un tissu, cette technique peut être utilisée pour créer un textile électronique capable de déchiffrer des stimulations mécaniques

alambiquées. (iv) Finalement, des mécanismes d'actionnement et de détection sont combinés, ce qui permet de créer des fibres robotiques avec un contrôle en boucle fermée. Grâce à trois tendons intégrés tirant sur l'extrémité distale de la fibre, une flexion à deux degrés de liberté est obtenue. Conçues comme des cathéters orientables, les fibres peuvent éviter des obstacles de manière autonome afin de minimiser les dommages aux tissus, scanner l'environnement afin d'exécuter la meilleure trajectoire de navigation, et délivrer avec précision des outils mécaniques, des fluides, ainsi que des stimulations optiques et électriques.

Mots clefs : matériaux souples, élastomères thermoplastiques, fibres multi-matériaux, capteurs électromécaniques, électronique souple, textiles intelligents, actionneurs, robotique

Contents

Introduction

As we all know from observations of nature and our own bodies, soft materials assemblies can accomplish a large range of sophisticated functions. This includes sensing, for the perception of internal physical state and external environment, as well as actuation, for carrying out targeted movement. Yet, state-of-the-art machines and robots are constructed almost exclusively out of hard materials, such as metals, ceramics, and hard polymers. While this may change in the future, technology based on assemblies of many hard components is unrivaled at accomplishing precise tasks in controlled environments, such as a robotic arm in an assembly line. In some circumstances, however, hard devices are unsuitable and are outperformed by soft devices, which are constituted of soft materials such as elastomers or gels. In particular, when in intimate contact with the human body, encompassing biomedical applications and human-machine interfaces, soft systems constitute an attractive alternative, because they are comfortable and safe for users, as well as robust, low-cost, and adaptable to unpredictable changes of dynamic environments. However, soft devices, including both sensors and actuators, are still in an early stage of their development, and research on their materials, fabrication, design, mechanism, and control must still be conducted.[1–4]

In this Thesis, we consider soft sensors and actuators in one particular geometry: fibers. Functional fibers are thin and long 1-dimensional elements, in which functionality is distributed continuously rather than concentrated in discrete points, and large lengths and areas are readily addressed with a minimum number of contact ports to peripherals [5]. Additionally, the high aspect ratio enables unique applications, for instance when a device needs to be inserted within a narrow torturous channel [6]. Finally, fibers can be integrated into textiles, which are ideally suited for human body contact [7].

Within the scope of soft functional fibers for mechanical sensing and actuation, we address three principal challenges:

Materials and fabrication. Functionality is evoked by the arrangement of diverse materials with specific properties in defined structures. In this work, we rely on the preform-to-fiber thermal drawing technique for the realization of functional fibers, which is traditionally employed for the manufacture of telecommunication optical fibers [8]. Thanks to advancements in process technology, particularly in the last two decades, thermal drawing enables the co-processing of multiple materials into long fibers with fine textures and intricate architectures [6]. In

a noteworthy recent breakthrough, some thermoplastic elastomers, a material class that unites thermoplastic processing-attributes with elastomer mechanical properties, could be thermally drawn [9]. However, thermal drawing is also restrictive in the specific materials that can be processed and co-processed [10]. Additionally, the processing can induce dramatic changes in material properties [11]. Thus, the materials selection must be geared towards processing as well as application. In this work, the focus lies on the characterization of rheological, mechanical, and electrical properties. This task is particularly challenging because often properties are inter-dependent, such as the electrical conductivity that varies due to mechanical deformations, and are affected by treatment history as well as testing conditions. Considered materials in the soft functional fibers include various thermoplastic elastomers as dielectrics and conductors in the form of polymer composites as well as solid and liquid metals. The peculiar properties of these materials require an adapted fabrication strategy, including pre-processing steps, the quintessential thermal drawing itself, and post-processing.

Design and mechanism. Next to the constituting materials, the device design and working mechanism play an essential role. In a mechanical sensor, an electrical signal is triggered by a mechanical deformation, which yields information about the stimulation type, intensity, and location. Oppositely, in actuators, a precise deformation is generated through an applied signal [12]. With the right fiber design, which is constrained in materials and geometry by the thermal drawing fabrication process, a transduction mechanism is evoked in the soft fibers. Additional complexity is introduced by the paradigm shift away from standard arrays of discrete transducers and towards long continuous soft functional fibers [13]. For instance, in distributed mechanical sensors it is often difficult to characterize simultaneously the deformation mode, intensity, and location, and the task becomes more challenging still when multiple stimuli applied at once on one fiber-based sensor must be decoupled.

Implementation and application. Finally, the developed soft functional fibers must be embedded into suitable systems to result in functional products ready to take on real-world problems. This task involves the assembly of one or multiple fibers into a suitable pattern, such as in a textile. Additionally, the fibers must be interfaced through contact ports to peripheral systems, usually at the fiber ends, which is challenging because the connection of soft materials to standard hard components is prone to failure [14]. The selection of the peripheral hardware to address the fiber-based devices is critical as well. For instance, a sensor becomes only useful when it is integrated in a suitable electrical circuit that enables accurate readout by a control unit, such as a microcontroller. Additionally, the raw signal must be treated by algorithms and models to become valuable information, often involving adapted calibration schemes [12]. Finally, the value of developed soft fiber-based sensors and actuators must be demonstrated in applications where a real-world problem is solved, ideally highlighting the advantages over existing technologies.

The Thesis is organized as follows:

In Chapter 1, the thermal drawing process is introduced with a focus on previously developed fiber materials and structures. Additionally, the essential material class of thermoplastic elastomers is explored, by analyzing the chemical composition and microstructure as well as rheological and mechanical properties. Finally, the thermal drawing process flow is outlined with a focus on practical considerations of soft materials.

Building upon this materials and fabrication platform, several fiber-based devices are presented and the aforementioned challenges are addressed. In the first part, the focus lies on sensing and each chapter is aimed at one of the three conceptual elements of a sensor: the structural design, the constituting materials, and the signal processing. In the second part, actuation is coupled with sensing to develop soft robotic fibers. Each of these chapters can also be considered as a stand-alone work and thus contains a specific motivation and conclusion. Some of the works are also published elsewhere.

In Chapter 2, the research is aimed at the design element of a sensor. Fibers with an asymmetric elastomer architecture are developed. Thanks to advanced mechanical analysis, involving a hyperelastic material model and finite-element analysis, the fiber microstructure is tailored to respond in a predictable and reversible fashion to different pressure ranges and locations. This developed pressure-sensing concept enables the facile functionalization of large surfaces, demonstrated by a fiber-augmented gymnastic mat for the monitoring of human body position, posture, and motion.[15]

In Chapter 3, the focus lies on the materials. A polymer nanocomposite with carefully engineered rheological, mechanical, and electrical properties is introduced. The nanocomposite enables the development of a whole family of fiber devices, including a shape-sensing fiber based on piezoresistivity, a pressure-sensing fiber based on a variable path length of the electrical current, and a stretch-sensing fiber based on measures of capacitance.

In Chapter 4, signal processing, as the third pillar of sensing, is addressed by employing electrical reflectometry within microstructured elastomeric fibers that integrate liquid metal conductors. Reflected electrical waves, triggered by multimodal deformations of the fiber structure, are investigated experimentally and theoretically. This unprecedented physical mechanism enables multiplexed measurements of the mode, magnitude, and position of multiple simultaneous pressing and stretching events.[16]

Finally, in Chapter 5, both actuation and sensing schemes are combined, resulting in robotic fibers that can accurately accomplish extensive 3-dimensional motion driven by fiber-embedded tendons. Additional modular functionalities are evoked by embedded light guides, electrical wires, and fluidic channels.

1 Thermal drawing of soft materials: A platform for functional fibers

The field of functional fibers — fibers that incorporate a function besides mere mechanical integrity — is largely driven by innovations in fiber materials, structures, and processes. Indeed, it is the high purity of silica glass, created by vapor deposition and shaped by thermal drawing, that enabled the guiding of light in optical fibers at losses below 1 $dB.km^{-1}$ [17]. Similarly, the introduction of conductors and semiconductors in intimate contact gave rise to optoelectronic functionalities in thermally drawn fibers [5].

Soft materials can extend functionalities in thermally drawn fibers further, but they pose a significant processing challenge. In this chapter, a materials and process platform for soft multi-material fibers is introduced, which enables a novel generation of functional fibers. First, the previously established materials, structures, and functionalities are presented in a discussion of the state-of-the-art of thermally drawn fibers. Next, thermoplastic elastomers, which are the key to soft fibers via thermal drawing, are introduced in the form of their chemical composition and microstructure, as well as their process-relevant rheological attributes and their application-governing mechanical properties. Finally, the technical aspects of the fiber manufacturing process with a focus on soft materials are outlined.

1.1 Thermal drawing of multi-material fibers

Thermal drawing is a fabrication technique that consists of the conversion of a macroscopic preform into a fiber through the controlled viscous flow of material (Figure 1.1a). The resulting fiber exhibits a length that is orders of magnitudes larger than the preform, and a cross-section that is scaled down according to volume conservation. Quintessential to the process is that the fiber maintains the same cross-sectional structure with equal relative dimensions as the preform along its entire length [6].

The thermal drawing process features many advantageous properties. For one, the constitutive materials can be shaped and assembled on the macroscopic level, allowing the use of standard machining and assembly approaches, such as milling and stacking [22]. This enables the

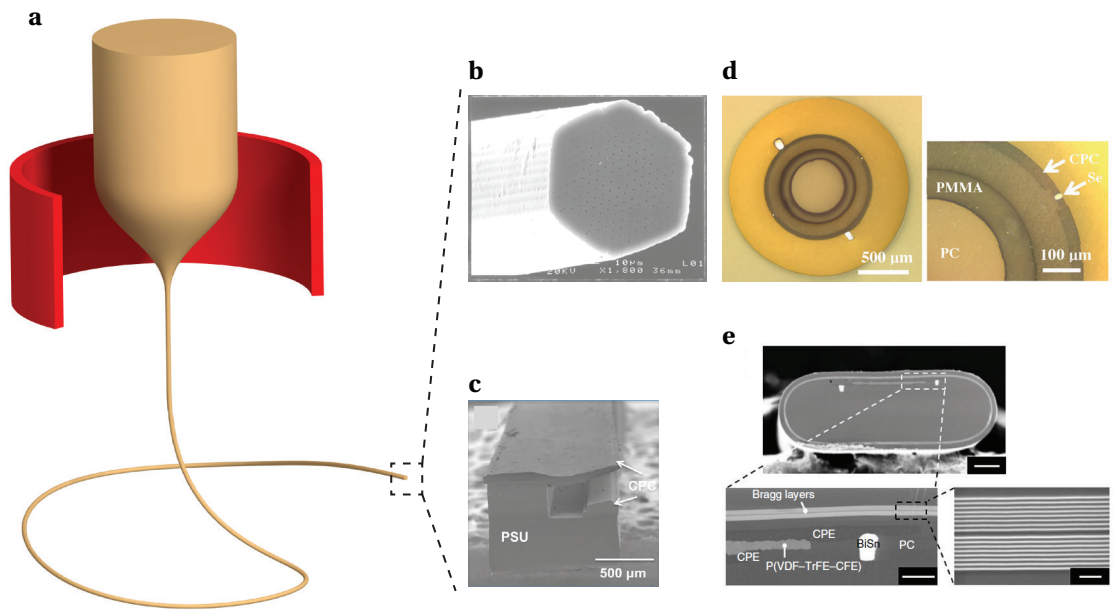

Figure 1.1 – Thermal drawing of functional fibers. a) Schematic of thermal drawing process. b) Silica photonic crystal fiber [18]. c) Thermoplastic electromechanical fiber with polymer composite electrodes for pressure sensing [19]. d) Thermoplastic optoelectronic fiber featuring an optical waveguide, a semiconductor, and electrodes of metal and polymer composite [20]. e) Thermoplastic electrosctrictive fiber with a P[VDF-TrFE-CFE] layer, electrodes of metal and polymer composite, and a Fabry-Perot optical cavity of alternating layers of PC and $As_{25}S_{75}$ [21]. Scale bars for top, bottom left, and bottom right are 100, 20, and 2 µm, respectively.

simple realization of fibers of various shapes with complex internal architectures on the µm or even nm scale, where different materials are localized in prescribed positions and are in intimate contact [8]. The drawing tower itself essentially only consists of a feeding mechanism for the preform, a furnace with accurate local temperature control, and a take-up spool for the fiber. During the drawing, the diameter of the fiber, which is continuously monitored, can be easily controlled by the feeding speed of the preform and the winding speed of the fiber [23]. Moreover, while being a batch process, thermal drawing is highly scalable. For instance, in the optical fiber industry, where thermal drawing is historically most applied, a single preform of length 1 m can be converted to 40 km of fiber [17].

However, the process also poses some challenges, mostly regarding the identification and engineering of materials that can be drawn and co-drawn, which, in concert with controlled microstructures, enables novel functionalities. Materials must be able to viscously deform in a specific temperature regime, and have sufficient mechanical resilience to support the drawing stress and maintain their cross-sectional architecture [10]. Additionally, materials must not crystallize or degrade during the process. Thus, in the case of glasses, the supercooled state must be maintained under the temperature and time conditions of the process [8]. Thermal drawing becomes especially difficult when multiple materials with different processing attributes are combined within a single preform and co-drawn.

While still limited, materials found to be compatible with the process now encompass candidates from several different material classes. In the following, examples of fiber materials and structures as well as resulting functionalities that have shaped the field are presented.

Thermal drawing became an industrially established process through the large-scale production of optical fiber. The constituting material is silica glass, because it exhibits extremely low losses of <1 $dB.km^{-1}$ at a high level of purity and is found to be highly compatible with the thermal drawing process, allowing the manufacture of homogeneous fibers with µm scale cross-sectional dimensions over tens of km length [17]. Beyond standard step-index optical fibers, where the necessary contrast in refractive index is achieved through doping of the core, for instance of GeO_2 [17], silica glass is also employed in microstructured optical fibers [24]. In these, the optical waveguiding is manipulated by the structure. For instance, in the case of photonic crystal fibers, a periodic array of air holes runs along the length of the fiber (Figure 1.1b), representing an excellent example for the achievable sophistication and feature sizes of fibers through thermal drawing [24]. The technique has also been extended to other glasses, such as chalcogenides [25], fluorides [26], and phosphates [27], mostly following the goal of broadening the wavelength range of low-loss guidance in optical fibers.

Next to glasses, thermoplastics represent an important materials class compatible with thermal drawing. Although attenuating light at levels that are several orders of magnitude above glass, thermoplastic fibers are attractive in terms of their mechanical performance. Thermoplastics have a lower Young's modulus than glasses, generally on the order of magnitude of 1 GPa, allowing higher fiber flexibility even at larger diameters. Additionally, they exhibit superior fracture toughness and fractures are of a ductile rather than brittle nature, reducing the risk of sharp edges and shards upon failure [28]. Thermoplastics bring also a processing advantage as they can be formed at significantly lower temperatures and using a variety of different techniques. This is useful during the drawing but also during the preceding preform fabrication steps [24], allowing melt-based techniques (e.g. molding, 3D-printing, extrusion), solvent-based techniques (e.g. casting, spin-coating, dip-coating), machining (e.g. milling, drilling), and polymerization in molds. Prominent examples of drawable thermoplastics are poly[methyl methacrylate] (PMMA), polycarbonate (PC), polysulfone (PSU), and polyethylenimine (PEI) [6]. Recently, biodegradable thermoplastics were also identified to be compatible with thermal drawing, enabling, for instance, edible fibers of gelatin [29] and drug-delivery fibers of poly[D,L-lactic-co-glycolic acid] (PLGA) [30].

The attractive mechanical properties in conjunction with the ease of prototyping and handling of thermoplastic fibers has been a major driving force in the emergence of multi-material fibers [6]. In these, the thermoplastic acts as substrate for processing onto which active materials are piggybacked. As substrate and active material are co-processed, the active material must also be compatible with thermal drawing. However, the necessary compatibility only extends to the ability to follow the deformation induced by the process. It is thus important to distinguish between the substrate material, which must exhibit the rheological character that makes it truly 'drawable', and the active material, which must merely endure the pro-

cess. Nonetheless, the discovery of suitable pairs of substrate and active material remains challenging.

Table 1.1 – Classes and examples of materials compatible with the thermal drawing process, subdivided by draw-supporting substrate and active constituent.

Substrate materials	
Glasses	Silica glasses [17] Chalcogenide glasses[25] Fluoride glasses [26] Phosphate glasses [27]
Thermoplastics	PMMA [20] PC [20] PSU [20] PEI [5] gelatin [29] PLGA [30]
Active materials	
Metals	Sn [5] Sn–Zn [20] Bi–Sn [21] Pt–Cu –Ni –P [31]
Polymer composites	cPC [19] cPE [22] carbon nanofibers in cPE [32]
Piezoelectric and electrostrictive	P[VDF-TrFE] [33] P[VDF-TrFE-CFE] [21]
Semiconductors	Se [20] As_2Se_3 [34] $As_{40}Se_{50}Te_{10}Sn_5$ [5] $Ge_{17}As_{23}Se_{14}Te_{46}$ [35] SnSe [36] $Ge_{22}As_{18}Se_{15}Te_{45}$ [37]

The integration of active materials in targeted architectures has resulted in a variety of different functionalities, which extend from the optical to the electrical field. In such applications, the integration of conductors in thermally drawn fibers is essential. Conductive pathways have been realized in fibers through crystalline and amorphous metals as well as polymer nanocomposites [6]. Metals exhibit conductivities that are several orders of magnitude higher than composites, but their processing by thermal drawing is limited, because crystalline metals must be in a molten state when processed, requiring a fiber substrate material with a higher processing temperature than the melting temperature of the metal. For instance, Au, Ag and

Fe have been drawn in silica glass [38]. Thermoplastic substrates allow only the co-processing of lower melting point metals, such as Sn in PEI [5]. Moreover, crystalline metals must be fully enclosed by viscous materials during processing to retain structural integrity, and the minimum size of metals is limited by capillary breakup [6]. In this regard, amorphous metals are attractive candidates because they are processed in a supercooled viscous rather than liquid form, enabling free-standing structures and smaller feature sizes [31]. Finally, polymer nanocomposites, which consist of a polymer matrix enclosing a percolated network of conductive fillers such as carbon black in polycarbonate (cPC) and carbon black in polyethylene (cPE), can also be integrated in thermally drawn fibers. They exhibit thermoplastic processing attributes, including viscous deformation at elevated temperature, enabling the realization of freestanding structures and interfaces with liquids in fibers. However, their conductivities are significantly lower than metals and are strongly affected by the deformations during the drawing process [11, 39]. Exemplary applications of conductors in fibers include electrodes as neural probes in bioengineering[40], as conductive films in fiber capacitors for touch sensing [41], and as resistors that can heat and expand under voltage pulses and act as an polarization switch in optical fibers [42]. A final example that is particularly relevant to this work is the use of composites to impose a potential drop in fibers. This effect can be exploited to localize stimuli in fibers because the length of the current pathway through the resistive medium relates directly to the measured resistance. This technique was implemented in fiber consisting of two conductive polymer composite films (carbon black-loaded PC) being arranged in a cantilever-like structure made of a flexible polymer (PSU) that are contacted under mechanical load (Figure 1.1c), thus enabling pressure sensing [19].

Materials with peculiar dielectric properties have also been exploited in thermally drawn fibers. By integrating the piezoelectric poly[vinylidenefluoride-trifluoroethylene] (P[VDF-TrFE]) an acoustic emitter and sensor was created in fibers [33], whereas the electrosctrictive material poly[vinylidenefluoride-trifluoroethylene-chlorofluoroethylene] (P[VDF-TrFE-CFE]) resulted in electromechanical actuation (Figure 1.1e) [21].

Finally, semiconducting functionalities were achieved through integrated chalcogenide domains for uses as transistors [43], phase-change memory [37], heat sensing[35], thermoeletrics [36], optoelectronics (Figure 1.1d)[5], and photonic bandgap devices [34]. These fibers are excellent examples of truly multi-material microstructures that can be achieved by thermal drawing.

1.2 Thermoplastic elastomers

While the range of substrate materials for thermal drawing discussed above is extensive, it has so far been limited to glasses and thermoplastics with elastic moduli on the order of 1000 GPa and 1 GPa, respectively [44]. When considering technologically relevant materials that exhibit lower stiffnesses, one comes inevitably across the class of elastomers, which feature moduli ranging from 100 kPa to 100 MPa. However, elastomers are chemically crosslinked polymer

chain networks, meaning, unlike thermoplastics, they cannot be processed under simultaneous application of heat and stress, thus excluding thermal drawing. Fortunately, a particular type of polymeric material combines the best of both worlds: thermoplastic elastomers exhibit elastomeric mechanical properties at ambient temperatures and thermoplastic processing behavior at elevated temperatures [44]. Indeed, thermoplastic elastomers lay the foundation for soft fibers fabricated via thermal drawing [9].

1.2.1 Chemical composition and microstructure

The softness and high deformability of standard elastomers stems from their relatively long polymeric chains having a high degree of flexibility and mobility that are joined in a network structure. The network is connected by crosslinks, which give elastomers their solid-like features by preventing the chains from freely flowing under external stresses [45]. They are chemical in nature and do not weaken under heat, thus the material cannot be thermoformed. Only under excessive heating do the crosslinks break, resulting in polymer degradation [44].

The particular properties of thermoplastic elastomers originate from their chemical composition and resulting microstructure. Most thermoplastic elastomers are block copolymers consisting of hard thermoplastic polymer blocks linked to soft elastomeric segments. The hard segments are located at the chain ends and thus enclose the soft elastomeric segments. The hard chain-end segments from several adjacent chains aggregate together to form rigid, often crystalline, domains within a soft matrix, resulting in a phase-separated microstructure (Figure 1.2 a). As these domains are nm-sized, they are too small to be observed in visible light and thermoplastic elastomers are usually transparent materials. However, the phase-separated structure can be imaged using staining techniques and transmission electron microscopy (Figure 1.2 b). Much like the chemical crosslinks in standard elastomers, the hard domains act as anchor points to restrict the soft-chain segment motions. However, for thermoplastic elastomers, these crosslinks are physical in nature, which weaken and disappear upon heating or exposure to a solvent. Most importantly, they are reversible and will reform when cooled or when the solvent evaporates [45]. Thus, thermoplastic elastomers can be processed by conventional thermoplastic processing techniques, such as compression molding and thermal drawing.

A very common subgroup of thermoplastic elastomers are styrenic block copolymers. Their chains consist of the simple structure A-B-A, where A is the thermoplastic polystyrene and B is the elastomer segment. Typically, the elastomer is an polydiene, such as polybutadiene or polyisoprene. The widely used nomenclature for these materials is SBS and SIS, respectively, where S stands for styrene, B for butadiene, and I for isoprene. Their molecular structure are shown in Figure 1.2c. Both polybutadiene and polyisoprene units exhibit a double bond, which is prone to chemical attack, limiting the resistance to oxidation and thermal degradation. A common chemical alteration made to SBS is the use of poly(ethylene-butylene) as a middle segment, which doesn't include double bonds, resulting in the more stable SEBS [45]. A

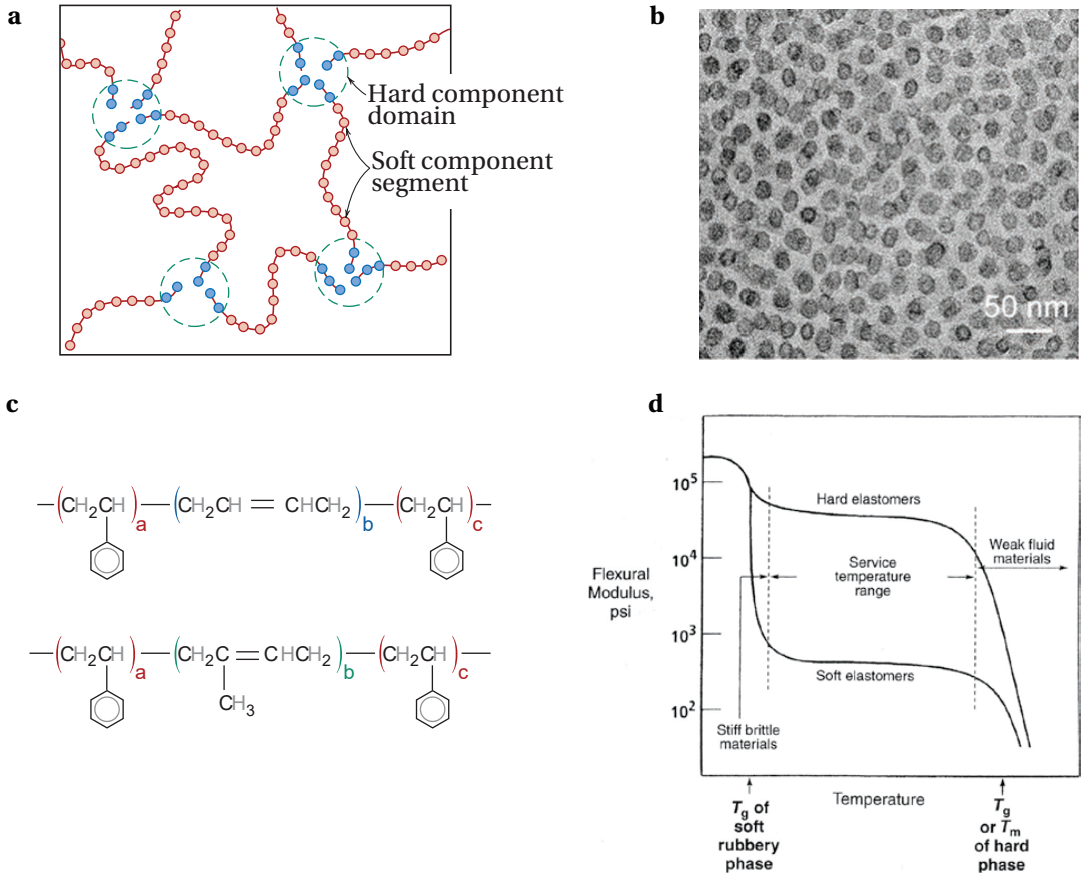

Figure 1.2 – Chemical composition and microstructure of thermoplastic elastomers. a) Schematic illustrating the molecular structure and arrangement of block copolymer chains that make up thermoplastic elastomers. Reproduced from reference [44]. b) Transmission electron microscopy image of a stained sample of SEBS, showing the phase-separated microstructure. Reproduced from reference [9]. c) Chemical composition of the common thermoplastic elastomers SBS and SIS. Reproduced from reference [44]. d) Evolution of stiffness of thermoplastic elastomers with temperature, indicating the different temperature windows. Reproduced from reference [45].

less employed and more recently developed thermoplastic elastomer group, is the Wacker Geniomer family (recently renamed to Genioplast). In these, the hard segment is aliphatic isocyanite and the soft segment is polydimethylsiloxane. They exist in different formulations, where different properties are brought about by changes in hard-to-soft ratios or total chain length [46]. In fact, all the aforementioned thermoplastic elastomers are employed in this Thesis:

- SEBS G-1657 (Kraton)
- SIS D-1113 (Kraton)
- Geniomer 145 (Wacker)

- Geniomer 345 (Wacker).

In the thermoplastic elastomer composite systems, both types of polymers retain most of their individual characteristics. For instance, both the hard and soft phase exhibit a specific softening temperature (glass transition or crystalline melting temperature). These two transition temperatures delimit the use ranges of the material as a whole (Figure 1.2 d). At very low temperature below the glass transition temperature of the elastomer phase (typically < -50 °C), the material is stiff and brittle. Thermoplastic elastomers are usually not employed within this range. At ambient temperature between the transition temperature of the elastomer and of the thermoplastic, the material is soft and elastic, resembling a conventional elastomer. This range is the typically service range for applications. Finally, above the transition temperature of the thermoplastic phase, the material becomes a viscous fluid, defining the processing window.

In the following, both relevant temperature ranges shall be investigated in detail for the thermoplastic elastomers employed in this Thesis. First, the processing window is discussed by investigating the rheological properties, followed by the application window where the mechanical properties are analyzed.

1.2.2 Rheological properties

While physically crosslinked copolymers appear to be the natural candidate for soft thermally drawn fibers, by far not all thermoplastic elastomers are compatible with the process. This stems from the fact that thermal drawing raises stringent requirements regarding the flow of material during the process, i.e. the rheology. Studies have found that the substrate material must exhibit relatively high viscosities at the processing temperature, typically between 10^4 and 10^7 Pa.s, where the material can sustain the large stresses during drawing [8]. A large viscosity is also essential for slowing thermal reflow and maintaining the structural integrity of the fiber [22].

Beyond the analysis of simple viscosity, detailed insights on the rheological behavior of materials can be obtained using oscillatory shear rheology, where measures of viscosity and modulus can be separated into an elastic (storage) and viscous (loss) component. Although it does not replicate the complex flow of material during thermal drawing, particularly because flow is extensional rather than in shear, it does serve as a suitable tool to screen and compare different materials. Using this tool it was found that thermoplastics suitable for thermal drawing exhibit a rapid decrease in storage modulus with temperature, whereas the loss modulus remains at elevated levels even beyond the glass transition temperature and only slowly decreases with increasing temperature. The ideal temperature window for thermal drawing is thought to be slightly above the glass transition temperature of the hard phase in thermoplastic elastomers, where the loss modulus remains at a high level and dominates over the storage modulus [9]. With this criterion in mind, one should favor thermoplastic elastomers for which the two-phase microstructure persists at temperatures above the glass transition. In such as state,

flow can only occur if the hard segments at the polymer chain ends are pulled out of their domains, which requires an extra amount of energy. Such behavior is favored by systems with a large segmental incompatibility, such as is the case for SBS, SIS, and in particular SEBS, as well as by large molecular weights [45]. Indeed, it was found that polystyrene domains in SEBS aligned in the direction of the drawing, indicating that the structure didn't disaggregate during processing [9]. Unfortunately, few polymer manufacturers supply such detailed insights into the rheological properties of their products. Therefore, material discovery usually consists of screening the viscosity or melt flow index data provided by the supplier, followed by in-house oscillatory shear rheology measurements and thermal drawing trials.

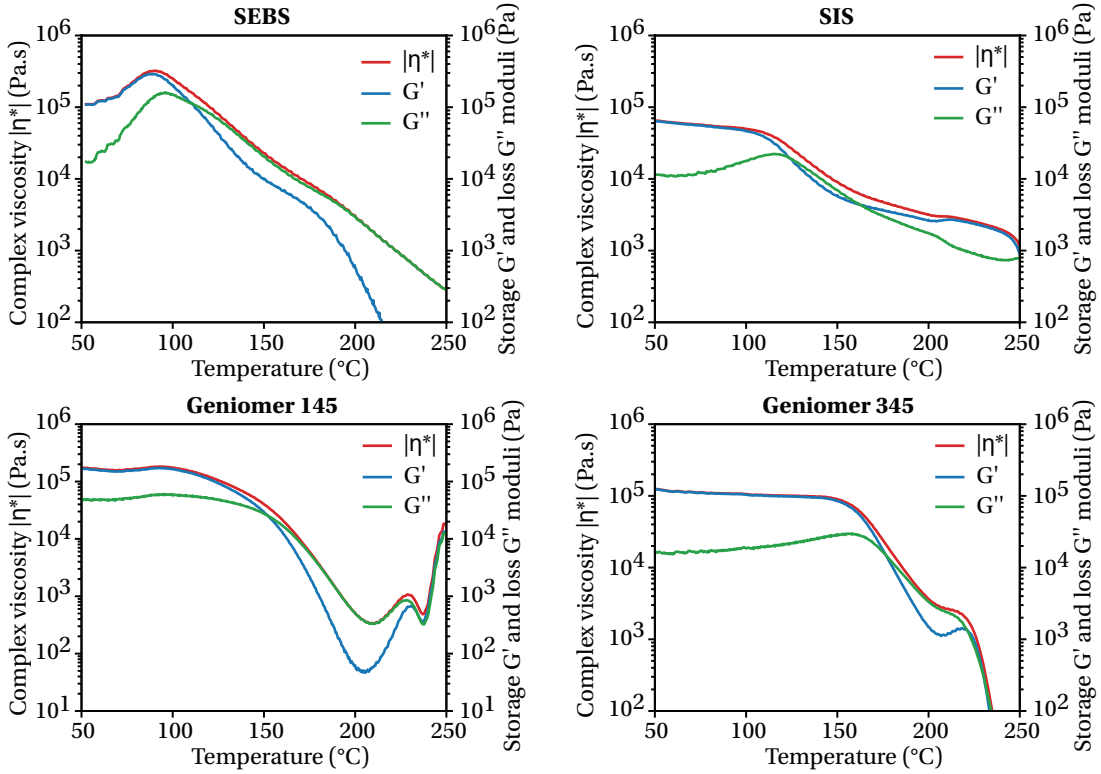

Figure 1.3 – Oscillatory shear rheology analysis of the thermoplastic elastomers under increasing temperature.

Indeed, all the thermoplastic elastomers employed and discovered within this Thesis exhibit the rheological features named above —some more pronounced that others. The results of temperature ramps under oscillatory shear deformation are shown in Figure 1.3. The characterization was carried out using a TA Instruments AR 2000 Rheometer under an oscillation strain of 1 % and an angular frequency of 1 rad.s $^{-1}$. As expected, all materials demonstrate a dominantly elastic behavior at lower temperatures, where the storage modulus is significantly higher than the loss modulus. With increasing temperature, the moduli approach one another up to the cross-over point. This cross-over indicates a transition from mostly elastic to viscous behavior and correlates to the glass transition temperature of the thermoplastic phase. It is very similar for the two polystyrene-based materials SEBS and SIS, at approximately 110 °C

and 124 °C, respectively. For the Geniomer materials, the cross-over is found at higher temperatures of 152 °C for Geniomer 145 and 176 °C for Geniomer 345. Beyond the cross-over temperature, the viscosity steadily decreases for all materials, but is dominated by a viscous response (the loss modulus is larger than the elastic modulus). Slightly above the cross-over temperature is thought to be the ideal processing temperature window for thermal drawing. At a temperature setting that is too low, the material behaves to a high extent elastically, resulting in plastic fiber breakage under excessive tension. At a temperature setting that is too high, the material behaves viscously, but the overall viscosity is so low that the material flows too freely, resulting in overly thin fibers and a high risk of viscous breakage. Note that for SIS the elastic modulus is indeed lower than the loss modulus but it remains at comparable levels. Thus, the materials still exhibits a viscoelastic character in the processing window. Indeed it was found that SIS is more challenging to process by thermal drawing than the other materials.

All materials but SEBS exhibit a second cross-over point at higher temperatures, where the thermomechanical response is once again dominated by the storage modulus. This second transition is thought to be caused by the thermal degradation of the polymers. SEBS is an exception because the poly(ethylene-butylene) middle segment results in a particularly high resistance to degradation. SIS, however, exhibits a high sensitivity to degradation, as the second cross-over temperature appears at relatively low temperatures of approximately 162 °C. Thermal degradation influences the processing compatibility of the different thermoplastic elastomers with one another as well as with standard thermoplastics. For instance, SIS cannot be drawn with either of the Geniomers, because it degrades at the high temperatures of > 150 °C that are required for viscous flow of Geniomer. SEBS does not degrade at these temperatures and can indeed be co-processed with the Geniomer materials.

Based on this rheological analysis and practical drawing experiments, we conclude that all named thermoplastic elastomers can be individually processed by thermal drawing, resulting in thin fibers with the possibility of high structural complexity. Furthermore, SEBS –SIS and Geniomer 145 –Geniomer 345 make excellent materials pairs, resulting in multi-material elastomeric fibers through termal drawing. While more challenging because of low viscosity at high temperature, SEBS can also be paired with Geniomer 145 or Geniomer 345.

1.2.3 Mechanical properties

In addition to the rheological properties of the thermoplastic elastomers in the processing temperature window, the mechanical properties at ambient temperatures are most relevant to this Thesis. Quantitative knowledge about the stresses at which the materials deform is essential for their application in soft and deformable fiber-based devices. However, describing the mechanical properties of elastomers and thermoplastic elastomers is challenging, because they exhibit a pronounced viscoelastic behavior. Thus the mechanical response of thermoplastic elastomers is heavily dependent on temperature and strain rate. Additionally, processing conditions influence the microstructure, which determines mechanical behavior. For instance,

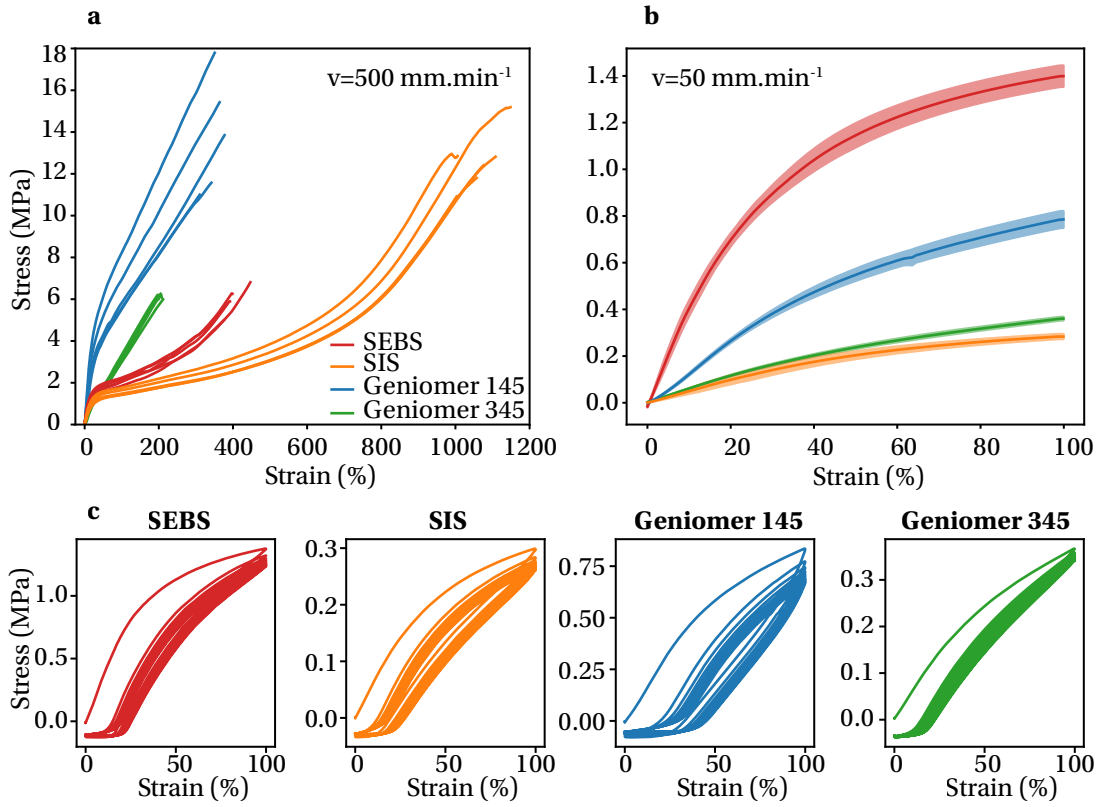

Figure 1.4 – Uniaxial tension testing analysis of the thermoplastic elastomers. a) Stress –strain curves of multiple fiber samples for each thermoplastic elastomer at an extension rate of 500 mm.min^{-1}. b) Stress –strain curves at an extension rate of 50 mm.min^{-1} up to a strain of 100%. The solid lines represent the mean and the shaded area the standard deviation for multiple samples. c) Dynamic tensile tests of the materials, where the strain is varied between 0% and 100% for 10 cycles.

thermal drawing is known to cause alignment of polymer chains, particularly at higher drawing stresses, resulting in altered stress –strain curves [30]. Moreover, the stress–strain curves of thermoplastic elastomers are non-linear [44]. Finally, the mode of deformation plays an important role and often different types of mechanical tests must be carried out to adequately describe the response of a thermoplastic elastomer [47].

However, the purpose of this section is to generally present the employed thermoplastic elastomers and highlight their differences as well as the most relevant parameters. Thus, the mechanical properties are only characterized by uniaxial tension of fiber samples with a clamped length of 30 mm and approximate diameter of 2 mm. The results of the mechanical analysis are shown in Figure 1.4. In a first test, we aim at quantifying the elongation at break, by stretching the materials at high extension speeds of 500 mm.min^{-1} up to failure (Figure 1.4a). All thermoplastic elastomers employed in this Thesis exhibit high elongations at break, outperforming the standard elastomer for soft and stretchable devices poly(dimethylsiloxane) (PDMS, Sylgard-184) with an elongation at break of 100% [48]. The lowest value of 202% was

found for Geniomer 345. SIS proved to be the most stretchable material with an elongation at break as high as 1065%. SEBS was found to fail at 402%. As applications rarely require elongations in excess of 100%, even in the fields of soft and stretchable electronics and wearable devices, we deem all materials satisfactory in this regard. Next, we quantify the elastic modulus of the materials by stretching them up to 100%, which represents the most relevant strain range in applications, at lower extension rates of 50 $mm.min^{-1}$ (Figure 1.4b). As elastomers exhibit non-linear stress–strain curves, the modulus is expressed by the stress value at 100% strain. We find that SIS and Geniomer 345 are particularly soft, with 100%-moduli of 280 kPa and 360 kPa, respectively. SEBS is the stiffest material with a 100%-modulus of 1.4 MPa. Finally, we characterize the elasticity (also called stretchability) of the materials, which relates to the reversibility of deformation, through dynamic tensile testing, where the fiber samples are repeatedly stretched between 0% and 100% for 10 cycles (Figure 1.4c). All the thermoplastic elastomers exhibit a pronounced hysteresis, where the unloading curve deviates from the loading curve. Additionally, upon load removal, the material does not retract entirely. This remnant deformation, also termed tensile set, is quantified by the strain at which the unloading curve crosses the 0-stress horizontal line. The negative stresses beyond this point are the result of the elongated fiber bending between the clamps, thus exerting an opposing force. The remnant deformation is the result of viscous and plastic contributions to the dominantly elastic deformation. Finally, a stress softening behavior is observed by a shifting of the hysteresis loop to lower stress values. This stress softening is commonly observed for elastomers and thermoplastic elastomers, particularly during the first few cycles. The origin of this effect, often called Mullin's effect, is still debated [49]. In terms of tensile set, SIS is the most elastic material with a tensile set of 12% after one 100%-deformation cycle. However, the stress softening during cycling is least pronounced for Geniomer 345, which also exhibits a low tensile set of 15%. SEBS is also deemed a highly elastic material with a tensile set of 14%. Geniomer 145 performed the poorest during the dynamic tensile tests with a tensile set of 19% and a pronounced stress softening effect.

1.3 Methodology for the thermal drawing of soft fibers

With the state of the art of multi-material thermal drawing and the fundamental aspects of thermoplastic elastomers established, the practical aspects of thermal drawing for the realization of soft functional fibers are discussed next. While all features of the process flow will be described, the focus lies on particularities of the fabrication specific to soft materials as well as extensions to the technique that were introduced in the context of this Thesis. The entire fabrication process can be roughly divided into three steps: preform preparation, thermal drawing, and fiber post-processing (Figure 1.5).

Preform preparation. The preform is the physical object that is converted into a fiber during the thermal drawing step through the controlled flow of material. The realization of a preform of high quality is of quintessential importance, as, in the best case, inaccuracies or defects in the preform are mirrored in the fiber cross-section or, in the worst case, the faults result in

severe inhomogeneities of the fiber along its length, such as diameter fluctuations, or even fiber breakage during thermal drawing. The preform is of macroscopic size, with a width and thickness on the order of 1 cm and a length on the order of 10 cm. However, some feature sizes can be on the order of 1 mm and smaller. The preform must have a consistent cross-section along the length, both in terms of dimensions and materials, but can otherwise take any desired geometrical shape, most often rectangular or round. Typically, single-material components of the preform are formed individually first, before being assembled and merged in a so-called consolidation step. For hard thermoplastics, the materials are usually obtained in standard geometrical shapes, such as plates or cylinders. The components are then machined into their desired forms through standard machining techniques, such as cutting, drilling, or milling. The thermoplastic elastomers, however, which make up the bulk of the fibers in this Thesis and represent the fiber substrate, are usually obtained in granular form. Moreover, due to their softness, machining of thermoplastic elastomers result in poor results. For these reasons, they are typically formed through compression molding. This technique involves the shaping of parts by exposing polymer granules to heat and pressure for a given time (typically, slightly above the glass transition temperature of the material in question, at approximately 0.1 MPa, for 10 min up to 12 hours) within highly defined confines brought forth by molds and cores (cores are molding elements that shape the interior of parts), which can sustain the high temperatures and pressures.

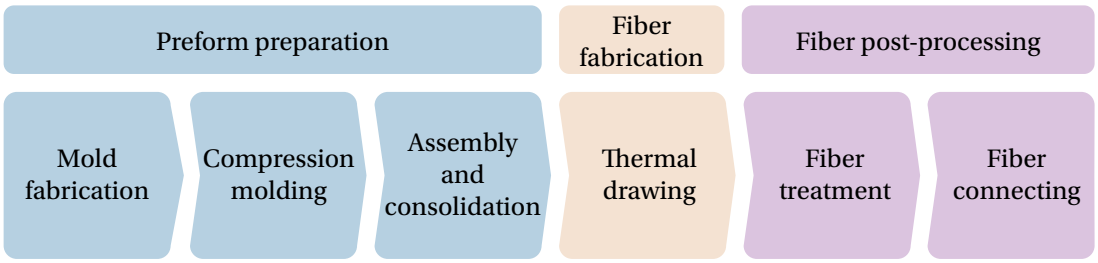

Figure 1.5 – Process flow chart of the functional fiber manufacturing.

Three categories of molds are employed within this Thesis: metal molds that are purchased in their desired geometry or shaped by machining, polytetrafluoroethylene molds (PTFE, Teflon) that is shaped in the same fashion, and, finally, polycarbonate (PC) molds that are formed by 3D printing. This last type of mold creation is particularly attractive because it allows molds of high complexity to be fabricated with little effort and at high speeds, facilitating the fiber prototyping and optimization. Furthermore, metal rods can be integrated within the PC mold as reinforcements or cores (Figure 1.7a). However, as the glass transition temperature of PC is 150 °C [44], which is below the softening temperature of Geniomer polymers, only SEBS and SIS can be formed by PC molds. Regardless of the type of mold employed, the removal of the part after compression molding is facilitated significantly by the use of Teflon tape and mold-release agent on the mold surface. If the preform shall contain solid materials other than thermoplastic elastomers, they can be shaped in a similar fashion. Once all the geometrically defined parts of the preform are produced, they can be assembled. Different

strategies of the assembly step were developed and they can be divided into three general cases, depending on the outer shape, inner architecture, and constituting materials of the preform. For rectangular preforms, the components constituted of different materials, such as thermoplastic elastomers or polymer composites, are typically stacked in a defined order (Figure 1.6a). Empty channels with defined geometries within the preform are realized by inserting mold cores within the stack. These can take the form of machined blocks or rods out of metal or PTFE. For cylindrical preforms, films composed of different materials can be rolled together (Figure 1.6b). Finally, cylindrical preforms featuring several interior cylindrical elements are fabricated directly in a suitable mold directly from thermoplastic elastomer granules (Figure 1.6c). The metallic mold has a cylindrical outer shape and includes several metallic rods fixed to the base plate to create cylindrical channels. In this case, the force during hot-pressing is applied longitudinally rather than transversely respective to the preform. Subsequently, the channels can be filled with another material by inserting it in the form of a rod. In a final preform fabrication step applicable to all assembly methods, the assembly is consolidated in a final compression molding step at temperatures and pressures lower than preceding treatments (at approximately 120 °C and 0.05 MPa) to maintain the structural integrity of the preform.

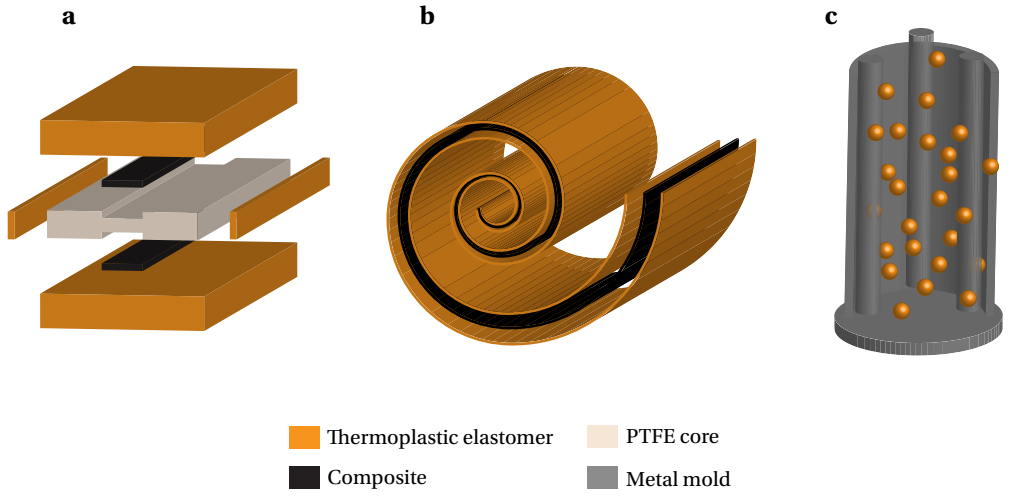

Figure 1.6 – Assembly of different types of preforms. a) Rectangular preform assembled by stacking of individual material components. b) Cylindrical preform assembled by rolling of several sheets. c) Cylindrical preform realized directly from granules inserted in a metallic mold with several cores to produce channels.

Thermal drawing. In the thermal drawing step, the preform is converted into a fiber through the controlled flow of material. From preform to fiber, the diameter is significantly reduced (by a drawdown ratio of 10 to 30 in this work) and the length increased by a corresponding factor determined by volume conservation (100 to 900 are typically reached in this Thesis). Thus, a typical preform with length 15 cm and diameter 3 cm yields a fiber of 30 m length with a diameter of 2 mm. Note that the the relative cross-sectional geometry and materials in the

preform remain the same in the fiber. For SEBS and SIS-based fibers the drawing temperature is set to approximately 200 °C (the ideal temperature depends on preform geometry and size due to changes in heat transfer) and for Geniomer constructs to 250 °C. With the bulk of the fiber consisting of one or several of the thermoplastic elastomers, active materials can be integrated into the soft fiber through three different techniques. (1) The active material is embedded at the preform stage and is co-drawn. Evidently, the active material must thus be capable of viscously deforming at the process temperature. This is the case for composite systems such as carbon black-reinforced polyethylene. (2) For liquid functional materials, such as the liquid metal Galinstan, the metal can be embedded within empty channels of the preform. Alternatively, it can be continuously injected into the preform while the fiber is being draw. Note that for sufficiently large channel diameters, the liquid metal can also be injected directly into the fiber after the drawing. (3) Finally, functional elements can also be introduced through feeding. This techniques involves the introduction of wire-like elements, such as metallic wires or thin optical fibers, into prescribed channels in the preform. During drawing, the channels narrow and latch on to the wire and pull it along, unspooling it continuously as the fiber is drawn. The wire element does not flow or deform during the process. Its diameter must therefore correspond to the size of the channel in the fiber (typically 50 to 500 μm). The fed element must also sustain the processing temperatures. The feeding setup, which sits on top of the drawing furnace, is shown in Figure 1.7b.

Fiber post-processing. Downstream of the thermal drawing step, additional treatments can be applied to the fiber to alter its configuration or embed it into a suitable system through adapted contacts. An advantage of thermoplastic elastomer fibers is that their shape can be reversibly altered through heat and pressure treatments. A common treatment is the reshaping of fibers under heat (typically a heat gun) to obtain a perfectly straight or twisted fiber (Figure 1.7c). The axial homogeneity of the thermally drawn fiber can also be perturbed, by locally compressing the fiber under heat. For instance, continuous channels within the fibers can be separated along the length by compressing a section of the fiber, thus isolating the two segments of the channel from one another. Tests were also carried out in which air channels were pressurized from within, thus extending outward. Also in this case, the length-symmetry can be broken by placing the fiber in a suitable mold (in a technique resembling blow-molding). The result of this fiber blow-molding process is shown in Figure 1.7d. Fiber complexity can also be extended by introducing additional elements. For instance, nylon lines or stiff wires can be inserted into channels in the fiber. Another post-processing technique is the combining of several fiber elements into assemblies. For instance, a braiding setup was realized, with which soft fibers could be over-braided with stiff thinner lines (Figure 1.7e, f). The most employed post-processing step, however, is fiber connection, which is essential for functional fibers. The element of interest must often first be made accessible at the fiber end. This is typically achieved using mechanical techniques such as cutting or grinding, but can also involve chemical treatments such as the application of a solvent. The connection depends on the employed materials and function of the fiber element. For instance, electrical connection is achieved by application of conductive silver paint for composite electrodes, insertion of thin

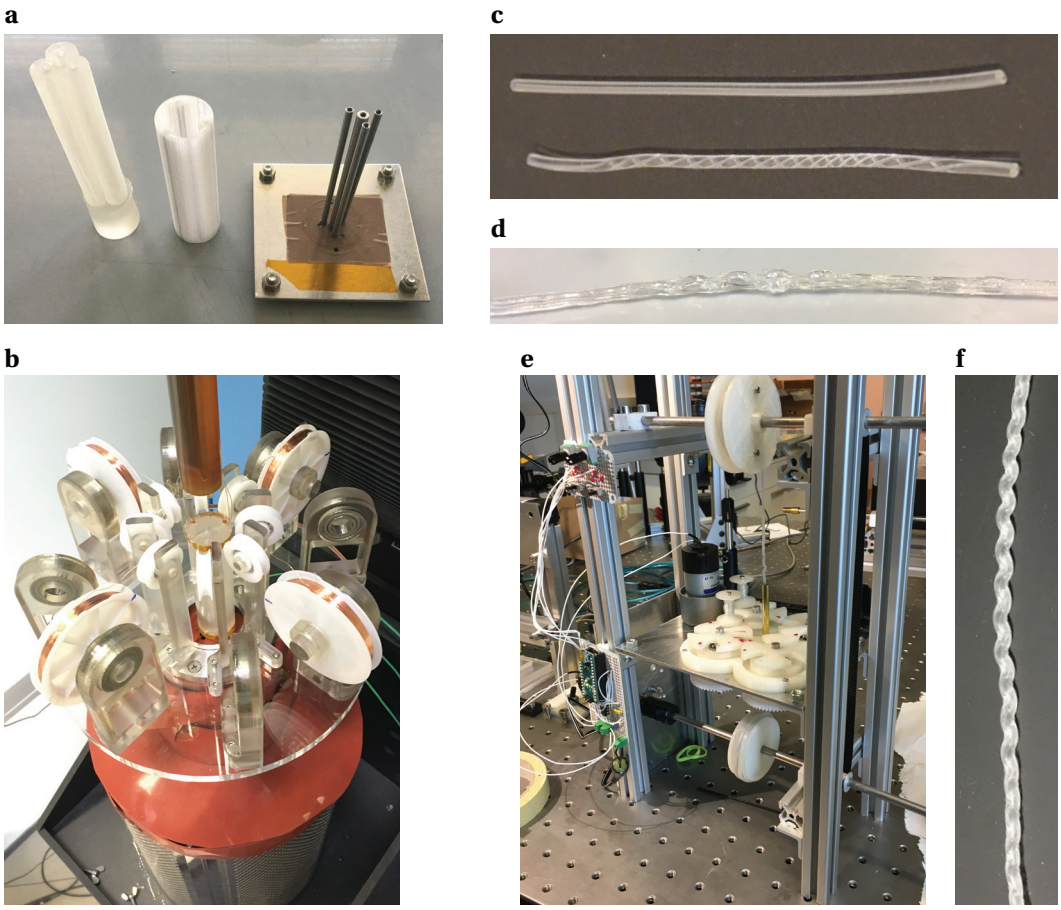

Figure 1.7 – Special extensions to the fiber manufacturing process. a) The preform fabrication can be facilitated through 3D-printed PC molds, which can be used in concert with metal rods. b) The addition of a feeding setup placed on top of the drawing furnace can be employed to integrate thin 1D elements into fibers during the thermal drawing process. c) Comparison of an untreated fiber and a post-processed fiber. The original fiber, as obtained through thermal drawing, contains several straight channels. Twisting the fiber while exposing it to heat allows a new fiber configuration to be programmed, as illustrated by the spirals formed by the formerly straight channels. d) Pressure can also be applied from within the channels, resulting in an expansion. This expansion can be controlled by an exterior fiber mold to break the axial symmetry. e) Fiber braiding setup as a fiber post-processing technique. f) Soft fiber over-braided with a thin stiff line.

metallic wires into liquid metal channels, or soldering in the case of fiber-embedded wires. For extensible air chambers in pneumatically actuated fibers, syringe tips are inserted and the interface sealed with epoxy.

The essence of the materials and fabrication platform established in this Thesis are summarized in Figure 1.8. It encompasses the different techniques that can be employed to integrate active materials in the fiber, specifically embedding and co-drawing, injecting, and feeding, as well as the range of materials and functional elements that can be integrated. In this Thesis the bulk of the fibers, the substrate, is always composed of a thermoplastic elastomer. Based

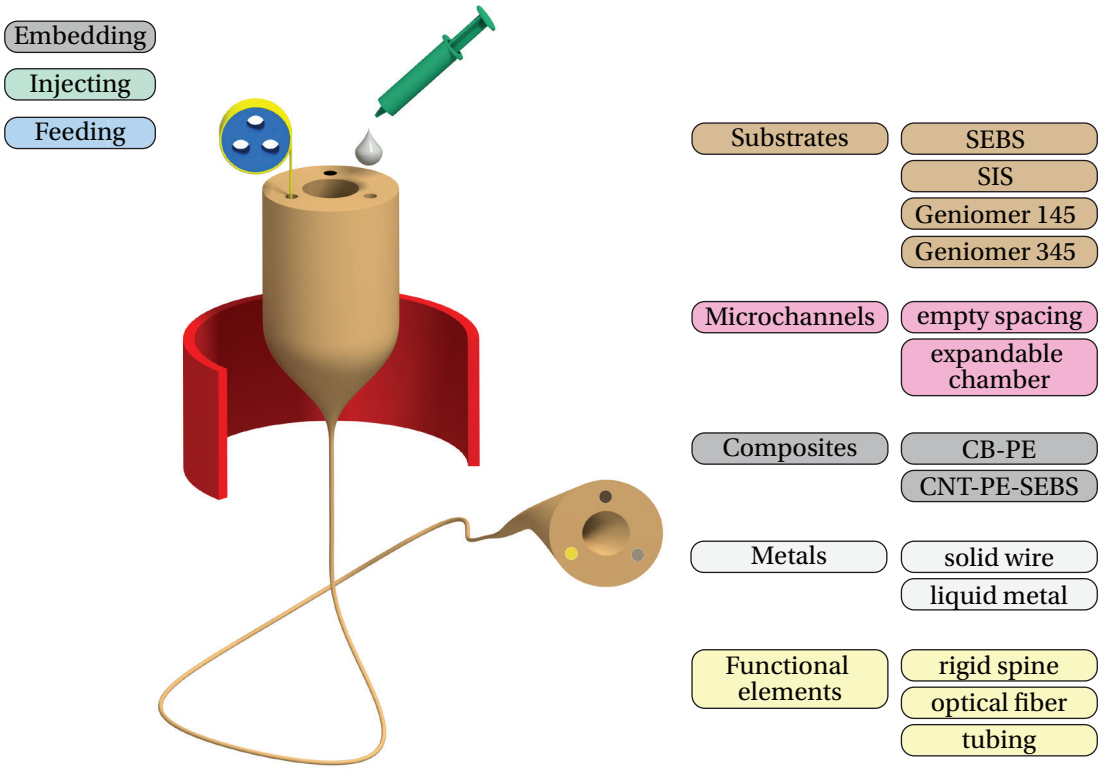

Figure 1.8 – Schematic outlining the materials and fabrication platform of soft functional fibers. On the top left, the principle techniques for integrating active materials in the substrate material are listed. They are illustrated in the schematic of the process. On the right-hand side, the different materials constituting the soft functional fibers in this Thesis are outlined.

on the rheological profile outlined in Section 1.2.2, the substrate material controls the draw by supporting the majority of stress during the process. It can be one of the four thermoplastic elastomers found to be compatible with thermal drawing: SEBS, SIS, Geniomer 145 and Geniomer 345. In the case of multiple of these substrate materials, the one with the highest viscosity at the processing temperature is thought to control the draw. Due to rheological as well as chemical similarities, SEBS and SIS are an ideal match. SEBS can also be co-drawn with any of the Geniomer materials, but poor interfacial bonding can be problematic during subsequent application. Additionally, the high processing temperature of Geniomer fibers results in significant reflow of SEBS features if not fully embedded in Geniomer. SIS cannot be co-drawn with Geniomer systems because it degrades at such elevated temperatures. Empty channel features are easily introduced into any of the substrate materials at the preform level, typically with diameters of 1.5 to 8 mm, and maintained throughout the thermal drawing step. However, excessively large or small channels can collapse during the process. Active materials in the form of conductive polymer composites are incorporated by embedding in the preform and co-drawing. Due to their elastic nature even at elevated temperatures they introduce a difficulty in the process that increases with the cross-sectional area ratio of composite to substrate. The rheological criteria that apply to composites are discussed in

Chapter 3. Metals can be introduced by injection for liquid metals and by feeding for solid metallic wires. For feeding, note that the highly heat conductive metallic wires act as heat sinks and set temperatures are usually significantly higher compared to the drawing in absence of the wires. Finally, a multitude of other 1D functional elements can be introduced into the fiber through feeding. This includes nylon lines as rigid spines for mechanical support, optical fibers for light guiding, and tubing for targeted transfer of fluids or mechanical tools.

2 Compressible fibers for large-area sensing of pressures

Based on the presented materials and process platform, we demonstrate a first type of fiber-based device for the sensing of pressures. The electromechanical functionality of the fibers relies on a conductive polymer composite and a thermoplastic elastomer, acting as building blocks arranged in rationally designed cross-sectional architectures. The mechanism of pressure detection and localization is inspired by a previous work, where hard thermoplastics were employed [19]. By extending this concept to a soft fiber, the device performance is significantly improved. Moreover, the use of soft and elastic materials enables the pressure-sensing mechanism to be developed further, most importantly by quantifying the pressure intensity. The study of design and structural deformation are the focus of this Chapter. Parts of the presented work are also published elsewhere [15].

2.1 Motivation

Pressure sensing plays a key role in the current technological advancement of functional soft surfaces and textiles with applications in health care [50–53], sports [54, 55], and human-machine interaction [56, 57]. In particular, the measurement of pressures exerted by the human body on surfaces, such as seats or beds, represents an important benefit to health monitoring, as it can contribute to the prevention of pressure ulcers and the surveillance of motion patterns during sleep or physical exercise of patients. However, besides secondary requirements such as robust, long-term functioning, washability, and low cost, the design of integrated textile pressure sensors is challenging because the surfaces to be functionalized are large and relevant pressures ranges are small.

In recent efforts, the coupling of conductive nanomaterials, including metal nanowires [58, 59] and carbon nanotubes [60–64], with soft materials, such as polydimethylsiloxane [63, 64] or cotton fabric [62], has led to a multitude of micro-electromechanical devices that are conformable and flexible. Pressure sensing with these deformable material constructs is typically achieved through changes in resistance [58, 62–64], capacitance [60, 61], piezoelectricity [65], or triboelectricity [59]. Often with the help of micro-structuring [60, 63, 64] excellent sensitivi-

ties, low detection limits, and large measurable ranges were achieved. However, presented prototypes remain at a small scale – generally a few square centimeters of surface area – which hinders the integration in large fabrics or skins. Moreover, the devices consist of 0-dimensional sensing elements, i.e. point sensors without spatial resolution, for which pressure localization can only be achieved through arrays of discrete sensors. Such systems necessitate numerous electrical contacts and wires within the area exposed to pressures, which are particularly susceptible to failure in flexible substrates, as well as extensive data collection and processing.

In contrast to standard 0-dimensional devices, functional fibers represent an advantageous alternative strategy towards large-area pressure detection and localization, because they are typically fabricated in large lengths, can be seamlessly integrated into textiles and, most importantly, enable distributed sensing [66]. With the proper design, they can enable the functionalization of large areas with a drastically reduced number of required electrical connections or optical coupling placed outside the area of interest [67–69], leading to improved robustness and reduced manufacturing costs. Particularly promising are fibers originating from the thermal drawing process, because this technique allows the simultaneous processing of conductive and insulating materials into fibers of extended lengths, fine architectures, and sophisticated functions, including pressure sensing [6, 9, 19, 22]. Thus far however, fiber designs with conducting polymer composites were limited to simple symmetric designs which prevented the simultaneous detection of pressure location and pressure level. Moreover, the in-depth understanding and modeling of the mechanical deformation of soft multi-material constructs, which are essential to control pressure sensing functionalities, remain to be developed. As a result, the integration of such smart fiber assemblies into large-area fabrics for pressure sensing has not been demonstrated to date.

In this Chapter, we present the design and scalable manufacture of compressible and conductive fibers, which can detect, quantify, and locate mechanical pressures along their entire lengths. The thermally drawn fibers are constituted of polymer composite electrodes arranged in a novel asymmetric architecture within a soft thermoplastic elastomer support. Taking advantage of the elastic structure, the fibers can be reversibly compressed, resulting in the selective contacting of electrodes within the fibers at distinct pressure levels. This experimentally demonstrated functioning of the fiber devices is supported by finite element analysis to show the level of control and engineering of the pressure ranges and sensitivity that can be achieved through application-targeted fiber structures. Using only simple resistance measurements, kPa-scale pressures applied on the meter-long fibers are both reliably quantified and located. This enables the facile functionalization of large surfaces without the need of typically employed sensor arrays. Specifically, we demonstrate the potential of such fibers in large-area pressure sensing by integrating them onto a gymnastic mat for the monitoring of human body position, posture, and motion.

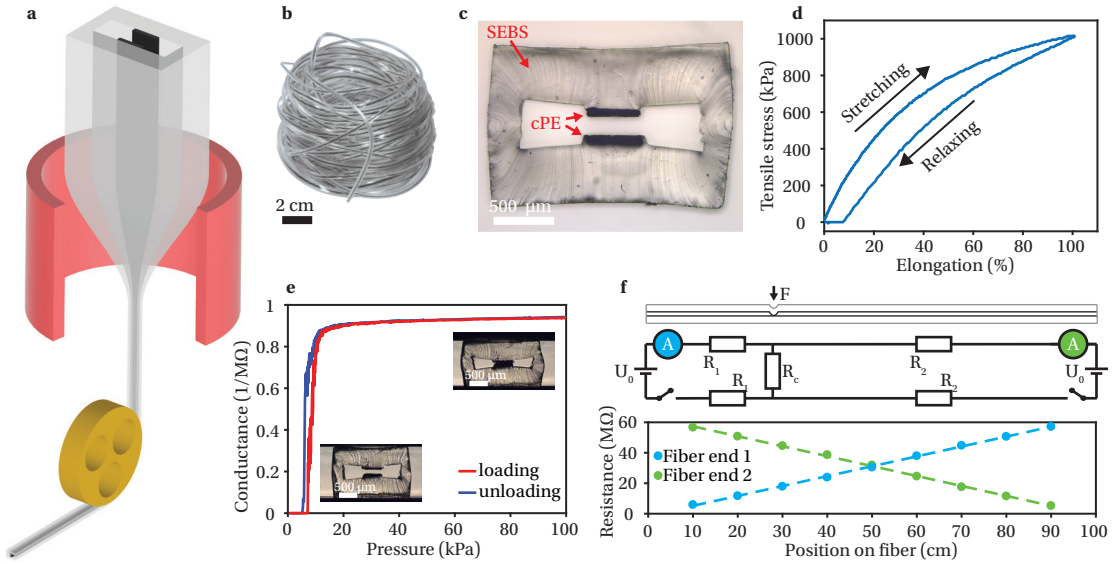

Figure 2.1 – Materials, fabrication and principle of operation of pressure-sensing fibers. a) Schematic of thermal drawing process for the fabrication of multi-material fibers. b) Roll of 15 m of continuous fiber, demonstrating the scalability of thermal drawing. c) Optical micrograph of a fiber cross-section. Two conductive cPE sheets are arranged opposite to one another in a soft SEBS support structure. d) Stress-strain curve of SEBS obtained by tensile testing to 100 % strain and back. The thermoplastic elastomer is soft (Young's modulus of 2.89 ± 0.01 MPa) and nearly elastic (remnant deformation 8 %). e) Compression test of the fiber, while simultaneously applying a voltage between the two cPE sheets and measuring the conductance at one fiber end. The insets show optical micrographs of the fiber in the relaxed and compressed state at which the cPE sheets are separated or in contact, respectively. f) Schematic of the fiber with a compressed section and resulting equivalent circuit. A voltage (U_0) is applied and a current is measured at either fiber end. The electrical load of the circuit is the sum of the resistances of the cPE sheets ($2 \cdot R_1$ or $2 \cdot R_2$, when considering the left or right fiber end, respectively) and the contact resistance between the two sheets (R_c). The total resistance increases linearly with the distance of the mechanical stimulation from the fiber end. Measurements from both fiber ends enable the simultaneous detection of two pressure points on the fiber.

2.2 Fabrication of compressible and conducting fibers

The thermal drawing technique is ideally suited for the co-processing of various materials into long fibers with complex architectures. In this process, polymer granules or thin sheets are first hot-pressed into geometrically defined components, which are subsequently assembled and consolidated into a preform. In the quintessential final processing step, the preform is thermally drawn into a multi-material fiber (Figure 2.1a). Even when composed of different materials and including an empty channel at its center, the resulting fiber maintains the same architecture as in the preform, while being much smaller in cross-sectional dimensions and larger in length. Additionally, the scalable process allows the fabrication of extended lengths of fibers in a few hours of operation (Figure 2.1b).

We identified carbon black-loaded polyethylene (cPE) and poly[styrene-b-(ethylene-co-butylene)-b-styrene] (SEBS) as suitable active and substrate materials, respectively, in pressure-sensing

fibers. While both materials share the processing attributes necessary for thermal drawing – high-viscosity material flow at elevated temperatures – and form an intimate interfacial bond in the fiber (Figure 2.1c), they exhibit vastly different sets of electrical and mechanical properties. Due to the formation of a percolated network of conductive fillers within a thermoplastic matrix, cPE is a conductive (ρ = 3 Ω.m) and rigid material. On the other hand, the thermoplastic elastomer SEBS is an insulator and exhibits large elastic deformability. To characterize the mechanical behavior of SEBS, we performed tensile testing experiments on a slab of material (Figure 2.1d), yielding a Young's modulus of 2.89 ± 0.01 MPa in the linear regime. In these tests, the samples were strained up to 100 % and subsequently released. Even after being exposed to such extreme strains, the material almost entirely recovered its original shape during unloading. A remnant deformation of 8 % when the load was fully removed was the result of viscous and plastic deformation contributions. Thus, being both soft and highly elastic, SEBS is an attractive material choice in applications where large and repeated deformations under low loads are required [9, 70, 71].

2.3 Pressure detection and localization on fibers

The particular properties of cPE and SEBS can be exploited for pressure sensing in fibers. In a first example, two parallel sheets of cPE were embedded within a SEBS support structure and drawn into a fiber (Figure 2.1c). In the relaxed state, the two exposed faces of the conductive sheets are separated by an air gap. When mechanical pressure is applied on the fiber, the SEBS structure collapses and the two cPE conductors come in contact, practically closing an electrical circuit. Upon removal of the load, the structure relaxes, reverting back to its original state. We quantified this mechanism by subjecting the fiber to a pressure ramp while simultaneously applying a voltage between the two cPE sheets and monitoring the conductance at one fiber end (Figure 2.1e). At a threshold pressure of 7 kPa, the conductance abruptly jumped from 0 to 0.9 $M\Omega^{-1}$. A further increase in pressure resulted in only a small increase of conductance of 0.06 $M\Omega^{-1}$, which was attributed to a variation in contact resistance. The subsequent unloading showed that the electrical response was entirely reversible with only a small hysteresis effect, quantified by a maximum pressure discrepancy of 3 kPa.

The significant and reversible electrical response makes the proposed fiber an effective approach for pressure sensing. Particularly advantageous is the soft thermoplastic elastomer fiber structure when compared to traditional thermal drawing materials, such as the thermoplastics polysulfone and poly(methyl methacrylate), as it allows the reversible compression of a fully enclosed structure and signal triggering at kPa-scale pressures, which are relevant for applications in health monitoring [72]. The most important feature of the pressure-sensing fibers, however, is that resistance measures can be traced back to the locations where a pressure is applied on the fibers. The working principle becomes apparent when considering the equivalent circuit of the fibers (Figure 2.1f). The electrical load of the circuit is made up of three resistances in series: the two internal resistances of the cPE sheets and the contact resistance between the sheets. The resistance of the two cPE sheets scales with the length of the resistive

element that the current must travel through. Indeed, we found a linear increase in resistance as a point pressure was applied at positions farther away from the interrogated fiber end. Evidently, this relationship is ideal for the localization of pressures on fibers. In this sensing scheme, the sensitivity is simply the quotient of the cPE resistivity and the cross-sectional surface area of the strips, both of which are constant for a uniform fiber, and amounted here to 0.6 $M\Omega.cm^{-1}$.

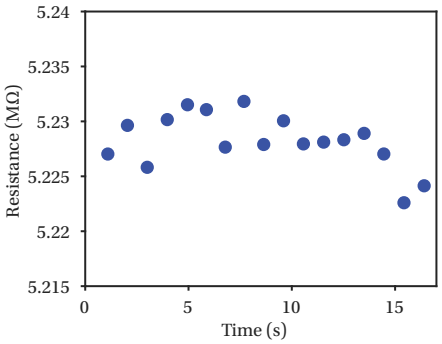

Figure 2.2 – Fluctuations of the resistance measurement for a fiber compressed at a point distanced 10 cm from the fiber end.

The contact resistance represents an source of uncertainty of the sensor. Over the considered pressure range of 7 kPa - 100 kPa a change in conductance attributed to variation in contact resistance was determined to be 0.06 $M\Omega^{-1}$ (Figure 2.1e). This corresponds to a change in resistance of 0.07 MΩ. Using the sensitivity of the fiber-based sensor of 0.6 $M\Omega.cm^{-1}$ (Figure 2.1f), the variation in contact resistance can be translated to an uncertainty in position of 1.2 mm. Another error originates from fluctuations of the resistance at a given, fixed pressure due to the measurement instrument. To quantify this error, the fiber was compressed at a fixed pressure above the triggering threshold at a distance of 10 cm from the interrogated fiber end and the resistance recorded over 15 s (Figure 2.2). This error is highly dependent on the employed electrical characterization instrument. A Keithley Sourcemeter 2400 was used in this experiment. The spread of measured resistances amounted to 0.01 MΩ, which translates to an uncertainty in position of 0.2 mm. For lengths of fibers on the scale of meters, which are employed in the large-area applications considered here, these errors are negligible. Changes in resistance readings induced by environmental factors, including temperature, strain, and humidity, which can result in more significant errors in localization, are discussed in section 2.5. Note that the fiber sensors are truly distributed sensors that can respond to pressure with such resolution at any point along their entire length. Finally, the capability of the sensor can be extended by applying a potential and measuring a resistance alternately from either fiber end. With this technique, two pressure points can be simultaneously detected and located on the fibers [19].

2.4 Sensing of pressure level with customizable multi-electrode fiber architectures

Having devised a technique to detect kPa-range pressures applied on meter-long fibers, we now turn to the challenge of simultaneously locating and quantifying a pressure event beyond a simple binary output. To address this task, we developed an alternative fiber architecture, while employing the same materials used above (Figure 2.3a). In this modified design, three small cPE sheets of width 200 μm were arranged opposite to a large cPE sheet of width 1300 μm set on an incline. The mechanical behavior of the fibers was investigated by applying a pressure ramp (Figure 2.3b). As the compressive load was increased, the top electrodes came into consecutive contact with the inclined bottom electrode, each contact event triggering an individual electrical signal at a distinct pressure level. Also in this configuration, an abrupt increase in conductance was followed by a negligible further change at increasing pressures. Presumably due to the larger deformations in the structure compared to the fiber structure presented above, a more pronounced hysteresis in the loading and unloading paths resulted in a maximum deviation of 15 kPa between the trigger and release pressures. Remarkedly, each electrode retained its dependency on the location of the applied pressure (Figure 2.3c). Similarly to the previous fiber example, the interrogation from both fiber ends enables the localization of two pressure points along the fiber for a given top electrode-ground electrode combination (i.e., pressure level). Thus, in the current design of a fiber with three top electrodes, a total of six pressure points can be resolved. A limitation in this localization scheme is that points of higher pressure must be distanced further from the interrogated fiber ends than points of lower pressure. However, in most load settings, such as a body on a surface, the highest pressure is generated at the center and decreases towards the extremities, and the fibers can thus be employed unrestrictedly.

To further explore the mechanism underlying this mechanically induced signal triggering, we performed a finite element analysis (FEA) of the fiber structure using Abaqus/Explicit. The simulation was evaluated by comparing the mechanical response of the compressed fiber structure obtained through experimentation and the FEA, and an excellent agreement was found (Figure 2.3d). The FEA results indicate that the mechanical behavior of the fibers can be divided into four distinct regimes, each separated by the consecutive contact events of the electrodes. (i) At low pressures, the entire applied load is carried by the two side walls of the open channel. As the pressure is increased, the walls bend progressively, and, eventually, the first top electrode comes in contact with the ground electrode. (ii) With additional loading, there is an increase of the stiffness of the fiber structure, as indicated by the slope of the pressure-displacement curve, given the combined effect of the bridge generated by contact of the first electrode and the continued bending of the side walls. Similarly, further stepwise increases in the stiffness occur during regimes (iii) and (iv), associated with the subsequent contacts of the second and third electrodes, respectively. Note that the maximum principal logarithmic strain in the structure rises to values as high as -0.4 (the negative sign signifies that the associated strains are compressive). These large strain values highlight, once more,

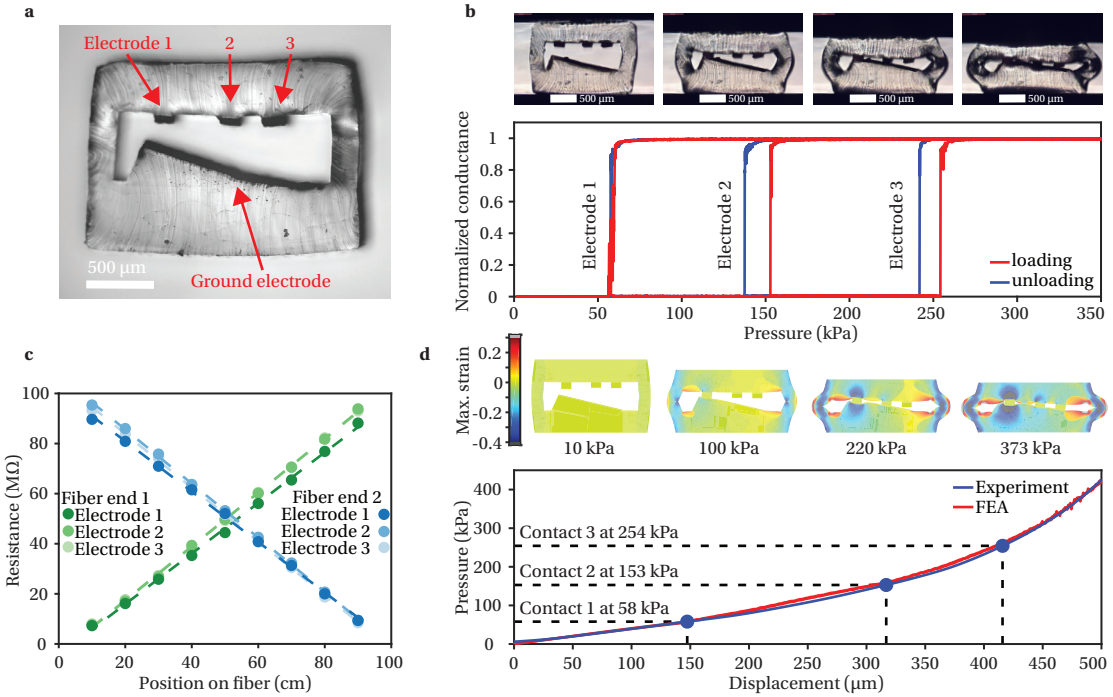

Figure 2.3 – Fibers for the detection of pressure level and location. a) Optical micrograph of the fiber cross-section. Three small conductive cPE sheets are arranged opposite to a large inclined sheet in a SEBS support structure. b) Optical micrographs of the fiber cross-section under increasing pressure. The consecutive contact of the electrodes results in an abrupt increase in the corresponding conductance at distinct pressure levels. c) Resistance of the electrode pairs as a function of the position of the pressure on the fiber. The measurement can be performed at either fiber end. d) Finite element analysis of the deformation of the fiber cross-section under increasing pressure, showing the maximum principal logarithmic strain field ε_1 ($|\varepsilon_1| \geq |\varepsilon_2| \geq |\varepsilon_3|$, where ε_1, ε_2 and ε_3 are the three principal logarithmic strains) in the structure at different pressure levels, and the pressure on the fiber structure as a function of displacement. The progressive collapse of the structure is divided into distinct regimes separated by the consecutive contact events of the electrodes. Each additional contact results in an increase in stiffness of the fiber structure.

the necessity of employing the elastomeric material SEBS instead of common thermoplastics, which could not sustain reversibly such high levels of deformation.

The stepwise increase in stiffness of the fiber under compression justifies our choice for the positions of the three top electrodes in the selected fiber design. While one might have been tempted to space these electrodes equidistantly, such an architecture would result in unbalanced pressure levels (Figure 2.4a, b). With the quantitative analysis of the increasing stiffness in compression of the fiber structure, we purposely shifted the position of the second top electrode away from the first and towards the third top electrode. In this non-centered electrode fiber design, signal triggering occurred at equally spaced pressure levels. We anticipate that balanced pressure levels will be preferred for most applications because applied load ranges can be classified evenly. For this reason, all subsequent experiments were performed on fibers with three top electrodes, which are triggered at the representative pressure levels of

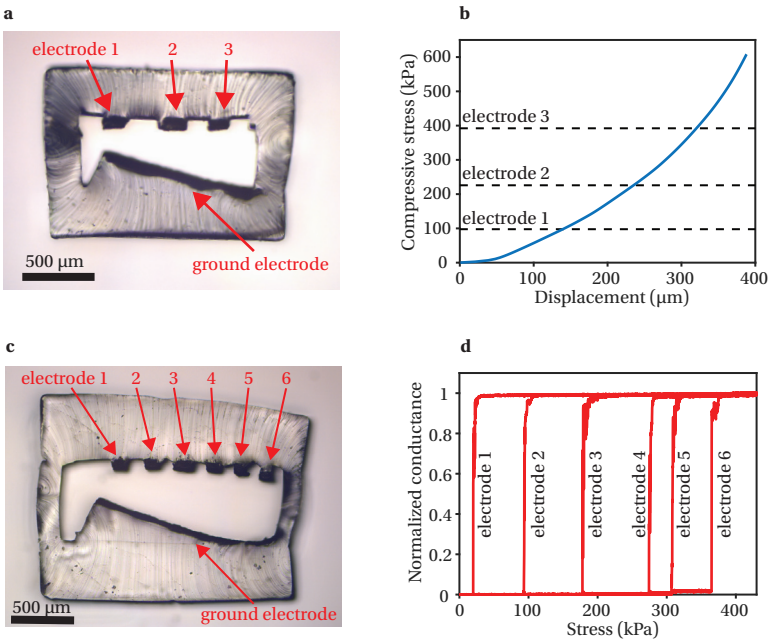

Figure 2.4 – Alternative designs of pressure-sensing fibers. a) Optical micrograph of the fiber cross-section with three equidistant top electrodes. The gap separating the three top electrodes from one another is approximately equal. b) A pressure is applied on the fiber with equidistant electrodes by an indenter. The displacement and the resulting compressive stress are recorded. The pressures at which the electrodes are triggered are indicated. Due to the increase in stiffness of the structure, the equidistant electrodes result in unbalanced signal trigger pressures. c) Optical micrograph of the fiber cross-section with six top electrodes. d) Compression test of the fiber with six pressure levels while simultaneously applying a voltage and measuring the conductance at the fiber end. The six electrodes are consecutively triggered, indicated by an abrupt increase in conductance, as the pressure on the fiber is increased.

50 kPa, 150 kPa, and 250 kPa, noting that triggering at different pressure levels could be readily achieved by adjusting the electrode spacings.

Additionally, the pressure level sensitivity can be tuned through the tailoring of other geometrical aspects of the fiber cross-section, such as the wall thickness, electrode gap, and angle of the ground electrode. The fiber could also be adapted for applications where shear forces in addition to compressive loads are expected. Angled forces can shift the pressures under which the electrodes are triggered and, thus, cause pressure quantification errors. These could be reduced through changes in the fiber structure, such as a reduced electrode gap and thicker side walls. Finally, the number of pressure levels detected by the functional fibers can also be increased by the inclusion of additional electrodes in the design. For example, we fabricated and characterized a fiber with six top electrodes (Figure 2.4c, d). Note that this increase in pressure resolution also leads to an increase in spatial resolution of a generated pressure map, as each added electrode is accompanied by a signal specifying a pressure location. Overall, the fiber-based pressure sensors that we have developed exhibit a discrete resolution of the pressure level and offer the capability of a continuous pressure location measurement. Our

design can be highly customizable towards specific applications, guided by a parametric exploration of the FEA and implemented through thermal drawing.

2.5 Performance of pressure-sensing fibers

To quantitatively assess the fibers' electromechanical performance, we subjected them to repeated cycles of controlled compression and relaxation while simultaneously monitoring the conductance values corresponding to the three pressure levels. The tests revealed that the electrical response of the fibers to pressure was remarkably consistent and robust (Figure 2.5a). All three pressure levels were triggered and released consecutively within each pressure cycle, and no changes in the conductance profiles were observed going from one pressure cycle to the next. Even after 10 000 cycles, the electrical response remained nearly unchanged. As we envision to use the fibers for pressure-localization applications, we characterized more thoroughly the ultimate output of the fiber-based sensors: the magnitude and position of pressures on the fibers. Firstly, we measured the pressures at which the three electrode pairs were triggered during cycle 1, 10, 100, 1000, and 10 000 (Figure 2.5b). Variations in trigger pressures between different fiber samples were quantified by a maximum error of ±20 kPa during the first cycle. Additionally, fatigue resulted in a maximum decrease in mean trigger pressure of 18 kPa after 10 000 cycles. The quality of pressure magnitude measurement of the fiber-based sensor, limited by intrinsic variations and fatigue, was deemed to be satisfactory, as the calculated errors fall well below the 100 kPa difference of trigger pressure between levels. Secondly, we evaluated the reliability of the fiber-based sensor for determining pressure position. This was achieved by assessing the relationship between the measured position and resistance prior to the fatigue experiment (as shown in Figure 2.1c). Using this calibration curve, recorded peak resistance values for each cycle could be directly translated into position readings. During the fatigue test, we monitored the change in position reading over 10 000 cycles (Figure 2.5c). We found that the localization was highly consistent, quantified by a maximum error in position reading between different fiber samples during the first cycle of ±0.2 mm and a maximum drift of mean position reading due to the repeated deformation of 0.6 mm after 10 000 cycles.

Next, we investigated the response time of the fiber-based pressure sensors to mechanical stimuli (Figure 2.5d). The supported bandwidth represents an important sensor specification, because human body motion can reach frequencies as high as 10 Hz [73]. We compressed the fibers cyclically at frequencies of 1 Hz, 10 Hz, and 20 Hz, and simultaneously monitored the electrical response. Experiments at higher frequencies could not be performed due to limitations of the testing machine. Even at the highest considered frequency of 20 Hz, the fiber followed the motion of the indenter faithfully, and all three pressure levels were triggered and released within each deformation cycle, resulting in a constant signal amplitude.

We also tested the performance of the fiber-based sensors under different environmental conditions, including humidity, temperature, and strain. Proper functioning in variable en-

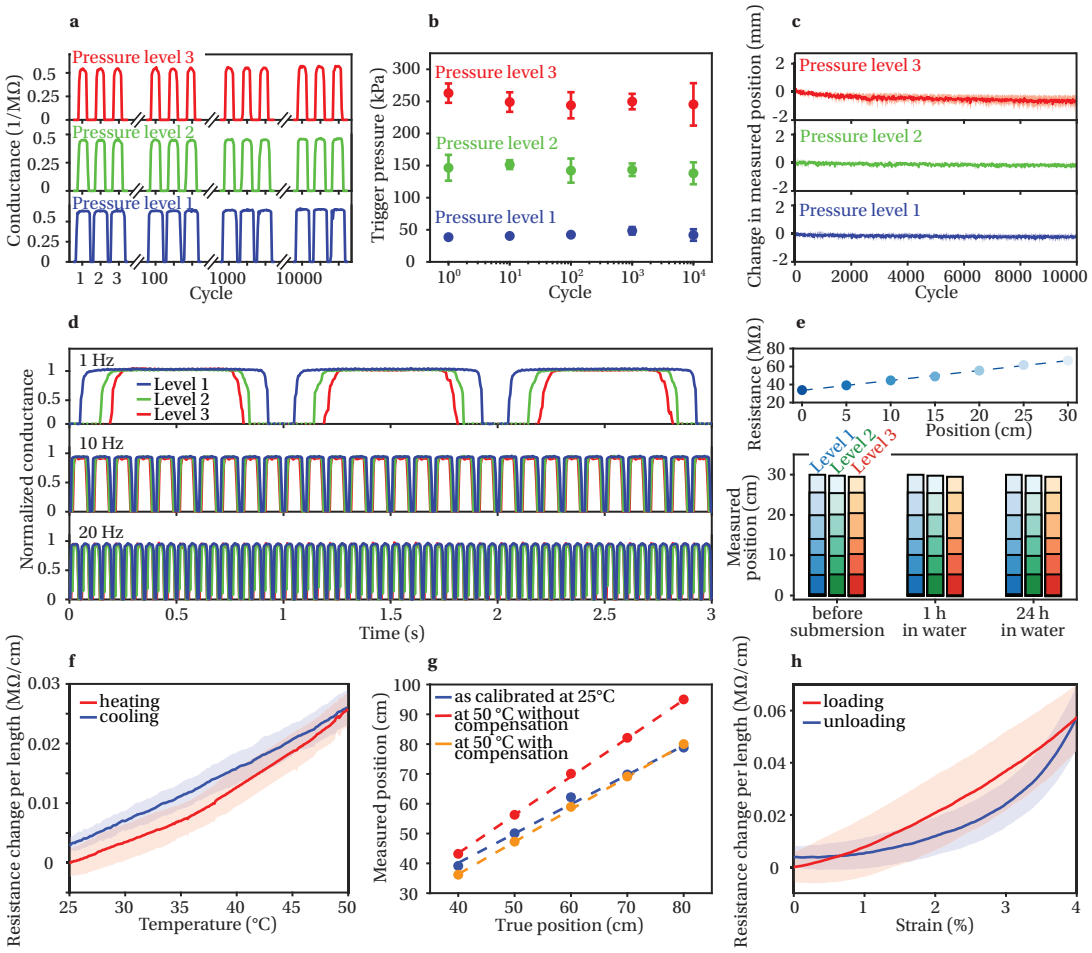

Figure 2.5 – Performance of the pressure-sensing fibers. a) Electrical response of the three pressure level-indicating electrode pairs in the fibers under repeated compression and relaxation for 10 000 cycles. b) Change in trigger pressure of the three electrode pairs as a function of cycle number. c) Change in location reading of the three electrodes as a function of cycle number. The location is calculated using the peak conductance of previously calibrated electrode pairs for each cycle. d) Time-resolved electrical responses of the fibers to compression at different frequencies, illustrating the bandwidth of the sensor. e) Stability of fiber-based sensors under water. The resistances of the electrodes in the fibers are linearly dependent on the position of the applied pressure, shown exemplarily only for one electrode pair. The color shade in the plot is relevant for the subsequent illustration. The positions determined using the calibrated fibers are compared in dry conditions to submersion in water for 1 h and 24 h. The shade of color indicates the true position at which the fibers are compressed, and the height of the bars in the bar chart the measured position determined with the fibers. f) Change in resistance per length of the fiber ground electrode induced by an increase and subsequent decrease in temperature. g) Pressure position determined by the pressure-sensing fibers as a function of true position at the temperature of calibration, at an elevated temperature without compensation, and at an elevated temperature with compensation, reducing the error in pressure localization induced by the temperature effect. h) Change in resistance per length of the fiber ground electrode due to an applied and subsequentially released axial strain.

vironments is an advantageous device property, as the fibers could be exposed to moisture, heat, and deformations during applications involving the human body. Furthermore, practical functional textiles should be machine-washable. First, we tested the fibers' stability in humid environments (Figure 2.5e). In this test, fibers were firstly calibrated and subsequently submersed in a water bath. While being submerged, the fibers were compressed at the predetermined positions and the outputs recorded after 1 h and 24 h in water. A comparison of the positions determined by the fibers revealed that the exposure to water had practically no effect on the functioning of the fiber-based sensors, validating their robustness in humid environments. To investigate the effect of temperature on the functioning of the fiber-based sensors, we applied a controlled temperature ramp to the fibers while monitoring the resistance of the ground electrode end-to-end (Figure 2.5f). An increase in temperature from 25 °C to 50 °C resulted in a resistance difference per fiber length of 0.025 $M\Omega.cm^{-1}$. This increase in resistance was found to be almost entirely reversible, quantified by a remnant change in resistance per length of 0.003 $M\Omega.cm^{-1}$. While the difference in resistance induced by a change in temperature scales orders of magnitudes below the sensitivity of the pressure localization (approximately 1 $M\Omega.cm^{-1}$), it could reduce the accuracy of the fiber-based sensor for large temperature differences and exposed fiber lengths. Thus, we tested the functioning of the fibers at an elevated temperature of 50 °C (Figure 2.5g). In this test, fibers were firstly calibrated regarding their pressure position-resistance relationship at room temperature. After heating the fibers from 25 °C to 50 °C, pressures were once more applied at the same predetermined positions and the resulting resistance readings directly converted using the calibration curves obtained at room temperature. Indeed, the significant temperature rise induced a non-neglectable error in the localization of pressures of up to 15 cm.

However, thanks to the multi-electrode design of the pressure-sensing fibers, the resistance change can be compensated through the introduction of a temperature correction factor. In contrast to the pressure localization, which is determined through electrical interrogation between electrode pairs at one fiber end, this factor is established by monitoring the resistance of a single electrode end-to-end. The resistance R_0 of a single electrode 1 at the calibration temperature T_0 is:

$$R_{1,0} = \frac{\rho_0}{S} l, \tag{2.1}$$

where ρ_0 is the resistivity at T_0 and S the cross-sectional area of the electrode. A change in temperature results in a change in resistivity [74]:

$$R_1(T) = \frac{\rho(T)}{S} l. \tag{2.2}$$

By combining equations 2.1 and 2.2, the temperature-dependent resistivity can be expressed as:

$$\rho(T) = \rho_0 \frac{R_1(T)}{R_{1,0}}. \tag{2.3}$$

The resistance of an electrode pair 1 and 2 used for the localization of pressures at a pressure position x is given by:

$$R_{12}(x) = \frac{\rho}{S_1}x + \frac{\rho}{S_2}x. \tag{2.4}$$

The equation can be rearranged, and the position expressed at the calibration temperature by:

$$x_0(T) = \left(\frac{\rho_0}{S_1} + \frac{\rho_0}{S_2}\right)^{-1} R_{12}. \tag{2.5}$$

The slope of the linear function is the coefficient c that is determined during calibration:

$$x_0(R_{12}) = c \cdot R_{12}. \tag{2.6}$$

However, at an elevated temperature this coefficient is no longer valid and the position changes to:

$$x(R_{12}, T) = \left(\frac{1}{S_1} + \frac{1}{S_2}\right)^{-1} \frac{1}{\rho(T)} R_{12}. \tag{2.7}$$

We now substitute equation 2.3 in 2.7

$$x(R_{12}, T) = \left(\frac{1}{S_1} + \frac{1}{S_2}\right)^{-1} \frac{R_{1,0}}{\rho_0 R_1(T)} R_{12}. \tag{2.8}$$

In this case, the coefficient c can once more be used:

$$x_0(R_{12}, T) = c\frac{R_{1,0}}{R_1(T)} R_{12}. \tag{2.9}$$

Thus, the position of a pressure, determined by the resistance of an electrode pair, can be continuously corrected at any temperature with the measure of the resistance of a single electrode along the fiber length. With this temperature correction factor, the calibration curve can be continuously adjusted for any given temperature. Using this compensation scheme, the temperature-induced error could be significantly reduced to a maximum value of 3 cm, and pressures localized without recalibration at elevated temperatures (Figure 2.5g). The actual temperature change or even the source of the resistance change must not be known for the compensation as long as the fiber is uniformly exposed to it. Note also that the electrode used for the monitoring of temperature-induced resistance changes must not necessarily be one involved in the pressure localization but could also be a separate electrode integrated within the fibers.

As a final environmental stimulation, we characterized the effect of an axial strain applied along the fibers (Figure 2.5h). In this test, the resistance of the ground electrode end-to-end was measured while the fibers were elongated to 4 % and subsequently released. While the electrode remained conductive even at elevated strain levels, a resistance difference per

fiber length of up to 0.057 $M\Omega.cm^{-1}$ was found. Also in this case, the effect was reversible resulting in a remnant resistance change per length of 0.004 $M\Omega.cm^{-1}$ after unloading. As a longitudinal strain is expected to affect all electrodes uniformly, the same compensation scheme introduced for the temperature effect could be employed to reduce the error in pressure localization applications where longitudinal strains are to be expected. More complex modes of deformation, such as fiber bending, could also perturbate the correct functioning of the fiber-based sensors. However, as only applications of the fibers on flat surfaces are envisioned, the analysis bending-induced errors goes beyond the scope of this work.

2.6 Pressure-sensing fibers in gymnastic mat for body monitoring

To demonstrate the potential of fiber assemblies in large-area pressure sensing applications, we integrated multiple fibers onto a gymnastic mat for the monitoring of body position, posture, and motion (Figure 2.6a). We placed eight fibers strategically on the mat at positions where the highest body pressures are expected, including the head, shoulders, tailbone, and heels. The four electrodes at each fiber end were connected to a custom circuit board using electrical wires, and a microcontroller was used to interrogate the fibers. The prototype highlights two key aspects of the fiber technology: firstly, the outstanding throughput of thermal drawing, even at a laboratory scale, as the fiber used to functionalize the entire surface of 180 cm x 60 cm was obtained from a single drawing experiment; secondly, the number of electrical connections, which is orders of magnitude lower than what would be needed to functionalize such a surface with 0-dimensional sensors. To directly output pressure positions during use, the fibers were calibrated before testing the device. This procedure consisted of compressing each fiber at five predetermined points and correlating the measured signals to the true positions.

The performance of the calibrated device was subsequently evaluated by having a volunteer lie on the mat in different positions, and continuously recording signals generated by all fibers (Figure 2.6b). The signals of the sensor system, shown here only for the fifth fiber from the top as an example, proved to be stable. Signals collected from all fibers were translated to positions using the calibration curves. To make the gathered data more accessible to users, the readings were visualized in pressure contour plots that were automatically generated in real-time. In these, the displayed pressure areas are defined by the two position readings obtained for every fiber and pressure level and are thus a representation of only the pressure profile of the body. While an increase in pressure within the outer determined body profile will be detected through the triggering of another electrode pair, a decrease will not, which is a limitation of our fiber-based sensor. Nonetheless, as shown by the close correlation to the photographs of different body positions, the pressure plots can be used to determine body position, posture, and movement. Moreover, the location of an exceedance of a threshold pressure is easily picked out on the graphics. Knowledge of a critical pressure location over time is crucial in assessing the risk for the formation of bedsores [75]. We also tested the device dynamically by asking a volunteer to walk on the mat as well as lie on it and shift between

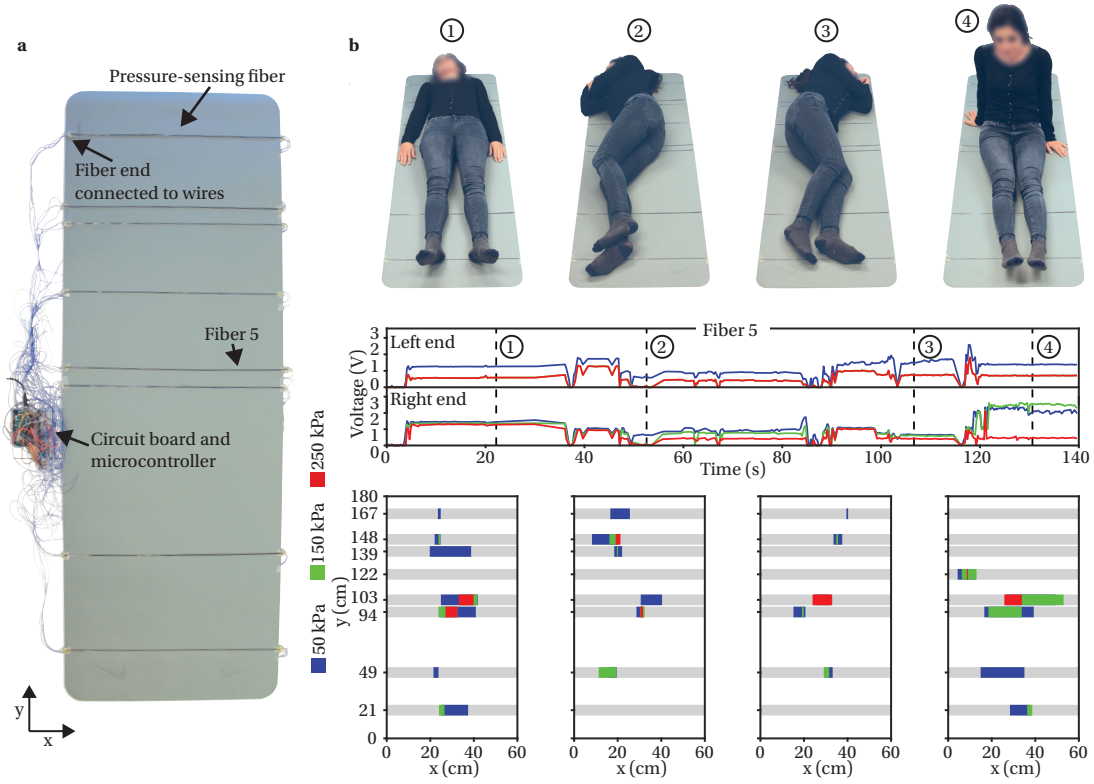

Figure 2.6 – Fibers in human body posture and motion monitoring. a) Eight pressure-sensing fibers are integrated on a gymnastic mat. The electrodes exposed at the fiber ends are connected to a circuit board and are interrogated by a microcontroller. Fiber 5 and a coordinate system are shown, which are relevant for subsequent illustrations. b) Photographs of a volunteer lying on the gymnastic mat in different positions labeled 1 to 4. The raw outputs of fiber 5 as a function of time for the entire test, including shifts from one body position to the next, are shown as an example. The pressure level is indicated by the number of electrodes that are triggered, while the distance of the pressure position to the fiber end is quantified by the signal value. The times at which photographs were taken are indicated on the plot. Automatically generated pressure contour plots are obtained by processing the data collected by all fibers with the help of previously determined calibration curves. Displayed pressure areas are defined by the two position readings obtained for every fiber and pressure level and are thus a representation of only the pressure profile of the body.

different body positions (the video is available at https://onlinelibrary.wiley.com/doi/abs/10.1002/adfm.201904274).

Pressures could be resolved temporally and spatially, and body movements on the mat were accurately represented in pressure visualizations. The results suggest that the fiber-based monitoring system presented here allows for the detection of surface occupancy, assessment of body posture and kinematics, and localization of exceedance of critical pressures. In this application, we employed fibers with trigger pressures of 50 kPa, 150 kPa, and 250 kPa. However, as previously discussed, the trigger pressures can be tailored to the specific information of interest through targeted changes in the fiber geometry. Furthermore, the quality of the pressure measurement over the large area could be further improved through the inclusion

of a higher number of fiber-based sensors, resulting in a larger coverage. The information obtained through the system could be particularly useful in health care, such as pressure ulcers prevention and surveillance of sleep patterns or physical exercise, but also in more general body pressure measurements, such as car seat occupancy measurements, detection of falls of elderly people, and monitoring of foot traffic.

2.7 Omni-directional pressure-sensing fibers in an untethered smart fencing jacket

Next to the presented functional gymnastic mat, we explored the application of our pressure-sensing fibers in a fencing jacket for the detection and localization of a hit on the body during the combat. As the requirements for this application are significantly different, several changes to the fiber design and integration were implemented.

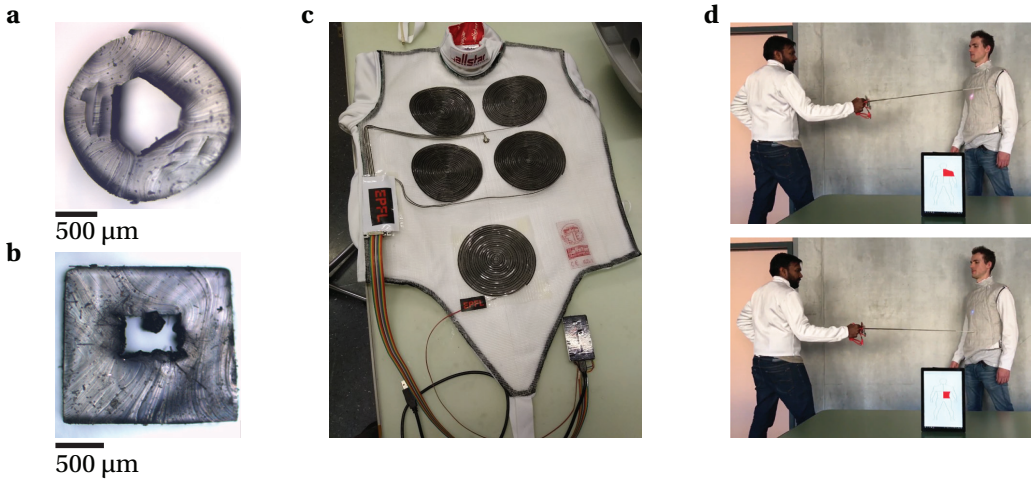

Figure 2.7 – Omni-directional pressure-sensing fibers in an untethered smart fencing jacket. a) Fiber cross-section including three composite electrodes arranged triangularly inside an empty channel, enabling omni-directional pressure detection. b) Alternative fiber cross-section, where a small composite electrode is surrounded by a larger U-shaped electrode. c) Smart fencing jacket prototype with five pressure-sensing fibers arranged in spirals, as well as peripheral electronics unit for signal collection and wireless transfer to a remote central unit. d) Demonstration of the smart fencing jacket. The location of a hit on one of the functional zones is visualized on a near tablet in real-time.

In fencing, a hit is defined by any touch with the sword tip with a pressure that exceeds a defined threshold. Thus, the fiber should be triggered at pressures above the threshold value, but quantifying the pressure in excess is not necessary. Thus, the multi-electrode fiber architecture is not suitable for this application. However, in order to assure a sufficiently high hit detection rate, the surface of the fencing jacket must be densely functionalized with an inter-fiber spacing that is smaller that the diameter of the round sword tip. Realizing such a high surface coverage can only be accomplished with high-throughput textile techniques, such as embroidering or knitting. In most of these processes, fiber orientation cannot be controlled.

Thus, the fiber should be responsive to pressures regardless of the direction of the applied force. None of the fiber designs reported thus far includes such an omni-directional sensitivity. To achieve this feat, two novel fiber design were conceived. The first fiber architecture consists of a round SEBS cladding with three cPE electrodes that are arranged triangularly inside an empty channel (Figure 2.7a). A force that is applied from any direction on the fiber results in the contacting of two of the electrodes. A disadvantage of this design is that the resistance between any of the three electrode couples must be continuously monitored. As this causes severe implementation issues, a alternative fiber design was developed, where one small electrode is surrounded by a large U-shape electrode within a square cladding (Figure 2.7b). This two-electrode design exhibited promising pressure-sensing potential in trials with random orientations and was selected for subsequent testing and implementation in the jacket.

To realize a first smart fencing jacket prototype, we glued five fibers arranged in individual spirals onto a textile overlay for the jacket (Figure 2.7c). Thus, each fiber spiral corresponded to a spatial zone on the jacket. Each of the five fibers was connected on one end to the peripheral electronics. Unlike the gymnastic mat, the smart fencing jacket is a wearable device and must be untethered. For this reason we integrated a small lithium-ion battery as a portable and rechargeable power source in the electronics unit. Additionally, we established wireless communication using Bluetooth, which allowed the signals collected for each of the fibers to be continuously transferred from the microcontroller to a tablet. There, the signals were treated and visualized in real-time on a digital avatar. As shown in Figure 2.7d, hits on the smart fencing jacket were successfully detected and assigned to one of the zones.

2.8 Conclusion

We have developed compressible and electrically conducting fibers, optimized for the measurement of kPa-scale pressures over m^2-scale surface areas. The fibers consist of conductive polymer composite electrodes arranged within a hollow, soft thermoplastic elastomer support and are fabricated by the scalable thermal drawing technique. A mechanical pressure on the fibers results in the selective and reversible contacting of electrodes, generating an electrical signal. We showed that the fibers perform as accurate, time-responsive, and robust sensors of both pressure magnitude and location. Moreover, the fibers are customizable, as the electrical response to mechanical stimuli can be tuned through targeted changes in the architecture, enabling control of trigger pressures as well as resolution of pressure level and location. The developed fiber-based sensors stand out among standard pressure sensing strategies, such as piezoresistivity, because the discrete rather than continuous pressure level measurement is inherently impervious to noise and drift. Moreover, the fibers act as distributed sensors for the functionalization of large surface areas and enable pressure localization without the need of typically employed grids of 0-dimensional sensors, thus drastically reducing the number of failure-susceptible electrical connections. This was demonstrated by integrating the pressure-sensing fibers on a gymnastic mat, with which human body position, posture, and motion was captured. We anticipate that this robust, cost-effective and easily implementable technology

can significantly contribute to health monitoring of patients prone to pressure ulcers, and anywhere else where pressures on large surfaces need to be assessed reliably.

2.9 Experimental section

Mechanical and Electrical Testing of Materials

The mechanical behavior of SEBS (Kraton) was investigated by tensile and compression testing with a standard frame (Mecmesin Multitest 2.5-i) and load cell (Mecmesin Basic Force Gauge). In tension, samples of dimensions 40 mm length, 24 mm width, and 5 mm thickness were tested and in compression samples of dimensions 20 mm length, 24 mm width, and 24 mm thickness. The displacement was set to 300 mm.min^{-1} and 1 mm.min^{-1} for tensile and compression testing, respectively. The resistivity of cPE (Goodfellow) was obtained by performing resistance measurements with an electrical testing instrument (Keithley Sourcemeter 2400) in four-probe configuration at a current of 100 μA.

Fiber Fabrication

First, granules of the polymers were hot-pressed (Lauffer Pressen UVL 5.0) into geometrically defined components. Next, the parts of different materials were assembled into a fiber preform, where a machined polytetrafluoroethene core was placed at its center to create the empty channel. The preform was consolidated in the hot press and the core was subsequently mechanically removed. Finally, the preform was drawn into a multi-material fiber with a custom draw tower.

Structural and Electro-mechanical Analysis of Fibers

The cross-sections of the fibers were examined by light microscopy (Leica DM 2700 M). To investigate the fibers' electrical response to pressure, the exposed electrodes at the fiber ends were contacted using electrical wires and silver paint. Resistances were measured using the Sourcemeter at a set current of 100 nA for two-electrode fibers, and with a microcontroller (Arduino Uno) for simultaneous measurements of multiple fiber electrode pairs at an applied voltage of 5 V in a voltage divider circuit with a 10 MΩ reference resistance. In the compression test, 100 mm-long fiber samples were compressed between two plates of diameter 15 mm using a dynamic mechanical analysis setup (DMA, TA Instrument DMA Q800), with which displacement and force were measured. To evaluate the correlation between pressure position and electrical response of the fibers, 1 m-long fiber samples were compressed locally with a rod of diameter 5 mm. For fatigue testing, 100 mm-long fiber samples were repeatedly compressed in the DMA at a frequency of 5 Hz and the conductance measured continuously for all three electrodes over 10 000 cycles. A position value was calculated for each cycle from the peak conductance values using the previously determined calibration curves. The

same test was repeated with interruptions at cycles 1, 10, 100, 1000, and 10 000, where a controlled pressure ramp test was applied to determine the variation in trigger pressure of the electrodes. To determine the mechanical bandwidth of the fiber-based sensors, fiber samples were stimulated in the DMA at frequencies 1 Hz, 10 Hz, and 20 Hz, and the electrical response recorded with an oscilloscope (Digilent Analog Discovery) in the voltage divider circuit. To investigate the functioning of the fibers in water, 0.5 m sections of 1 m-long fiber samples were submerged in a tray filled with water. The fibers were compressed locally at predetermined positions with the rod, and the resistance measured with the Sourcemeter. To characterize the effect of temperature, fibers of length 1 m were placed on a hot plate and the temperature monitored with a thermocouple coupled to a multimeter (Keithley DMM7510). Pressures were applied at predetermined positions with the rod, and resistance measured with the Sourcemeter. The effect of strain was assessed by elongating fibers of length 30 cm using the tensile testing stand and resistance simultaneously monitored with the Sourcemeter.

Finite Element Analysis

We performed FEA simulations using the commercial package Abaqus/Explicit, which offers a more efficient and robust convergence performance in simulations involving complex contact geometries compared to Abaqus/Standard. Given that the cross-section of the undeformed fiber is uniform along its length, the structure was simplified to a plane stress (2D) model (Figure 2.8). The efficiency and robustness of the simulations were further increased by simplifying the geometry of the fiber cross-section, obtained by light microscopy, while keeping its key features. The measures of the distances between the three electrodes and the ground electrode were altered to match the displacements during compression experiments, at which an electrical contact was established between electrode pairs. We found these distances to be a more representative value because experimental errors, such as a slightly angled placement of the sample, can result in deviation in the configuration of the sample under test compared to the one observed by light microscopy. The two side walls of the open channel are initially curved with a maximum deviation of 60 μm at the outer surfaces. An arc-shaped imperfection with a radius of 80 μm, which is filleted and smoothly connected to the straight edge, is added at the middle of the inner surface of each side wall to model the permanent deformation formed during creasing [76], where high compressive strains are localized.

Considering the nonlinear mechanical behavior of the thermoplastic elastomer used, the SEBS material was modeled by the incompressible Yeoh hyperelastic material with the strain energy potential $U = C_1(I_1-3) + C_2(I_1-3)^2 + C_3(I_1-3)^3$, where $I_1 = \lambda_2^2 + \lambda_2^2 + \lambda_3^2$ is the first invariant of the right Cauchy-Green deformation tensor, and λ_1, λ_2 and λ_3 are principal stretches. The material constants $C_1 = 482.2 \pm 1.8$ kPa, $C_2 = -82.8 \pm 2.2$ kPa and $C_3 = 11.3 \pm 0.8$ kPa were determined by performing uniaxial tension and compression tests on SEBS. The material of the electrodes cPE was assumed to be a linear elastic material with a Young's modulus of 157 MPa determined by tensile testing (REFERENCE TO FIGURE). The contact between any two surfaces (or self-contact) was assumed to be a general contact without penetration and

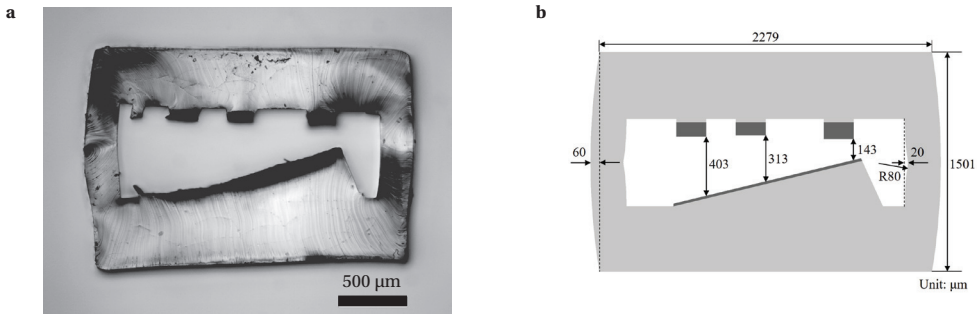

Figure 2.8 – Geometry of the fiber cross-section a) measured by light microscope and b) simplified in the FEA. The key dimensions are indicated on the schematic.

friction. The model was discretized by approximately 67,000 CPS4R plane-stress elements with an element size of approximately 6.8 μm. A mesh convergence study was performed to ensure that the element size was sufficiently fine. Geometric nonlinearities were taken into consideration in the simulation. During loading, the bottom face of the fiber was clamped, and the top face was compressed with a prescribed uniaxial displacement that was increased smoothly from 0 to 600 μm in 5 ms and restricted laterally. The kinetic energy was less than 0.5 % of the strain energy, which indicates that the simulations captured the mechanical behavior of the fiber under quasi-static loading conditions.

Fiber-equipped Gymnastic Mat Manufacture

A fiber obtained from a single draw was cut into eight pieces, each with a length of 0.6 m. The exposed electrodes at each fiber end were contacted with silver paint and electrical wires. Next, the fibers were fixed on the gymnastic mat using double-sided tape. The wires originating from all the fibers were connected to a custom circuit board. Each set of two electrodes was connected in series to a reference resistance of 10 MΩ, forming a voltage divider. The fibers were interrogated with a microcontroller (Arduino Mega 2560) by applying a voltage of 5 V successively at each fiber top electrode and measuring the voltage across the reference resistance, which is inversely proportional to the fiber resistance. In this setup, 48 values were recorded at a rate of 4 Hz. Each fiber was calibrated by applying a point pressure at five positions. For each electrode set, the voltage level was directly correlated to a position using a two-term exponential fit.

3 Stretchable nanocomposites in fibers for mechanical sensing

In the previous Chapter, the sensing mechanism was evoked by the structural design, and the materials were essentially used as building blocks rather than active elements of the sensor. In this Chapter, we explore the material itself, more specifically the development of a polymer nanocomposite that is strechtable, conductive, and compatible with the thermal drawing technique. Thus, the focus is on the formulation of such a composite as well as the detailed characterization of relevant microstructural, rheological, mechanical, and electrical properties.

3.1 Motivation

Soft electromechanical sensors have fueled developments in numerous application fields, including health and sports monitoring [77, 78], human–machine interaction [79, 80], and soft robotics [60, 81]. In such applications, a mechanical stimulation, which can take the form of an elongation, compression, bend or torsion, and can occur across different ranges of magnitudes, is effectively converted into an electrical signal. Several working mechanisms of signal generation have been proposed, typically based on controlled variations of resistance or capacitance [82]. In resistive sensors, a change in resistance of a conductor is induced by a change in geometry [57], such as the increase in length of the conductor due to an applied strain, or through the piezoresistive effect [64], where the intrinsic resistivity of the conductor is altered by the strain. In capacitive sensors, a change in capacitance between a pair of conductors separated by a dielectric is brought forth through changes in inter-conductor gap or surface area [83]. Regardless of mechanism, a capable soft electromechanical sensor must comprise the suitable materials and device architectures to be able to deform to large extents, be receptive towards the desired mode of stimulation, and exhibit a sensitivity tuned to the targeted loading intensity.

To achieve both mechanical deformability and electrical conductivity in a device material, researchers most often rely on nanocomposites. In these materials systems, conductive nanofillers, such as carbon nanotubes [84], graphene [85], carbon black [86], or metallic

nanowires [87, 88], are dispersed within an elastomeric matrix, such as polydimethylsiloxane (PDMS), forming a conductive pathway through a percolated network. Next to the material components, the device fabrication, with which conductive nanocomposites are coupled with standard elastomer dielectrics to realize the desired 3-dimensional device architectures, plays an important role. Proposed manufacturing approaches include nanomaterial deposition and coating-based techniques [89], molding [90], printing [91, 92] and wet spinning [93]. However, these techniques yield devices that are often limited in their size, structural complexity, and manufacturing throughput.

Nanocomposites based on thermoplastic elastomers rather than standard thermoset elastomers provide a unique opportunity in this regard, because this polymer class is compatible with polymer melt processing techniques, such as injection molding [94], compression molding [95], extrusion and melt-spinning [70, 96, 97], and 3D printing [98]. This family of techniques relies on the viscous flow of polymer melt under simultaneous application of heat and stress, and yields complex 3-dimensional products at high throughputs. The thermal drawing process, in particular, stands out because it enables the scalable manufacturing of fibers that integrate multiple materials arranged in fine cross-sectional architectures across extended lengths [15, 16, 99]. While this is an attractive prospect, in practice it is difficult to process thermoplastic elastomer-based nanocomposites in a molten state. This reduced processability is related to the percolated network of nanofillers that introduces a significant melt elasticity and yield behavior, which disrupts the controlled viscous flow of material [100]. Moreover, the manufacturing process heavily influences the conductivity of the nanocomposites [101], altering the performance of the resulting sensor device [96]. Because of these manufacturing obstacles, previously proposed soft sensors integrating thermoplastic elastomer-based nanocomposites have suffered from rudimentary device architectures and limited capabilities.

In this Chapter, we present a rheological assessment of nanocomposites as a method to screen materials for compatibility with the thermal drawing process. Based on this analysis, we purposefully engineer a nanocomposite consisting of carbon nanotubes dispersed in a thermoplastic elastomer matrix. By integrating the conductive nanocomposite into a dielectric cladding, we obtain fibers that are simultaneously mechanically stretchable and electrically conductive. Moreover, through an adaption of the thermal drawing process, we achieve stable drawing for an extended range of process temperatures, allowing the tailoring of the nanocomposite conductivity as well as strain-sensing sensitivity and range in the fibers. At a lower processing temperature, the sensitivity in resulting fibers is significant enough to capture strains below 1 %, while at elevated temperatures, we achieved a 15-fold increase in conductivity compared to the low-temperature-fiber and maintained conduction for stretching up to 160 %. Upon this materials and processing platform, we develop a diverse set of fiber-based mechanical sensors with complex cross-sectional structures and fabricated at large scale. We program the piezoresistive sensitivity of the nanocomposites through the fabrication process and integrate them in fiber architectures that are targeted at specific modes of stimulation. We demonstrate the high degree of design freedom and application potential through (i) a robotic fiber where an integrated bending mechanism is monitored by a piezoresistive feedback, (ii)

a pressure-sensing fiber based on geometrically induced variations of resistance, and (iii) a stretch-sensing fiber based on measures of capacitance.

3.2 Thermal drawing and rheological analysis of nanocomposites

To fabricate our mechanical sensors, we seek to employ the thermal drawing process. This technique involves the conversion of a macroscopic preform to a thin and long fiber through the controlled viscous flow of material under simultaneous application of heat and tension (Figure 3.1a). The preform itself is readily prepared using standard thermoplastic processing

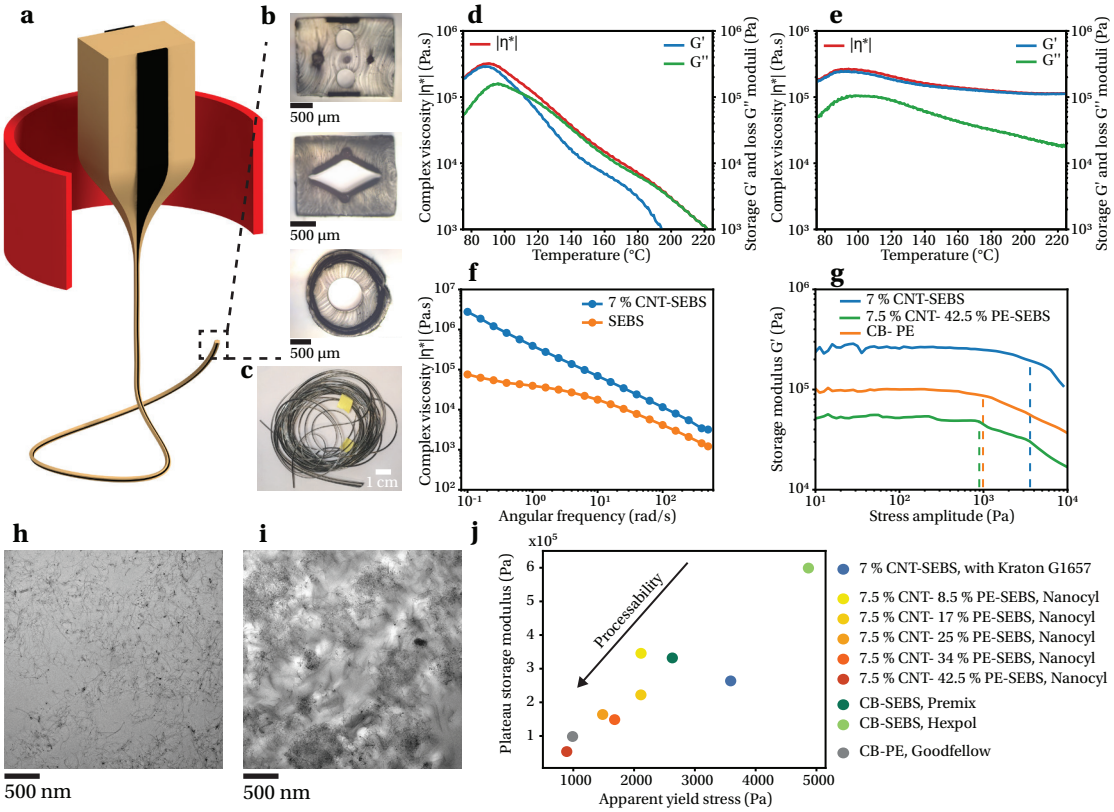

Figure 3.1 – Thermal drawing and rheological analysis of nanocomposites. a) Schematic of the thermal drawing process. b) Micrographs of various fabricated fiber cross-sections, integrating stretchable nanocomposites in an thermoplastic elastomer cladding. c) Photograph of a fabricated nanocomposite fiber. d) Oscillatory shear rheology temperature ramp of SEBS, showing the storage G' and loss G" moduli on one axis and the complex viscosity $|\eta^*|$ on the other. e) Temperature ramp of a nanocomposite with 7 wt. % CNT in SEBS. f) Frequency ramp of the nanocomposite and SEBS. g) Stress amplitude ramp of several nanocomposites. The onset of the curve marks the apparent yield stress, which is highlighted by a dashed line for each material. h) Transmission electron micrograph of 7 wt. % CNT in SEBS. i) Transmission electron micrograph of 7.5 wt. % CNT- 42.5 wt. % PE- SEBS. j) Materials selection map of several tested nanocomposites, quantified by the plateau elastic modulus and the apparent yield stress. The arrow indicates the region of highest processability of the nanocomposites by thermal drawing.

techniques, including the shaping of individual material parts by compression molding or mechanical machining, and the subsequent assembly of the parts and consolidation in a final compression molding step. During the thermal drawing process, the preform is essentially elongated to extreme extents, and thus the cross-sectional structure is preserved from preform to fiber, at typical uniform scale-down factors of 10 to 30 respective to the diameter. The advantage of the process is that complex multi-material structures with feature sizes on the order of micrometers are realized over 10s of meters of fiber length. We demonstrate this design freedom by fabricating several fibers integrating a stretchable nanocomposite in a thermoplastic elastomer cladding (Figure 3.1b, c), each envisioned as mechanical sensors for a specific mode of stimulation, as will be discussed later. However, as other thermoplastic fabrication techniques, thermal drawing is also restrictive in the materials that can be processed. Recently, it was found that compatible polymers exhibit a specific rheological profile in an oscillatory shear rheology experiment [9]. We show this behavior for the thermoplastic elastomer SEBS in Figure 3.1d. As the temperature is increased, the material transitions from a mainly elastic state where the storage modulus G' is significantly higher than the loss modulus G", to a viscous state where G" dominates. The crossover of G' and G" at 110 °C, which corresponds to the glass transition temperature of the hard polystyrene segment in the copolymer, delimitates the onset of the processing temperature window. Although both moduli decrease as the temperature is increased further, G" remains at an elevated level, resulting in a high viscosity value $|\eta^*|$ of 10^4 to 10^5 Pa.s in the processing window. Indeed, it is this pronounced viscosity that supports the stresses during the drawing process and retains the structural integrity of the fiber, which is impaired in low-viscosity materials by thermal reflow.

To impart electric conductivity to a material that is thermally drawable and mechanically deformable, we first introduce CNTs in the same grade of SEBS through melt mixing. By dilution of a masterbatch, we set the filler concentration to 7 wt. %, at which we find the material to be sufficiently conductive ($\rho = 0.1\,\Omega$.m). The resulting nanocomposite exhibits a rheological behavior that is dramatically different from the polymer base material (Figure 3.1e). Although the magnitude of the viscosity ranges on the same order of 10^5 Pa.s, it is dominated by its elastic rather than viscous component, underlining the importance of employing oscillatory rather than continuous rheology. In fact, no crossover of G' and G" is observed, and G' remains the larger of the two dimensions and is virtually unchanged by an increasing temperature. While this rheological behavior does exclude CNT–SEBS from being individually processed by thermal drawing, it can possibly still be co-drawn with a stress-supporting material that features a viscous nature counteracting the elasticity of the nanocomposite. Indeed, carbon black-reinforced polyethylene (CB-PE), a conductive but hard nanocomposite which exhibits a very similar rheological profile (Figure 3.2a), could be drawn within supporting claddings of polycarbonate [40] as well as SEBS [15]. However, drawing experiments of our nanocomposite CNT–SEBS supported by pure SEBS were unsuccessful, even at high cross-sectional ratios of SEBS (Figure 3.2b).

Because previous thermal drawing criteria are unsuitable, we need to establish a rheological assessment adapted to nanocomposites based on an understanding of the dynamic

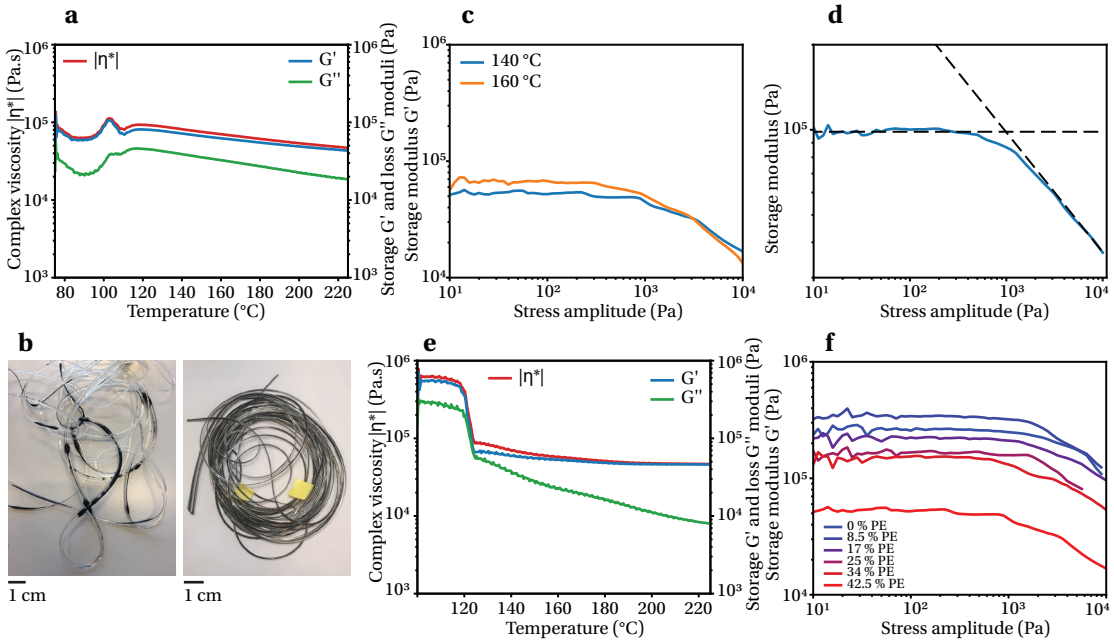

Figure 3.2 – Additional rheological analysis of nanocomposites. a) Oscillatory shear rheology ramp of the reference nanocomposite CB-PE. b) Photographs of drawn fibers with an SEBS cladding with 7 wt. % CNT- SEBS resulting in poor processability (left) and 7.5 wt. % CNT- 42.5 wt. % PE- SEBS yielding satisfactory drawing results (right). c) Stress amplitude sweep at different temperatures of 7.5 wt. % CNT- 42.5 wt. % PE- SEBS. d) Illustration of the apparent yield stress extraction from an stress amplitude sweep experiment for CB-PE. e) Temperature ramp of 7.5 wt. % CNT- 42.5 wt. % PE- SEBS. f) Stress amplitude sweep for nanocomposites with 7.5 wt. % in a blend of PE- SEBS with different amounts of PE.

microstructure. In composite systems with elevated filler concentrations, the filler–filler interactions result in the formation of a physical network, often termed rheological percolation, which restrains the long-range motion of polymer chains. This network structure significantly contributes to melt viscoelasticity, resulting in a change from a viscous fluid to solid-like behavior. This behavior is confirmed in a rheological frequency sweep, where the nanocomposite exhibits a linear behavior in the log-log scale at all frequencies, whereas the pure polymer enters a Newtonian region at low frequencies (Figure 3.1f). A linear behavior is usually accompanied by a high storage modulus and the appearance of a pronounced yield stress. Both of these characteristics are known to adversely affect the processability of melts, manifested for instance by a reduced maximum attainable melt draw ratio in melt spinning [102]. To investigate this effect, we seek to quantify the storage modulus and the yield stress of our nanocomposite through a stress amplitude sweep in oscillatory shear rheology (Figure 3.1g). We carry out this test at 140 °C, which is the approximate thermal drawing temperature of pure SEBS. Note that, in any case, beyond the softening point of the matrix, the temperature has a minor influence on rheological percolated nanocomposites (Figure 3.2b). In the test, after a plateau of G', the onset of decrease of the curve marks the apparent yield stress at which irreversible plastic deformation occurs. The details of the extraction of the apparent yield

stress are shown in Figure 3.2d. Indeed, we find a high plateau storage modulus of 330 kPa and yield stress of 3.5 kPa for CNT–SEBS, particularly compared to our reference material CB-PE with plateau storage modulus of 100 kPa and apparent yield stress 1 kPa. To explain this behavior, we employ transmission electron microscopy to image our nanocomposites (Figure 3.1h), because their elastic characteristics are highly dependent on the network morphology. We find CNTs to be in a highly dispersed state with little visible agglomeration, a configuration that indeed is known to contribute to a pronounced melt elasticity [103].

Guided by this characterization, we adapted our nanocomposite to a ternary system with 7.5 wt. % CNT, 42.5 wt. % PE and 50 wt. % SEBS, which we fabricated by diluting a CNT–PE masterbatch with SEBS. In this nanocomposite, we find the CNTs to be less dispersed and predominantly in the form of interconnected clusters (Figure 3.1i). This changed morphology is reflected in the rheological properties (Figure 3.1g), specifically by a reduced storage modulus and yield stress, and the successful drawing in an SEBS cladding (Figure 3.2b). In an analysis of the effect of PE content in the nanocomposite, we find a proportional reduction of elastic characteristics. A detailed rheological analysis of the different nanocomposite formulations is shown in Figure 3.2e, f. We summarize our findings in a materials selection map, with which nanocomposites compatible with thermal drawing can be identified through the key parameters of plateau storage modulus and apparent yield stress (Figure 3.1j). To underline the universality of the method, we also include several other materials systems which we trialed during our research. These encompass both different matrix materials, such as different grades of SEBS, as well as carbon black as an alternate nanofiller. Through thermal drawing tests of all the considered nanocomposites, we find that successful processing scales directly with lower storage modulus and apparent yield stress.

3.3 Mechanical and electrical properties of nanocomposite fibers

We address next the mechanical and electrical properties of the fabricated fibers, which are crucial for mechanical sensing applications. In our mechanical analysis, we focus on thermally drawn fibers which are composed of the nanocomposite 7.5 wt. % CNT- 42.5 wt. % PE- SEBS in an SEBS cladding. A supplementary characterization of the individual materials is detailed in Figure 3.4. In static tensile tests of the fibers (Figure 3.3a), we measure a 100 %-modulus of approximately 2 MPa and an elongation at break of 980 %. At the terminal elongation, both material components of the bi-component fibers fail simultaneously, indicating a strong interfacial bonding. We also submitted the fibers to dynamic tensile tests, where the strain was varied between 0 % and 100 % for 10 cycles (Figure 3.3b). The materials' response was predominantly elastic, where the fibers return to their initial configurations as the load is removed. However, a hysteresis and strain softening behavior is recorded, which is often observed for elastomeric systems and is related to the viscoelastic nature of the materials. We quantify the stretchability of the fibers by a remnant elongation when the load returns to zero after 100 %-stretching cycles, which was found to be 10 % after 1 cycle. In subsequent cycles, only minor changes of the hysteresis curve are observed. Thus, in applications, a

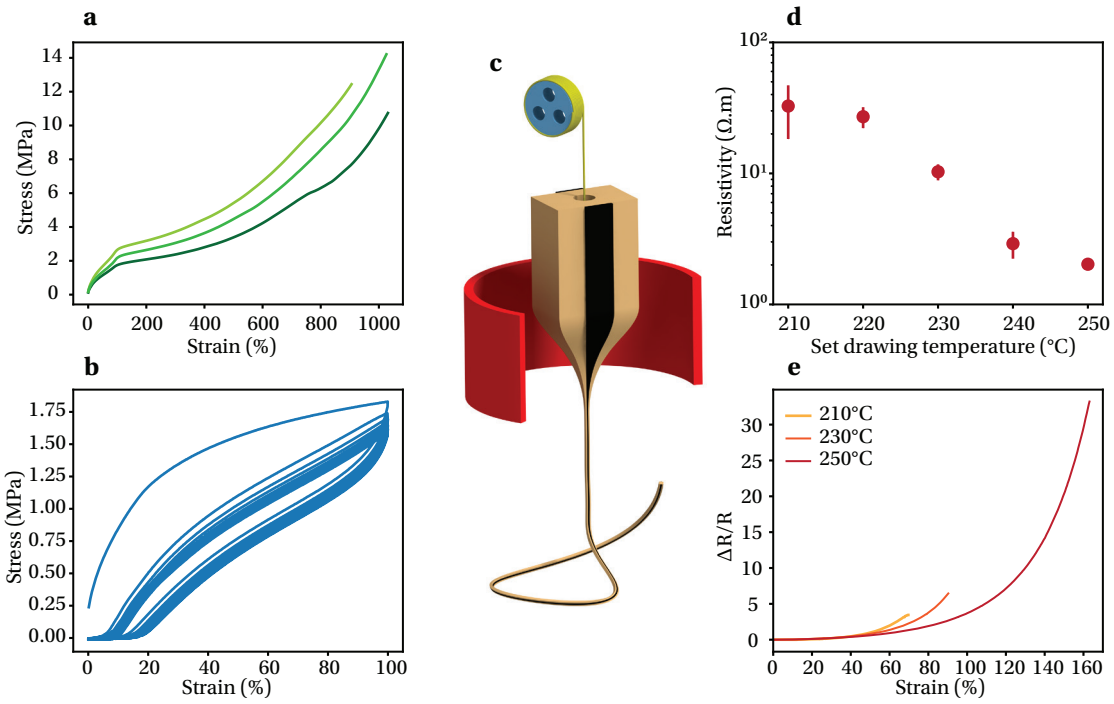

Figure 3.3 – Mechanical and electrical characterization of nanocomposite fibers. a) Tensile test results of several samples of fibers constituted of the nanocomposite embedded in SEBS. b) Dynamic tensile test results of a nanocomposite fiber stretched in the range of 0 % to 100 % for 10 cycles. c) Schematic of the thermal drawing process extended by the integration of a draw-stabilizing spine that is integrated in the fiber by feeding. d) Resistivity of the nanocomposite in fibers drawn at different set machine temperatures. e) Relative resistance change of nanocomposite fibers stretched up to the point of lost conductance.

pre-stretching can be introduced to assure that the fiber remains entirely elastic and taut within the targeted strain range. As a conclusion of the mechanical analysis, we find that the softness and elastic stretchability qualifies the nanocomposite fibers for applications in soft electronics and wearable devices.

We investigate the electrical properties by measuring the resistivity of the nanocomposite in the fibers. While the nanocomposite is indeed conductive, we find the resistivity to increase to 30 Ω.m from the pre-drawing state at 0.1 Ω.m. This effect is caused by the restructuring of the conductive filler network under the severe deformation of the thermal drawing process [11, 101]. It is known to be sensitively dependent on the processing conditions, most importantly the temperature, because the temperature alters significantly the viscosity of the polymer and thus the shear forces acting on the filler aggregates [104]. However, for thermal drawing, the processing temperature window is narrow, because the reduced viscosity of the fiber materials under increased temperature can lead to uncontrolled flow and fiber breakage. Thus, to extend the processing temperature range, we adapt the thermal drawing process and introduce a rigid spine as a flow-controlling element (Figure 3.3c). The spine is an inert 1-dimensional element, of diameter 50 µm to 250 µm and in the form of a metal wire or polymer line, that is

introduced into a dedicated channel in the preform before the process start. As the materials of the preform begin to flow into the fiber, the channel narrows, capturing the spine and unspooling it continuously as the fiber is drawn. Note that the spine can additionally play a functional role in the produced fiber, such as electrical or optical guiding, or be removed in post-processing, as will be shown later.

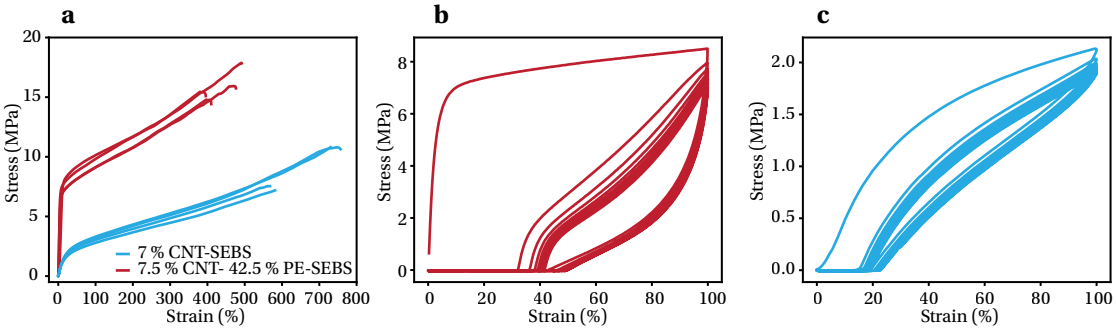

Figure 3.4 – Mechanical analysis of the nanocomposites. a) Tensile test results of several samples of two different nanocomposites. b) Dynamic tensile test results of a 7.5 wt. % CNT- 42.5 wt. % PE- SEBS film stretched in the range of 0 % to 100 % for 10 cycles. c) Dynamic tensile test results of a 7 wt. % CNT-SEBS film stretched in the range of 0 % to 100 % for 10 cycles.

The process extension allows us to increase the upper temperature limit of the process for SEBS-based fibers by 40 °C, resulting in a drawing range of 210°C to 250 °C. Note that these temperatures represent the set machine temperatures, which do correspond but are not equal to the true temperatures experienced by the material. By drawing nanocomposite fibers at different temperatures, we record a strong variation in resistivity (Figure 3.3d). At the highest processing temperature, we achieve a resistivity of 2 Ω.m, which is lower by a factor of 15 compared to the low-temperature value. Thus, through the processing temperature alone, we can effectively tune the resistivity. Moreover, the piezoresistivity of nanocomposites is closely linked to the initial resistivity, because the electrical properties are most sensitively affected by deformations close to the electrical percolation threshold [105]. Indeed, we find the relative resistance of nanocomposite fibers to significantly increase at lower elongations for fibers drawn at lower temperatures (Figure 3.3e). Along with the ability to realize complex multi-material structures in long fibers, the tunable electrical properties of the integrated nanocomposites promote the thermal drawing process to a versatile platform for the fabrication of sensors targeted at specific modes and ranges of mechanical stimulation.

3.4 Piezoresistive bending feedback in robotic fibers

In our first device example, we employ our nanocomposite to monitor the extent of fiber bending induced by an integrated actuation mechanism. The rectangular cross-section of the robotic fiber, which integrates nanocomposite sheets, lumens, an optical guide and a metallic wire in an SEBS cladding, is shown in Figure 3.5a. The fiber bending mechanism is driven by tendons, which take the form of nylon lines of diameter 200 µm introduced in the two lumens.

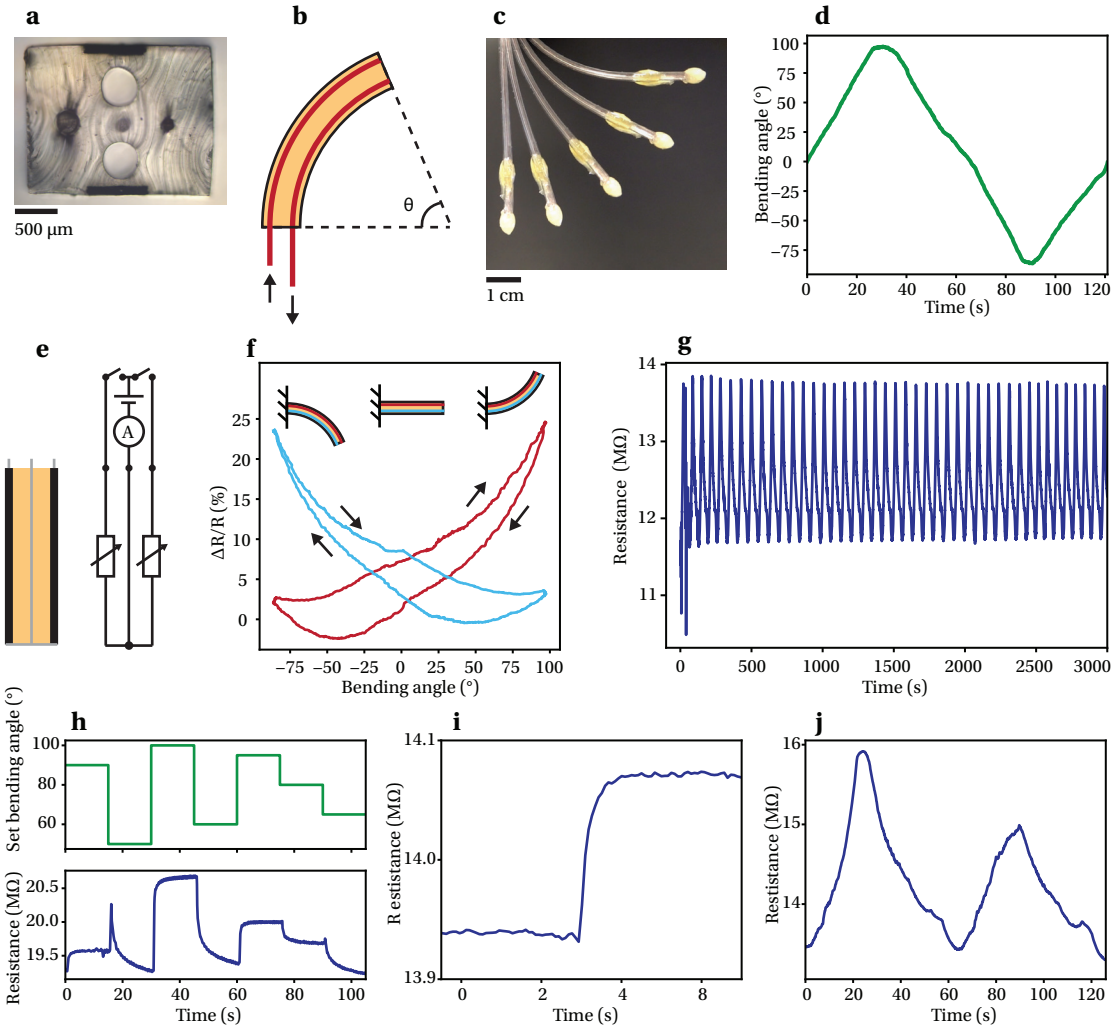

Figure 3.5 – Piezoresistive bending feedback in robotic fibers. a) Micrograph of fiber cross-section, integrating two sheets of nanocomposite, two lumens, a metallic wire, and a light guide. b) Schematic of the tendon-driven bending mechanism in the fibers, quantified by the bending angle θ. c) Sequence of stacked photographs of the robotic fiber at increasing bending angles. d) Bending angle ramp of a robotic fiber captured by computer vision. e) Schematic of the conductive elements in the bending fiber, showing the nanocomposite sheets and the center metallic wire, and the equivalent circuit. f) Resistive response of the two nanocomposite sheets during a bending angle ramp. The schematics show which sheet is in compression and which in tension. g) Resistive response of a robotic fiber during cyclical bending. h) Set bending angle and resistive response during a random angle sequence. i) Resistive response for a small bending angle step of 5°. j) Resistive response for a robotic fiber bending without and obstruction (first peak) and for the same commands but the path being blocked by an obstacle, thus impeding further bending (second peak).

By fixing the tendons at the distal end and concertedly pulling on them at the proximal end, the fiber bends to controlled amounts quantified by the bending angle (Figure 3.5b). We tested this actuation mechanism by applying a bending angle ramp from 0° to 90° and back for both bending directions and tracking the movement with computer vision (Figure 3.5c, d).

As shown, the configuration of the fiber can be controlled with the integrated tendons. The actuation mechanism is detailed further in Chapter 5.

Next, we aim at generating a feedback signal with the integrated nanocomposites to enhance the controls of the robotic fiber, because configurations of soft robotic systems are often difficult to predict based on input alone, particularly in dynamic environments where obstacles can be encountered. However, with a cross-sectional height of 1.7 mm, the strains induced by the bend in the thin fiber scale below 1.3 % for the targeted bending angle range of 0° to 90° and a fiber length of 100 mm. To capture such low levels of strains, we draw the fibers at the lowest processing temperature, which results in the highest resistivity and piezoresistivity of the incorporated nanocomposites. Moreover, we position the nanocomposite sheets on the outer faces of the fibers because the highest bending-induced strains are experienced at the position furthest from the neutral plane. To interrogate the two nanocomposite sheets selectively at the proximal end, we connect the two sheets at the distal end to the embedded metallic wire, which acts as a grounding element (Figure 3.5e).

The resistive responses of the nanocomposites are shown in Figure 3.5f for a complete cycle of bending of -90° to 90°, where the sign of the bending angle indicates the bending direction. For a given bending angle, one of the nanocomposite sheets is in tension while the opposing one is in compression. As shown, in compression, the resistance increases significantly up to a relative change of 25 %, whereas, in tension, only a small non-monotonic response is recorded. Since the observed increase of resistance in compression is opposite to the expected decrease due to the change in geometry, the resistive response must be dominated by the piezoresistive effect. In nanocomposites, the piezoresistivity results from the destruction and formation of conductive pathways and is highly dependent in trend direction and magnitude on the morphology of the percolated nanofiller network [106]. Practically, the disparate resistance variations in compression and tension enable the identification of bending direction, and the pronounced response in compression allows the estimation of bending angle magnitude. However, the bending sensor performance is limited by a hysteresis effect, which is, analogous to the mechanical properties, attributed to the viscoelastic nature of the polymer as well as the partly irreversible restructuring of the filler network during deformation. We characterized the sensor further by inducing cyclical bending with the robotic fibers in the defined range of -90° to 90° and simultaneously recording the resistive response of the nanocomposite (Figure 3.5g). After the initial cycle, the signal variation stabilizes and only a small drift is observed, underlining the reversibility and durability of the proposed sensor. To investigate the effect of deformation history we also induced a sequence of random bending angles (Figure 3.5h). As shown in the temporal plot, the resistive response follows generally the induced bending angle, but some variations are caused by the deformation history. Due to the dependence of the resistive response not only on absolute bending angle but also on the deformation history, the proposed bending sensing scheme is only suitable for approximate configuration predictions. Nonetheless, the proposed sensor is capable of detecting angle variations as small as 5°, which is shown by the distinct resistive response to the small bending angle step (Figure 3.5i). Moreover, the sensor can detect obstacles on the robotic fiber trajectory. We illustrate

this behavior by comparing the resistance variation through bending for an unhindered and an obstructed bending path (Figure 3.5j).

The results suggest that the soft robotic fibers with piezoresistive nanocomposite feedback are promising in applications that necessitate a long and thin device in unpredictable environments, such as medical interventions with active catheters and endoscopes.

3.5 Resistive pressure-sensing fibers

In a second device application, we target the sensing of compressive loads, which are applied transversally on the fibers. In the proposed cross-sectional architecture (Figure 3.6a), sheets of nanocomposites are placed on opposing faces of a diamond-shaped empty channel in an SEBS cladding. Additionally, Cu wires of diameter 125 μm are embedded within the nanocomposite sheets at opposing corners of the channel. In the initial configuration without load, the two electrodes, each composed of a metallic wire and nanocomposite sheet, are separated by an air gap, and thus no current can flow. As a pressure is applied on a section of the fiber, the elastic structure deforms, bringing the two nanocomposite sheets in contact and allowing a current to flow. The equivalent circuit formed under an area load is schematized in Figure 3.6b. As the resistance of the wires can be neglected, the measured resistive load in the equivalent circuit depends only on the nanocomposite elements and can be expressed as:

$$R_m = \frac{1}{2} \cdot \rho \cdot \frac{l}{t \cdot w} \tag{3.1}$$

where ρ is the resistivity, l the length of the current pathway in the fiber cross-section, t the sheet thickness and w the width of the contact area. The factor $1/2$ originates from the two equal pathways the current can take through the nanocomposite sheets to travel from one wire to the other. As the compressive load is increased, the current travels a shorter distance and thus l decreases. The width w, however, is proportional to the size of the loaded area, i.e. the length of the loaded fiber segment. Thus, the measured resistance is varied based on load intensity and area at a sensitivity that is equal to the ratio of nanocomposite resistivity and sheet thickness. Note that in this scheme, unlike similar previously reported fiber-based pressure-sensing strategies [15, 19], the measurement does not depend on the load's position on the fiber, because the negligible resistance of the metallic wires results in an equipotential behavior along the fiber length.

To obtain a high measurement sensitivity, we thermally draw our pressure-sensing fibers at the lower temperature limit of the processing window, resulting in high nanocomposite resistivity. We test the effect of load intensity, by applying a pressure ramp at constant loaded area and simultaneously monitoring the conductance, which is the inverse of resistance (Figure 3.6c). As expected, at small loads, the electrodes are separated, and the conductance is zero. However, at a threshold pressure of 150 kPa, the conductance starts to increase, corresponding to the point of first contact. Subsequently, the conductance scales near linearly with the load intensity, up

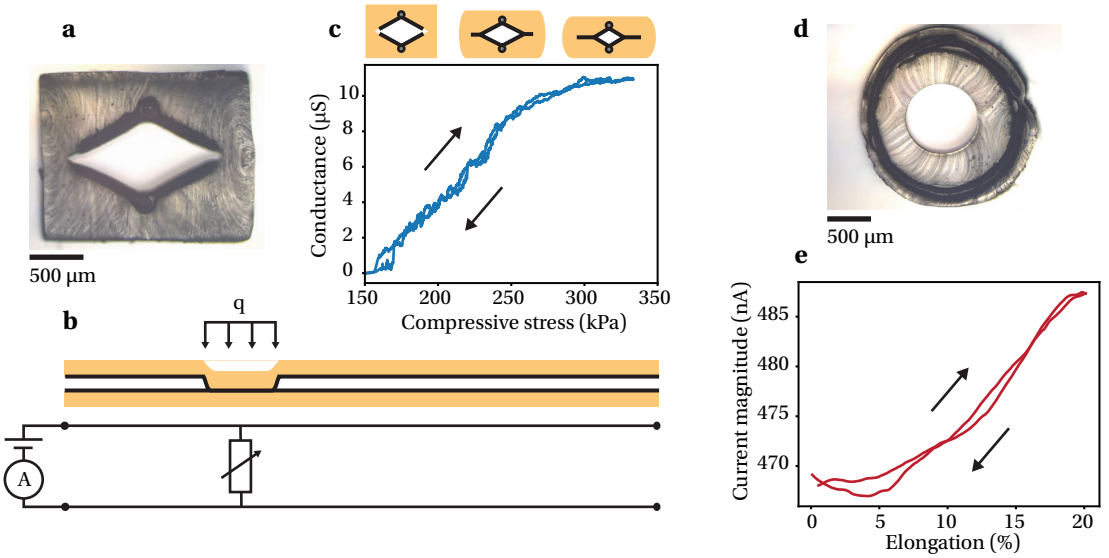

Figure 3.6 – Pressure-sensing and stretch-sensing fibers. a) Micrograph of a pressure-sensing fiber cross-section. Two sheets of nanocomposites with embedded metallic wires are arranged on opposing faces of a diamond-shaped empty channel. b) Schematic of a fiber being compressed by an area load q and resulting equivalent circuit. c) Resistive response of the pressure-sensing fiber under a compressive load ramp. The structural deformation is indicated by a sequence of schemes. d) Micrograph of stretch-sensing fiber cross-section, showing two concentric nanocomposite sheets separated by a thin dielectric film. The center hole is the result of the draw-supporting spine that was removed in post-processing. e) Electric response of an increasing elongation being applied to the capacitive fiber.

to point where the signal saturates, which corresponds to the deformed configuration where the channel is fully closed, and the current pathway cannot be decreased further. In this case, we observe a negligible hysteresis effect, because the structural deformation is fully reversible. Based on the results, we extract an expected pressure-sensing accuracy of approximately 10 kPa in the range of 150 kPa to 300 kPa. Note that both accuracy and range can be tuned by altering the cross-sectional geometry, for instance through the slope of the diamond shape. We attribute the observed behavior predominantly to the geometric effect of the structural deformation detailed above, rather than a piezoresistive effect due to the deformation of the nanocomposite itself.

3.6 Capacitive stretch-sensing fibers

For our final example, we enable stretch-sensing with nanocomposite fibers based on a capacitive mechanism. The fibers integrate a rolled-up stack of two nanocomposite sheets and two SEBS sheets that are alternately arranged, resulting in a structure resembling an axial lead capacitor (Figure 3.6d). In a theoretical consideration, when the fiber is elongated, the electrode length increases while the electrode width and dielectric spacing decrease to a smaller extent dictated by the Poisson number, resulting in a net increase of capacitance as a function of axial strain.

For this capacitive scheme, a low resistivity and piezoresistivity of the nanocomposite is sought, which is achieved through a high processing temperature of 250 °C. We introduce a polytetrafluoroethylene (PTFE) tube of diameter 760 µm as a draw-supporting spine, which is mechanically removed in post-processing. We investigate the performance of the capacitive fibers as stretch sensors by measuring the current magnitude at a frequency of 1 kHz as a function of axial strain (Figure 3.6e). Indeed, the current increases, indicating an increase of capacitance.

3.7 Conclusion

We have assessed the compatibility of thermoplastic elastomer-based nanocomposites with the thermal drawing process. The microstructure of the nanocomposites, specifically the state of dispersion of the nanofillers, sensitively influences the rheological properties, such as the melt viscoelasticity and a plastic yielding behavior. However, processable materials could be identified by the key parameters of plateau storage modulus and apparent yield stress in a stress amplitude ramp experiment in oscillatory rheology. Embedded in a thermoplastic elastomer cladding, the resulting nanocomposite fibers are found to be soft and stretchable (100 %-modulus 2 MPa, elongation at break 980 %), as well as electrically conductive, a property that can be tuned by the processing temperature when the fiber incorporates a process-supporting spine ($\rho = 2\,\Omega$.m to 30 Ω.m). Along with the intricate multi-material cross-sectional designs, the programmable resistivity and linked piezoresistivity make the thermally drawn nanocomposite fibers a versatile platform for mechanical sensors, which can be manufactured at extreme aspect ratios and large scale. We demonstrated this potential with three fiber-based devices, which are each targeted at a specific mode of mechanical stimulation and rely on a different sensing scheme. Specifically, we developed a soft robotic fiber with an integrated bending mechanism that is monitored with a piezoresistive feedback signal; a resistive pressure-sensing fiber that detects variations in load intensity and area through controlled structural deformations; and finally, a stretch-sensing fiber where elongations induce reversible changes in capacitance. We expect that the proposed materials and processing platform as well as the resulting sensing concepts will significantly advance soft robotics and wearable devices.

3.8 Experimental section

Nanocomposites preparation

All the nanocomposites were obtained as masterbatches and some were diluted to the desired filler concentration using a twin-screw microcompounder (Xplore) at 240 °C, 200 rotations per minute, and for 3 minutes. The nanocomposites are subsequently shaped using compression molding (UVL 5.0, Lauffer Pressen) at 240 °C and 1 bar for 40 minutes.

Rheological analysis

The rheological properties of the materials were assessed with a rheometer (AR 2000, TA Instruments) in a parallel plate configuration using disk samples of thickness 1 mm and diameter 25 mm. The temperature ramps were conducted from 50 °C to 250 °C at a ramp speed of 3 °C.min^{-1}, a strain amplitude of 1 %, and an angular frequency of 1 rad.s^{-1}. The frequency sweeps were performed from 10^{-1} rad.s^{-1} to 10^{3} rad.s^{-1} at a temperature of 140 °C and a strain amplitude of 0.1 %. In the dynamic oscillation stress sweeps, the stress amplitude was increased from 1 Pa to 10^{4} Pa at a temperature of 140 °C (unless specified otherwise) at an angular frequency of 1 rad.s^{-1}. The apparent yield stress is defined as the onset value of the storage modulus curve.

Fiber fabrication

Individual components of the preforms were shaped from granular polymers by compression molding. Nanocomposite sheets and pure polymer parts (SEBS G1657, Kraton) were assembled and consolidated in a final compression molding step at 0.1 bar and 120 °C for 30 minutes. Subsequently, the preform was thermally drawn into a fiber using a custom draw tower. Additional 1-dimensional elements, including metallic wires (tin coated copper wires, McMaster), optical guides (optical grade plastic optical fiber unjacketed, Edmund Optics), nylon lines (clear nylon lines, McMaster), and Teflon tubing (high-temperature tube sleeving, McMaster), are introduced using the feeding extension of the thermal drawing process. For electrical contacting, the selected conductor at the fiber end was exposed mechanically and the contact established using silver paint for the nanacomposite and solder for integrated metallic wires.

Microstructural, mechanical, and electrical analysis

Fiber cross-section were imaged using optical microscopy (DM 2700 M, Leica). Samples for transmission electron microscopy were cut with a ultra-cryomicrotome, transferred to a carbon/copper grid supports and imaged by a transmission electron microscope (F200X, Talos) at 200 kV. The mechanical properties of the nanocomposites and the fabricated fibers were assessed by uniaxial tensile testing (Z005 stand with 50 N load cell, Zwick/Roell) at an extension speed of 120 mm.min^{-1}. The electrical resistivity was assessed by an electrometer (Sourcemeter 2400, Keithley) at a source current of 100 nA.

Electromechanical analysis of fiber devices

For the bend-sensing fibers, fiber samples of length 10 cm long were cut. A the proximal fiber end, the composite electrodes from both fiber sides as well as the embedded metallic wire were contacted selectively. At the distal end, the two composite electrodes and the metallic wire were short-circuited with silver paint. Nylon lines were inserted into the appropriate

channels and mechanically fixed at the distal end, thus acting as tendons. They were used to actuate the fiber with the help of a custom setup involving two servo motors and a microcontroller, enabling a precise control of the fiber bending angle. During the test, the resistance was continuously monitored using the electrometer and the bending angled using a camera (C270, Logitech) and computer vision tracking (OpenCV in Python). For the pressure-sensing fibers, fiber samples of length 10 cm were employed. The fibers were submitted to controlled compressive force ramps using a dynamic mechanical analysis instrument (DMA Q800, TA Instruments) in compression mode with two parallel plates at a ramp speed of 6 $N.min^{-1}$. The resistance between the two embedded metallic wires, contacted at one fiber end, was measured continuously during the test using the electrometer. For the stretch-sensing fiber, fibers of length 10 cm were prepared, and stretched to controlled extents by a tensile testing stand (Multitest 2.5 kN, Mecmesin). Simultaneously, the capacitance between the two composite electrodes, contacted at one fiber end, was recorded using an impedance analyzer (HF2LI lock-in amplifier, Zurich Instruments) at a voltage amplitude of 1 V and a frequency of 1 kHz.

4 Soft transmission lines as distributed probes of multimodal deformations

Having relied on polymer composites in the fiber-based sensor presented so far, we consider liquid metal as a conductors in this Chapter. While the fluid nature of this material constrains the fiber design, its comparatively high conductivity enables more involved techniques of sensor interrogation. In this Chapter, we focus on the study of the propagation of high-frequency electrical signals in the fibers, which evokes unprecedented functionality, such as the capturing of multimodal deformations and the decoupling of multiple stimuli. Parts of the presented work are also published elsewhere [16].

4.1 Motivation

Electronic skins and textiles are an emerging technology for applications in health monitoring [51, 64, 88, 107], human–machine interactions [59, 80], safety engineering [108, 109], and soft robotics [60, 69, 110]. An essential functionality in these flexible and often stretchable systems is the detection of mechanical stimulation such as compression, elongation, bending, and torsion. However, quantifying and spatially resolving deformations of variable nature and number is a significant design challenge. Strategies usually involve grids of point sensors on a flexible substrate, but point sensors are limited in the kind of deformation they can sense, and they must all be selectively addressed [61, 63]. Alternatively, the number of contacts, which are failure-susceptible in flexible and stretchable substrates, can be drastically reduced and positioned outside the sensing area by employing networks of functional fabrics [62, 79], yarns [111], or fibers [15, 19, 68, 112], which act as distributed sensors. The scalability of fabrication processes such as extrusion [67, 113] or thermal drawing [6, 114] make fiber-based systems particularly attractive in applications where large and flexible surfaces need to be functionalized. However, while fiber technology is often more receptive towards multimodal stimulation, only a single physical dimension, such as electrical resistance [15] or optical intensity [67, 69], is typically monitored in a fiber-based sensor. This hinders the decoupling of different types of deformation and the assessment of the spatial position of multiple stimuli. Thus, a practical strategy for multimodal mechanical sensing over large and soft areas has yet to be developed.

Electrical time-domain reflectometry — a time-of-flight technique in which high-frequency pulses are sent down impedance-controlled transmission lines and are reflected at discontinuities — provides both the nature and position of applied stimuli [115], making it a promising approach for the interrogation of distributed sensors. The technique is primarily employed for spatially resolved monitoring of structural health [116, 117], landslides [118], and dielectric characteristics of surrounding media [119, 120]. Reflectometry probes have also been proposed as mechanical sensors, but the use of traditional hard conductors severely limits their sensitivities and deformation ranges [121, 122]. Developments in structural configurations [123, 124] and materials [125, 126] lead to a new generation of transmission lines for stretchable electronics. However, performing time-domain reflectometry using entirely soft materials remains a challenge, because the strict design principles of transmission lines constrain the engineering of material, structure, and process.

In this Chapter, we show that transmission lines can be adapted to the field of soft and stretchable electronics, and report several designs that integrate —in a scalable and precise way —liquid metal conductors in an elastomeric dielectric. We demonstrate that thermal drawing can be used to fabricate transmission lines in large lengths and with uniform, targeted, and complex cross-sectional architectures. Through targeted structural changes, we tune the radio-frequency characteristics in the soft transmission lines, including impedance, shielding, and losses. We also investigate experimentally and theoretically reflected waves in the time-domain triggered by multimodal deformations of the dynamically responsive liquid metal conductors themselves, as opposed to only the dielectric between them. This mechanism enables multiplexed pressure measurements at a sensitivity that is improved by a factor of 200 when compared to transmission lines based on conventional hard metals. Additionally, the soft transmission lines allow spatially resolved stretch sensing. Using a one metre-long line acting as a distributed probe, we demonstrate the quantitative assessment of multiple pressure points with a force resolution of 0.2 N and a spatial resolution of <6 cm, as well as an elongation with a strain resolution of 0.25 %. By integrating a soft transmission line in a large stretchable fabric (50 cm x 50 cm), interfaced through a single contact point to cost-effective and easily available electrical instrumentation, we create an electronic textile with higher functionality than existing systems that require hundreds of point sensors and electrical connections.

4.2 Soft transmission line design and fabrication

The soft transmission lines are composed of liquid metal alloy microchannels (68.5% Ga, 21.5% In, 10% Sn by weight) arranged within a thermoplastic elastomer dielectric (poly[styrene-b-(ethylene-co-butylene)-b-styrene], SEBS). The transmission lines are fabricated by thermal drawing (Figure 4.1a). The liquid metal is injected into the polymer structure at the level of the preform for smaller diameter channels, where it takes a passive role during processing, or directly into the fibers for sufficiently large channels. The rheological analysis of SEBS (Figure 1.3) allows the estimation of a temperature operating range, which is delimitated by

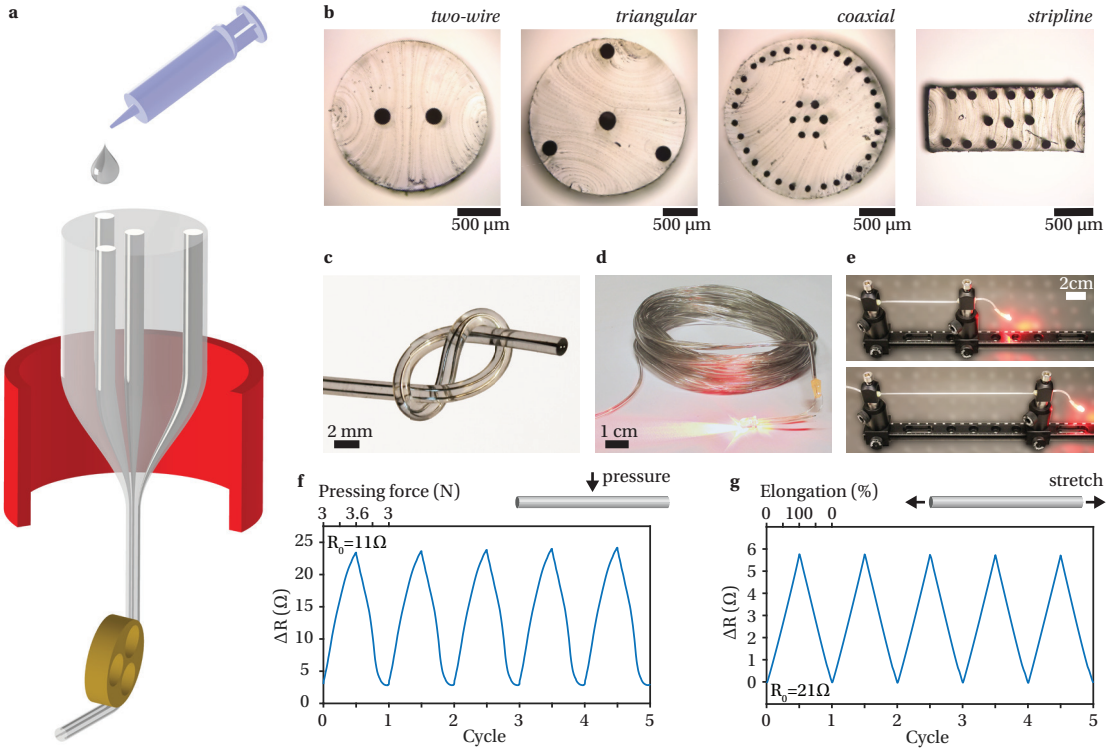

Figure 4.1 – Fabrication and structure of soft transmission lines. a) Schematic of the thermal drawing technique employed to process liquid metal–thermoplastic elastomer constructs into long fibers acting as transmission lines. b) Optical micrographs of line cross-sections as examples of commonly employed designs with targeted radio frequency characteristics, realized in soft constructs through the prescribed arrangement of Ga-In-Sn channels in SEBS. c) Photograph of a soft transmission line with two liquid metal conductors that run uniformly along its length. d) Photograph of a roll of transmission line connected to a power source on one end and an LED on the other end, demonstrating electrical conductivity through several insulated channels over extended lengths. e) Photographs of a line being stretched to 100% elongation with consistent conductivity, as shown by the unchanged brightness of the LED powered through the strained fiber. Change in resistance of a f) laterally compressed and g) longitudinally stretched line over several cycles.

the crossover of storage and loss modulus, yielding a maximum operating temperature of 114 °C. This corresponds to reports of the glass transition temperature of the crosslinking polystyrene blocks in the employed SEBS grade, which was found to be 120 °C [127].

The thermal drawing technique enables the accurate and length-consistent placement of the liquid conductors in the dielectric, which is of outmost importance for efficient radio frequency transmission, as small deviations in size or spacing can sensitively influence operational parameters such as propagation constant and characteristic impedance. To demonstrate the high level of control over material and process, we recreated transmission line designs common in the domain of hard materials through the arrangement of cylindrical microchannels in the elastic fibers, including two-wire, triangular, coaxial, and stripline (Figure 4.1b). Notably, these complex structures can be realized over extended lengths of soft fiber (Figure 4.1c), in which channels remain individually conductive but insulated from one another along

the entire length, as illustrated by connecting the two poles of an LED through a long fiber (Figure 4.1d). We demonstrate maintained conductivity under large, reversible deformations qualitatively by stretching a fiber, connected once more to an LED, to 100 % strain (Figure 4.1e). We also assessed quantitatively the fiber's direct current resistance change during deformation by pressing and stretching (Figure 4.1f, g, respectively). These well-known behaviors in liquid-metal based systems [128–132] have proven beneficial for sensing applications, yet do not allow to discriminate between different deformations, or localize them in the system. Such sensitive and reversible changes of impedance can however be exploited, with the right coaxial design, for reflectometry-based sensing.

4.3 Time-domain reflectometry in soft transmission lines

We now turn to treating the microstructured fibres as transmission lines and interrogate them with electrical time-domain reflectometry. The experimental setup is schematized in Figure 4.2a. A sharp step function, in our case with an amplitude of 0.5 V and a risetime of 100 ps, is produced by a pulse generator and coupled into the line. The resulting voltage transient across the line end is monitored with an oscilloscope connected in parallel.

Before introducing and characterizing line discontinuities, which cause partial reflections of the propagating signal, we assessed waveforms generated for soft transmission lines of different lengths (Figure 4.2b). The produced signals are characteristic for open circuit-terminated lines; specifically, an abrupt initial rise as the step is first incident on the line, a near-constant voltage for the time of signal propagation through the line, and finally a full reflection at the end of the line. The characteristic impedance can be directly deduced from a time-domain reflectometry measurement. The decisive feature of the waveform is the voltage amplitude across the transmission line at a time where the input signal has risen to its full level, but no reflected waves have reached the interrogated end. The characteristic impedance Z_0 is calculated based on the measured voltage U as well as the generator's input voltage U_g and internal resistance R_g [133]:

$$Z_0 = R_g \frac{1}{\left(\frac{U_g}{U} - 1\right)} \tag{4.1}$$

When plugging in the values obtained for the measurement of a standard coaxial cable (Figure 4.3a), specifically $U_g = 0.50$ V, $R_g = 50\,\Omega$, and $U = 0.25$ V, we do indeed find the expected characteristic impedance of 50 Ω. Transmission lines with custom connectors are more difficult to evaluate, because the contact resistance of the line connector offsets the voltage level. For the waveforms obtained for soft transmission lines displayed in Figure 4.2b, we find $U = 0.32 \pm 0.01$ V, yielding a characteristic impedance of $89 \pm 6\,\Omega$.

The travel time of the signal to the line end and back is proportional to the line length (Figure 4.2b inset) and the propagation speed is found to be $1.95 \cdot 10^8\,\mathrm{m.s^{-1}}$. This value depends only on the relative permittivity of the dielectric medium [134], calculated here to be 2.38, which is

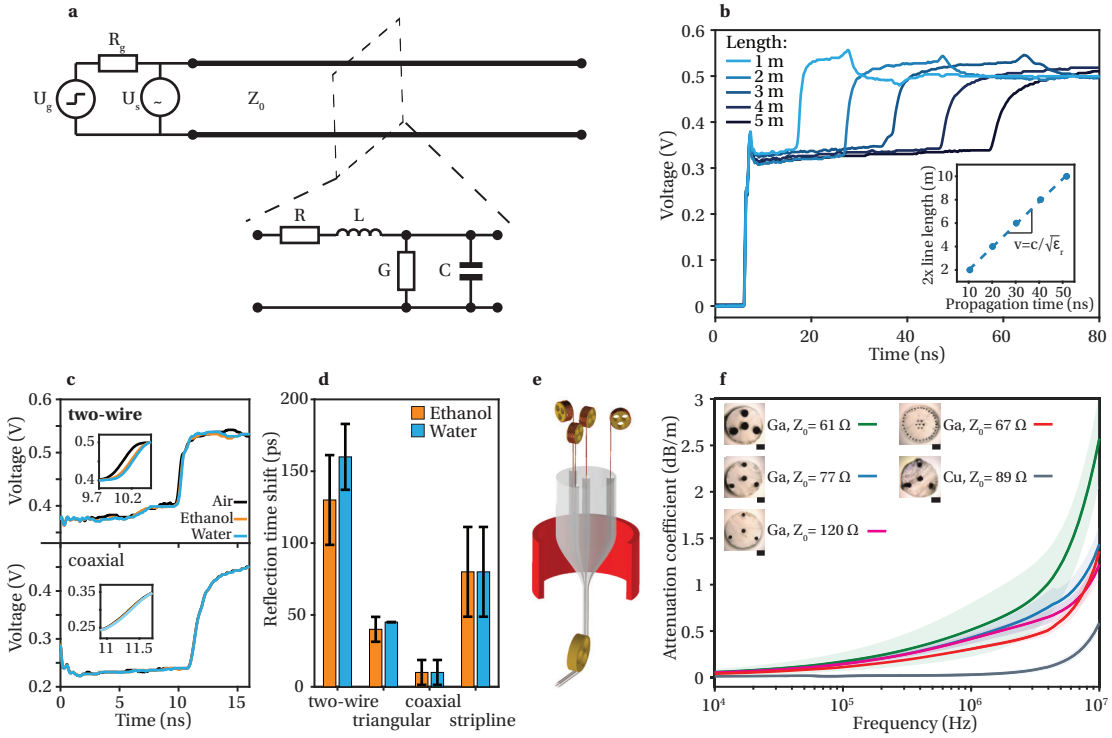

Figure 4.2 – Time-domain reflectometry setup and evaluation of transmission line performance. a) Circuit diagram of the reflectometry setup. A function generator with internal resistance R_g produces a step pulse with amplitude U_g that is applied to the interrogated transmission line with characteristic impedance Z_0 and open-circuit termination. The voltage transient across the transmission line is monitored by an oscilloscope connected in parallel. In transmission line theory, an infinitesimal piece of line can be modelled as a lumped-element circuit with per-unit-length resistance R, inductance L, conductance G, and capacitance C. b) Time-domain reflectometry waveforms observed for liquid metal triangular transmission lines of increasing lengths. The inset shows twice the line length as a function of propagation time of the signal from line end to end and back. The slope of the resulting linear function corresponds to the propagation speed v, which can be approximated with only the speed of light in vacuum c and the relative permittivity of SEBS ϵ_r. c) Waveforms of two-wire and coaxial lines before and after a section is submersed in ethanol and water. The initial signal rise and connector ringing are cut for clarity. The insets show an enlarged plot of the reflection at the open circuit termination, underlining the time delay induced by the medium for the two-wire line opposed to the unaffected coaxial line. d) Delay time induced by section-wise submersion of lines in ethanol and water for different transmission line types. e) Schematic of thermal drawing with solid wires continuously fed into the created fiber during processing. f) Frequency-dependent attenuation coefficient of transmission lines with different conductor materials (liquid metal Ga, solid copper Cu), structure type (triangular, coaxial), and characteristic impedance (Z_0). The solid lines represent the mean and the shaded areas the standard deviation.

consistent with the literature [135]. With the knowledge of the propagation speed, the time axis can be directly converted into distance units, enabling intuitive localization capability.

To evaluate the performance of fabricated transmission lines, we first test the shield quality for different structures by immersing line sections in ethanol and water with relative permittivities of 25 and 80 [136], respectively. A comparison of the waveforms obtained for two disparate

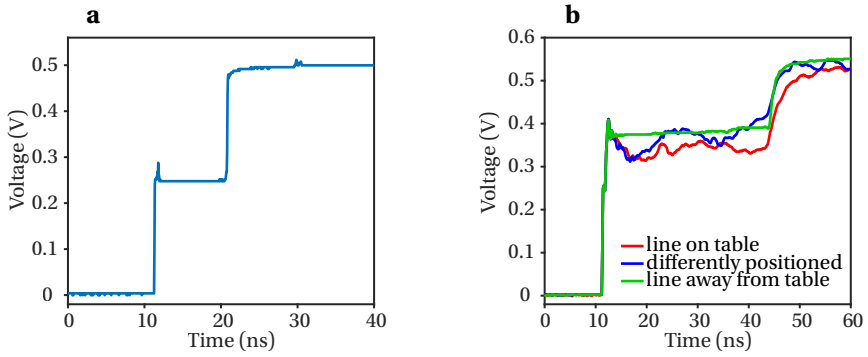

Figure 4.3 – Time-domain reflectometry measurements. a) Waveform for standard coaxial cable with characteristic impedance 50 Ω, showing the input pulse and the reflection at the open circuit termination. b) Waveforms for a liquid metal transmission line with the two-wire design, which is placed on a metallic table in two different configurations and suspended in air at a large distance to the table, illustrating the undesired interactions of the line with its environment.

designs, two-wire and coaxial, are shown in Figure 4.2c. For two-wire, the waveform exhibits an uneven profile, which depends on its interaction with the environment (Figure 4.3b). As a medium of higher dielectric constant than air is introduced around a section of the line, a positive time shift of the open circuit termination reflection and a negative reflection at the interface of air to ethanol/water is observed. For designs where the electrical field is not contained within the structure, the medium affects the propagation of signals through the line, because it changes the apparent dielectric constant. In the case of time-domain reflectometry, the effect on the measured waveform is twofold: (i) a reflection at the air–medium interfaces with an amplitude that depends on the change in apparent dielectric constant, and (ii) a time shift of the reflection at the open circuit termination. The effect is particularly noticeable for the two-wire design because it does not have an effective shield. As the employed media in the test are water and ethanol with higher dielectric constants than air, the reflection at the interface is negative. Additionally, the propagation speed in the section with the higher apparent dielectric constant is reduced, resulting in a positive time shift of the reflection at the open-circuit termination. Thus, time-domain reflectometry reveals both the nature of the medium, identified by its dielectric constant, and the section of the transmission line which is surrounded by it [134]. While this behavior harbors a significant potential for spatially resolved materials diagnostics and monitoring of physical parameters [119, 120], it is considered detrimental in this work dedicated to the unambiguous measurement of deformations. For the coaxial design, in contrast to two-wire, no discernible deviations in the smooth waveform occur when the line is introduced in a medium. The shield performance for all considered designs is summarized in Figure 4.2d, quantified by the time shift of the line end reflection due to the surrounding medium. While the coaxial line undergoes a negligible time shift, it is closely followed by the triangular structure, which also stands out due to its simpler design, which eases line fabrication and connection.

With the shielding behavior of different transmission line designs discussed, we turn next to a

description of losses, which are quantified by the attenuation coefficient. The presented liquid metal transmission lines can be approximated as low-loss lines, for which the attenuation coefficient α can be expressed by [137]:

$$\alpha \simeq \frac{1}{2}\left(\frac{R}{Z_0} + G \cdot Z_0\right), \tag{4.2}$$

where Z_0 is the characteristic impedance and R and G the series resistance and shunt conductance per length, respectively. In our analysis, we focus on the resistive term, which is expected to dominate over the dielectric term, because the loss tangent of the dielectric SEBS is low (0.07 at 3.5 GHz) [135], while the resistivity of the conductor Ga-In-Sn is high ($3 \cdot 10^{-7}\,\Omega$.m) [138]. As the two attenuation-controlling parameters, we shall first consider the characteristic impedance and then the resistance per length.

For a low-loss transmission line, the characteristic impedance is [137]:

$$Z_0 \simeq \sqrt{\frac{L}{C}}, \tag{4.3}$$

where L is the series inductance and C the shunt capacitance per length. Thus, it depends on the geometry of the transmission line. For a coaxial structure it can be approximated as [139]

$$Z_0 \simeq \frac{1}{2\pi} \cdot \sqrt{\frac{\mu}{\epsilon}} \cdot \ln\left(\frac{D}{d}\right) \tag{4.4}$$

where μ is the permeability, ϵ the permittivity, and D and d the outer and inner conductor diameter respectively. For the triangular structure, the characteristic impedance is [140]:

$$Z_0 \simeq \frac{1}{6\pi} \cdot \sqrt{\frac{\mu}{\epsilon}} \cdot \ln\left(H + \sqrt{H^2 - 1}\right), \tag{4.5}$$

where H is the geometric factor. It depends on the center-to-center spacing between center to shield wire s and the center and shield wire radius r_i and r_o, respectively:

$$H = \frac{\left(s^2 - r_o^2\right)^3 - r_i^6}{r_i^3\left[(s + r_o)^3 - (s - r_o)^3\right]}. \tag{4.6}$$

Now that we have established the term of the characteristic impedance in equation 4.3, we can turn to the resistance per length. The resistance per length due to skin effect is [141]:

$$R = \frac{R_S}{A}, \tag{4.7}$$

where R_S is the skin resistance and A the conductor surface area per length. The skin resistance is [141]:

$$R_S = \sqrt{\frac{\omega\mu}{2\sigma}}, \tag{4.8}$$

where ω is the angular frequency, μ the permeability, and σ the conductivity. Thus, the resistive term of the attenuation coefficient can be expressed as:

$$\alpha_c = \frac{1}{2} \cdot \frac{1}{Z_0 A} \cdot \sqrt{\frac{\omega\mu}{2\sigma}}. \tag{4.9}$$

This expression gives an insight into the relevant parameters, which dictate the loss in the transmission lines, and can be used to explain results that were obtained experimentally.

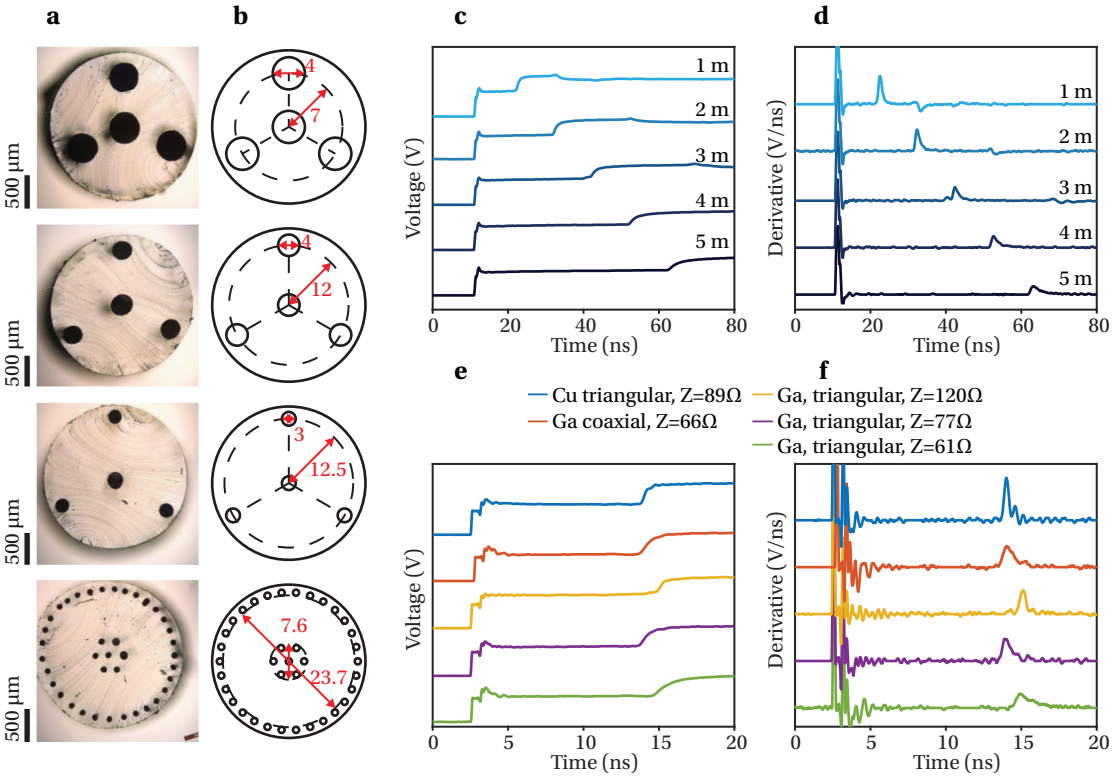

Figure 4.4 – Signal distortion in time-domain reflectometry measurements. a) Optical micrographs of considered designs for liquid metal transmission lines. Triangular structures with increasing conductor spacing-to-diameter-ratios, and a coaxial structure are displayed. b) Dimensions of the structural features of the designs in the preform in mm. The characteristic impedance can be calculated based on the indicated structural features. c) Time-domain reflectometry waveforms observed for liquid metal triangular transmission lines of increasing lengths. d) Derivatives of the waveforms, illustrating the increase in broadness of reflections at the open circuit termination. e) Time-domain reflectometry waveforms of transmission lines with different conductor materials (liquid metal Ga, solid copper Cu), structure type (triangular, coaxial), and characteristic impedance (Z), illustrating the correlation between determined attenuation coefficient and broadening of the reflection at the open-circuit termination. f) Derivatives of the waveforms.

To decouple effects originating from material and structure in experiments, as well as obtaining a baseline for the novel liquid metal lines, we compare their characteristics to more conventional solid metal lines with the same architecture and dimensions. The latter are fabricated in fiber-form through an adaption of the Taylor process [38], which involves Cu

wires of diameter 250 μm being introduced into empty channels of an SEBS preform, and the thermal drawing of the assembly (Figure 4.2e).

In Figure 4.2f, the attenuation coefficient is shown for three differently dimensioned triangular and a coaxial line based on liquid metal, as well as a triangular solid metal line. As expected, the attenuation coefficient of all considered lines follows roughly a square root relationship to the frequency, which is an indication of loss being dominated by the skin effect. This resistive loss depends on the conductor material, explaining the higher attenuation coefficient of lines based on Ga-In-Sn ($\sigma = 3.3 \cdot 10^6 \text{S.m}^{-1}$) [138] compared to Cu ($\sigma = 5.8 \cdot 10^7 \text{S.m}^{-1}$ [137]. Albeit limited by the material's resistivity, attenuation can also be tuned through structural changes. This includes an increase in conductor surface, which was implemented in the coaxial design through a division of the centre and outer conductor into 7 and 32 microchannels, respectively. While the attenuation coefficient of the coaxial line is indeed lower than the triangular lines at lower frequencies, it increases at an elevated rate for frequencies above 1 MHz, presumably due to the proximity effect [142]. Alternatively, the resistive term of the attenuation coefficient can also be reduced by an increase in characteristic impedance, which is readily realized in triangular lines through a higher ratio of inter-conductor spacing to conductor diameter (Figure 4.4a, b). The frequency-dependent attenuation in the transmission lines results in signal distortion in the time-domain [141], a detrimental effect observed in reflectometry measurements (Figure 4.4c, d, e, f). As will be shown below, pulse broadening is the limiting factor for the spatial resolution of distributed probes consisting of liquid metal lines. In this regard, triangular designs with a higher characteristic impedance are considered promising candidates because they undergo lower losses.

4.4 Distributed probes of multimodal deformations

To deepen the understanding of the electromechanical coupling and highlight the value of employing liquid metals, we investigate the electrical response to pressing by comparing transmission lines composed of liquid metal microchannels to lines based on solid metal wires. Both types of lines consist of the triangular configuration and have comparable dimensions. Additionally, the dielectric in both cases is the elastomer SEBS, and, thus, while not being stretchable, the solid metal-based lines are also compressible. In the test, a point force ramp is applied orthogonally halfway along the length of 1 m-long transmission lines (Figure 4.5a). For both types, a larger force results in an increasing reflection at the time that corresponds to the pressing position along the lines. However, the shape of the reflected wave and the force magnitudes, under which the reflection occurs, differ significantly. For the liquid metal lines, a positive step is produced in the waveform at forces as low as 2.5 N, which increases in amplitude at an approximate rate of 20 mV.N^{-1}, whereas, for solid metal lines, a negative peak first appears at a larger force of 10 N and rises at a significantly smaller rate of approximately 0.1 mV.N^{-1}. The dissimilar electrical responses are the result of the mechanisms under which the lines deform, which are dictated by the disparate mechanical properties of the two types of conductors, as schematized in Figure 4.5b. Under increasing pressure, the channels locally

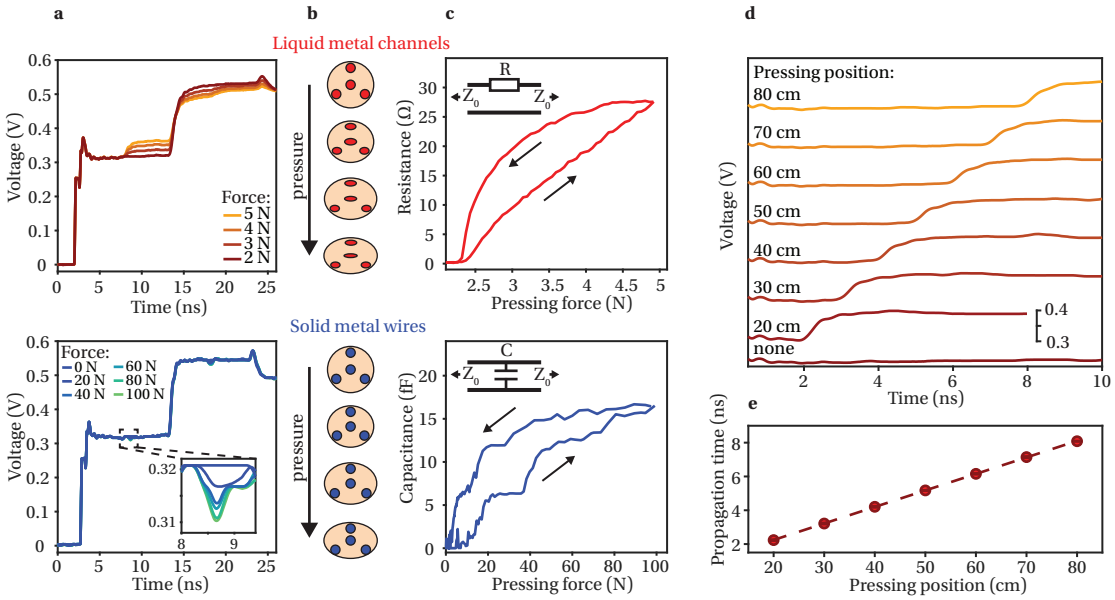

Figure 4.5 – Pressing on soft transmission lines. a) Waveforms of a liquid metal (top) and solid metal (bottom) triangular lines of length 1 m loaded at 50 cm with an increasing pressing force. b) Schematic of the cross-sectional deformation mechanism of lines under increasing pressures. The liquid metal microchannels collapse in a controlled fashion (top), whereas the solid metal wires are unaffected and merely their spacings are varied (bottom). c, Resistance R of a single series resistive discontinuity for liquid metal channels (top) and capacitance C of a single shunt capacitive discontinuity for solid metal wires (bottom) along the line of otherwise unchanged characteristic impedance Z_0 calculated based on the reflection in the waveforms as a function of pressing force. The loading and unloading path are indicated by arrows. d) Waveforms for pressing of equal force but varying position along liquid metal lines. The initial signal rise and connector ringing, as well as the final termination reflection are cut for clarity. e) Propagation time of the signal to the discontinuity and back as a function of pressing position calculated from the waveforms.

close in a controlled fashion, thus increasing their resistance [143]. In the solid wire–elastomer structure, however, only the spacings between the center and shield conductors vary, inducing a change in capacitance.

With this knowledge, the magnitude of the discontinuities can be calculated based on the reflection in the waveforms. For a single resistive discontinuity in series, the resulting step in the waveform can be quantified by a reflection coefficient, which is the ratio of reflected to incident voltage. The magnitude of the resistance R_S can be deduced from the reflection coefficient ρ [133]:

$$R_S = 2 \cdot Z_0 \cdot \frac{\rho}{1-\rho}, \tag{4.10}$$

where Z_0 is the characteristic impedance of the line. A shunt capacitive discontinuity, however, causes a negative peak in the waveform. Its magnitude C_P can be approximated by the peak

value in the waveform V_{peak} [144]:

$$C_P \simeq \frac{|V_{peak}|}{1.1 \cdot Z_0} \cdot \frac{t_{rise}}{U_i}, \tag{4.11}$$

where t_{rise} is the rise time and U_i the amplitude of the incident step.

Using these equations, the two types of discontinuities can be calculated based on the waveforms obtained in the force ramp experiment (Figure 4.5c). For the liquid metal transmission lines, the calculated resistance as a function of pressing force corresponds to previous measurements under direct current conditions (Figure 4.1g) and exhibits similar advantageous force range, sensitivity, reversibility, and repeatability. For a measurement instrument with a voltage resolution of 4 mV, the sensitivity of 20 mV.N^{-1} implies a force resolution of the transmission line of 0.2 N on the loading path. This sensitivity is higher by a factor of 200 than the value of 0.1 mV.N^{-1} found for compressible Cu-wire transmission lines. Additionally, the solid metal lines produced signals that are detectable only at large forces, and even under forces as large as 100 N the signals range on the order of fF (10^{15} F), which represents a measurement near or beyond the limitations of most measurement instruments. Thus, despite lower losses, the Cu wire lines are considered less effective pressure sensors. Finally, as the cross-section of the employed triangular configuration is not circularly symmetric, we also investigated the effect of the relative angle of the pressing force. However, no discernible effect of the orientation is identified in the force-dependent waveforms, enabling the use of triangular liquid metal transmission lines as omni-directional pressure probes.

With the inherent spatial resolution of reflectometry, pressures can be both quantified and localized on the soft transmission lines. While the amplitude of a generated step in the waveform correlates to the pressing force magnitude, the time at which it occurs indicates the position of the pressure. From the waveforms generated for differently placed discontinuities (Figure 4.5d), we extract the propagation times of the signal from the interrogated line end to the discontinuity and back (Figure 4.5e). The measured propagation time remains stable under variable pressing forces with maximum fluctuations of ± 0.06 ns, implying a spatial precision of <1 cm. As shown in Figure 4.5e, the propagation time is a linear function of the pressure position with the slope depending only on the propagation speed, which was previously determined for SEBS. Thus, the permittivity of the employed dielectric represents the only parameter necessary for the accurate localization of pressures on the transmission lines and no sensor calibration is needed in applications, regardless of line length and diameter or contact resistance.

Furthermore, multiple pressure points on a transmission line, interrogated only from one end, can be simultaneously analyzed. To easily identify multiple discontinuities, we establish a resistance distribution from the collected waveform for the timespan that corresponds to the length of the line (Figure 4.6a). In the calculation of the distributed resistance, we considered that the second reflection is diminished by the first discontinuity, as the voltage wave is partly transmitted and reflected at every discontinuity. For instance in the case of two discontinuities,

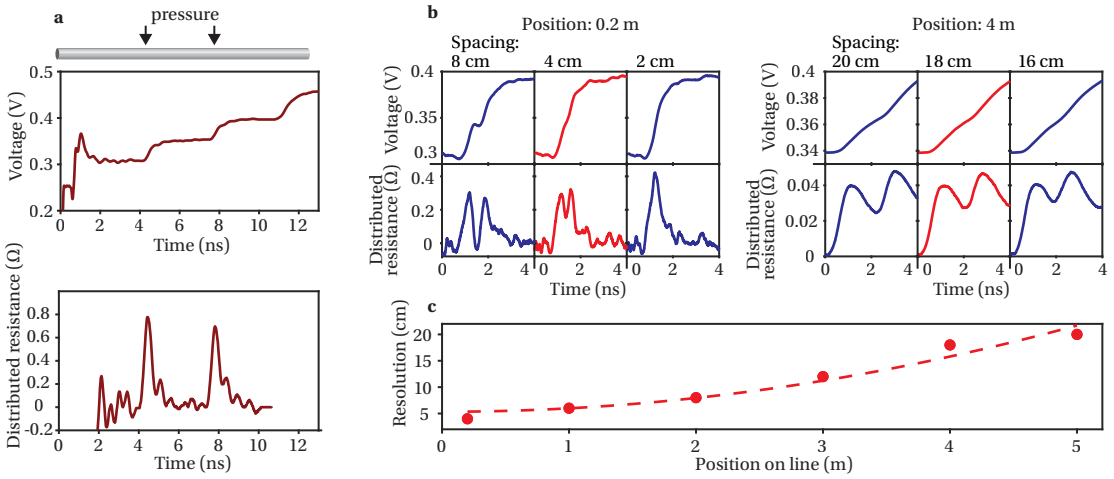

Figure 4.6 – Multiple pressure points on soft transmission lines. a) Two pressure points are applied at 33 cm and 66 cm from the interrogated end on a 1 m-long liquid metal line, inducing steps in the waveform (top). Based on the reflections in the line, a distributed resistance is established, in which the pressure points appear as distinct peaks (bottom). b) The spatial resolution of pressure sensing is investigated by applying two pressure points of equal magnitude at different positions from the interrogated end. The waveforms and distributed resistance profiles are shown for two positions and three different spacings between the two pressure points. The resolution is defined as the spacing where the valley in the distributed resistance profile between the two peaks is equal to 70 % of the higher of the two peaks, highlighted here in red. c) The extracted spatial resolution is shown as a function of position along the length of the transmission line probe.

the reflection at the second discontinuity is diminished by the transmission –reflection at the first discontinuity before reaching the monitored line end [133].

We employ a recursive algorithm to calculate the true reflection coefficient ρ_i for each time step i in the waveform [121]:

$$\rho_i = \frac{\Delta U_i}{U_0 \cdot \prod_{j=0}^{i-1}(1+\rho_j)}, \tag{4.12}$$

where ΔU_i is the amplitude of a discontinuity-generated measured voltage step and U_0 the incident voltage. In this strategy, only the first reflections at the discontinuities are considered, which are partly transmitted at previous discontinuities. The subsequent geometric series of internal multiple reflections, each weaker than the last, is neglected. Based on the calculated true reflection coefficient, the resistance is calculated using the equation 4.10, resulting in a resistance distribution for the soft transmission lines.

In the resistance profile (Figure 4.6a bottom), the two pressure points appear as distinct peaks. As the peaks are broadened by the finite bandwidth of the measurement instrument and the attenuation in the line, the magnitude of the point discontinuities on the line corresponds

to a summation of the peak values. The maximum number of pressure points that can be simultaneously detected is dependent on the employed instrument's input voltage and voltage resolution. In our case, reflections of a 500 mV step are detected at a resolution of 4 mV, resulting in a theoretical maximum of 125 pressure points. In this calculation, it is assumed that pressing forces are applied that induce voltage steps equal to the resolution. Larger forces will reduce the number of points that can be detected, and, thus, the line must be arranged according to the expected pressure distribution to avoid cutting off parts of the line in real applications. The capabilities of the proposed sensor system can be extended by interrogating the line from both ends as well as employing multiple lines in application-targeted networks, representing two strategies commonly employed in the field of functional fibres and smart textiles [13, 15, 67].

We assess the spatial resolution experimentally by determining the minimum spacing between two pressure points of equal magnitude that can be resolved separately (Figure 4.6b). When the line is loaded close to the interrogated end, shown here for 0.2 m, two pressure points distanced 8 cm from one another appear as sharp steps in the waveform and distinct peaks in the resistance profile. As the spacing is reduced, the peaks start to overlap up to the point where they merge into a single peak at a spacing of 2 cm, at which point they cannot be resolved separately anymore. We define the spatial resolution as the spacing, where the valley between the two peaks is equal to 70 % of the higher of the two peaks, corresponding here to 4 cm. However, the spatial resolution is not constant along the length of the line but depends on the distance of the pressure points to the interrogated end. Considering, for instance, the two pressure points being applied 4 m down the line, a broadening of the originally sharp peaks in the resistance profile is observed, an effect attributed to the signal attenuation in the lines, resulting in an increased spatial resolution of 18 cm. Through repetitions of this procedure at different distances from the interrogated end, the resolution is extracted as a function of position on the line (Figure 4.6c), ranging from 4 cm at 0.2 m to 20 cm at 5 m. As shown in the plot, the spatial resolution appears to follow a quadratic dependency on the position, which corresponds to theoretical predictions. When considering a perfect unit step function as an input waveform, the changed shape of step response can be described by [141]:

$$\begin{aligned} U(t) &= U_0 \cdot erfc\left(\frac{z \cdot k}{2 \cdot \sqrt{t}}\right) \\ &= U_0 \cdot erfc\left(\sqrt{\frac{\tau}{t}}\right), \end{aligned} \tag{4.13}$$

where U_0 is the amplitude of the input step, erfc the complementary error function, z the distance down the line, k a constant for the skin effect, and t the time. The time constant τ can be employed to quantify the pulse broadening. It is indeed proportional to the square of the line distance, agreeing with the experimental observation.

We conclude that the spatial resolution is dictated by the instrument for small distances but is quickly overtaken by line attenuation as the dominating resolution-limiting mechanism

for pressure positions further down the line. In applications involving long lines and severe localization requirements, the lines can also be interrogated on both ends, resulting in an improved spatial resolution.

Having established spatially resolved pressure sensing, we investigate the response of elongation from 0 to 100 % of the lines in time-domain reflectometry (Figure 4.7a). By stretching the line, the open circuit termination reflection is shifted towards higher times due to the increased length. The relationship of propagation time to elongation is found to be linear (Figure 4.7b), confirming an unchanged propagation speed in the stretched lines. Furthermore, the dependency is fully reversible with negligible hysteresis and exhibits a sensitivity of 0.1 ns.%$^{-1}$ for a 1 m-long line, implying a strain resolution of 0.25 % when using an instrument with a temporal accuracy of 25 ps. Note that, although plotted here as a function of the relative quantity strain, the propagation time yields directly the absolute length of a stretched line.

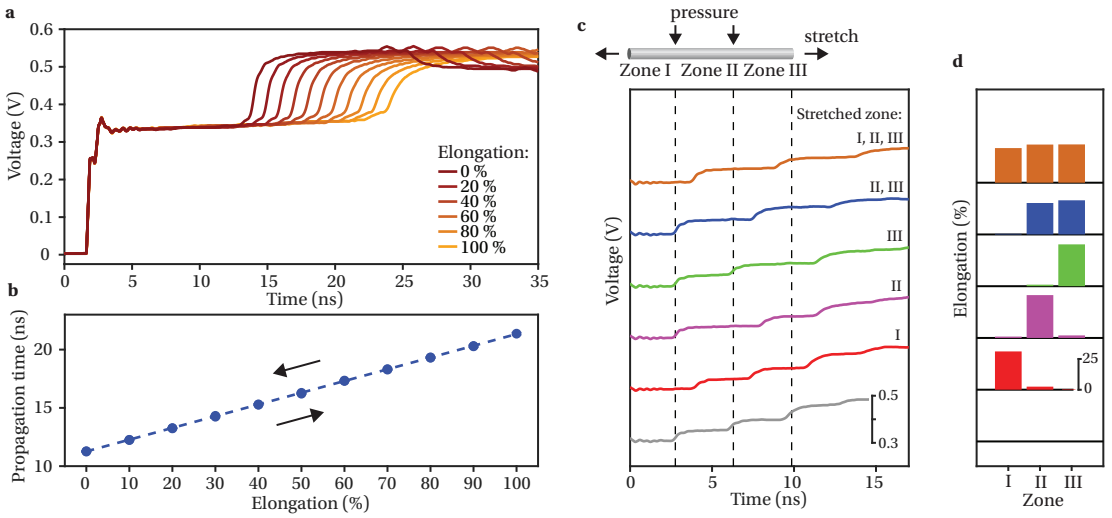

Figure 4.7 – Stretching of soft transmission lines. a) Waveforms of a triangular liquid metal line being stretched to increasing elongations, resulting in a time shift of the reflection at the open circuit termination. b) Propagation time of the signal in the line extracted from the waveforms as a function of applied elongation. The plot includes the loading and unloading path, which overlap near perfectly. c) A 1 m-long transmission line is locally compressed at 33cm and 66cm as a mean of discretizing the line into three zones for localized strain sensing. Selective stretching results in an increased propagation time in only the corresponding zones, as shown by a time shift of the steps in the waveform. d) Based on the change in propagation time, the elongation can be directly calculated for each zone, related to each loading case shown in c by the color of the plot.

Besides the time-shifted termination reflection, the voltage trace remains unchanged. This is, firstly, due to the low-loss nature of the line for which the characteristic impedance is dominated by capacitive and inductive rather than resistive contributions, and, secondly, because cross-sectional dimensions vary homogeneously when the line is stretched. Considering the simple geometry of a coaxial line [139], the characteristic impedance Z_0 as a function of strain

e can be expressed as:

$$\begin{aligned} Z_0(e) &\simeq \frac{1}{2\pi}\frac{\mu}{\epsilon} ln\left(\frac{D(e)}{d(e)}\right) \\ &= \frac{1}{2\pi}\frac{\mu}{\epsilon} ln\left(\frac{D_0 \cdot (1-\nu e)}{d_0 \cdot (1-\nu e)}\right) \\ &= \frac{1}{2\pi}\frac{\mu}{\epsilon} ln\left(\frac{D_0}{d_e}\right) \end{aligned} \tag{4.14}$$

where μ is the permeability, ϵ the permittivity, D and d the outer and inner conductor diameter respectively, and ν the Poisson ratio. Thus, the characteristic impedance remains constant for any elongation. The same reasoning can be made for the triangular transmission line design using equation 4.5.

While a constant characteristic impedance for arbitrarily stretched transmission lines may prove beneficial in communication, the lack of reflections hinders the localization of section-wise applied elongations in sensing applications. To obtain position information, we introduce discontinuities on the line to discretize it into sections. As previously shown, this is readily achieved for soft transmission lines by locally applying controlled pressures, generating steps in the waveform (Figure 4.7c). As elongations are applied selectively in one or several of the three created zones, the propagation time increases only in the corresponding sections, as indicated by a time shift of the voltage step (Figure 4.7d). While this strategy demonstrates the ability of localizing and quantifying stretching in transmission lines, it proves impractical in applications where spatially resolved sensing of both stretching and pressing is targeted. In such use cases, discontinuities for discretization of a different nature, for instance capacitive which induce negative peaks in the waveform, can be introduced as not to interfere with the signals generated for pressing.

As two supplementary modes of deformation, we investigate the effect of torsion and bending on the soft transmission lines. Similarly to an axial strain, increasing levels of twisting, up to 100 full revolutions per meter of length, for a line that is held at a constant end-to-end distance, result in a positive time shift of the open circuit termination reflection (Figure 4.8). The increase in propagation time of the signal is attributed to the helical lengthening of the outer shield wires brought upon by the torsional deformation [145], which is expected to be zero at the center of the twisted line and to increase linearly in the radial direction. For line bending however, the accompanying deformations of the liquid metal channels are beyond the detection levels of our instruments. Indeed, even at the minimum attainable radius of curvature at which line sections on either side of the bend are parallel and in contact, the changes in length and cross-section are too small to result in a significant difference in propagation time or impedance, respectively.

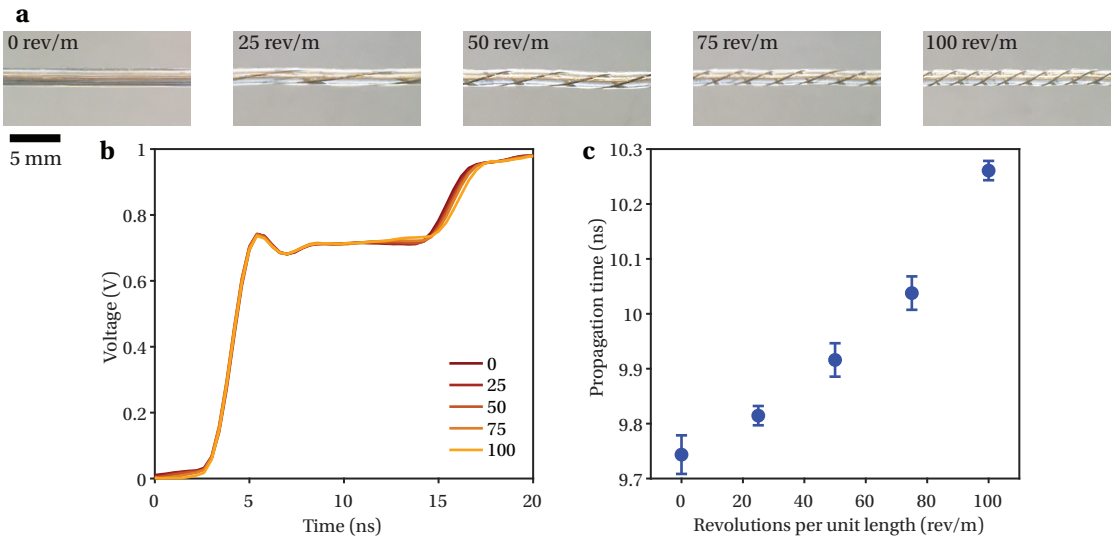

Figure 4.8 – Twisting of soft transmission lines. a) Photographs of a triangular liquid metal line being twisted to increasing degrees of torsion, quantified by the number of revolutions per meter of length. b) Time-domain reflectometry waveforms of twisted lines, exhibiting a positive shift in time of the open circuit termination reflection for increasing levels of twist. c) Propagation time of the signal in the 1 m-long lines extracted from the waveforms as a function of number of revolutions. The error bars indicate the standard deviation. The increase in propagation time is attributed to the helical lengthening of the outer shield wires due to the torsional deformation.

4.5 Multiplexed deformation sensing in electronic textile

The capabilities of the soft transmission line probes are demonstrated in practice by integrating a 10 m-long line on a stretchable piece of fabric of size 50 cm x 50 cm (Figure 4.9a). A serpentine pattern with a spacing of 3 cm is selected, which enables the functionalization of the entire surface with an individual line, interfaced through a single point. Since specialized time-domain reflectometers are expensive, delicate, and large-footprint instruments, we employ a custom pulse generator with costs in parts of less than US$ 10 coupled with a standard laboratory oscilloscope. Although the produced and captured signal exhibits some ringing and a higher rise time of 5 ns, limiting the positional accuracy to approximately 25 cm, it represents a first step towards a practical and cost-effective solution. In the context of cost, the oscilloscope is the critical element of the system, resulting in a trade-off between low cost and high spatial accuracy. Nonetheless, the proposed sensing strategy is distinguished by its unique capability, including the decoupling of different deformation modes and the continuous measurement of stimuli magnitude and location. Furthermore, the approach based on a single sensor unit offers a straightforward implementation for any geometry and loading case, compared to commonly employed grids of point sensors that must all be addressed selectively through numerous delicate contact points, but also networks of fiber-based sensors without spatial resolution.

We submit the electronic textile to a series of tests, where controlled mechanical stimuli are

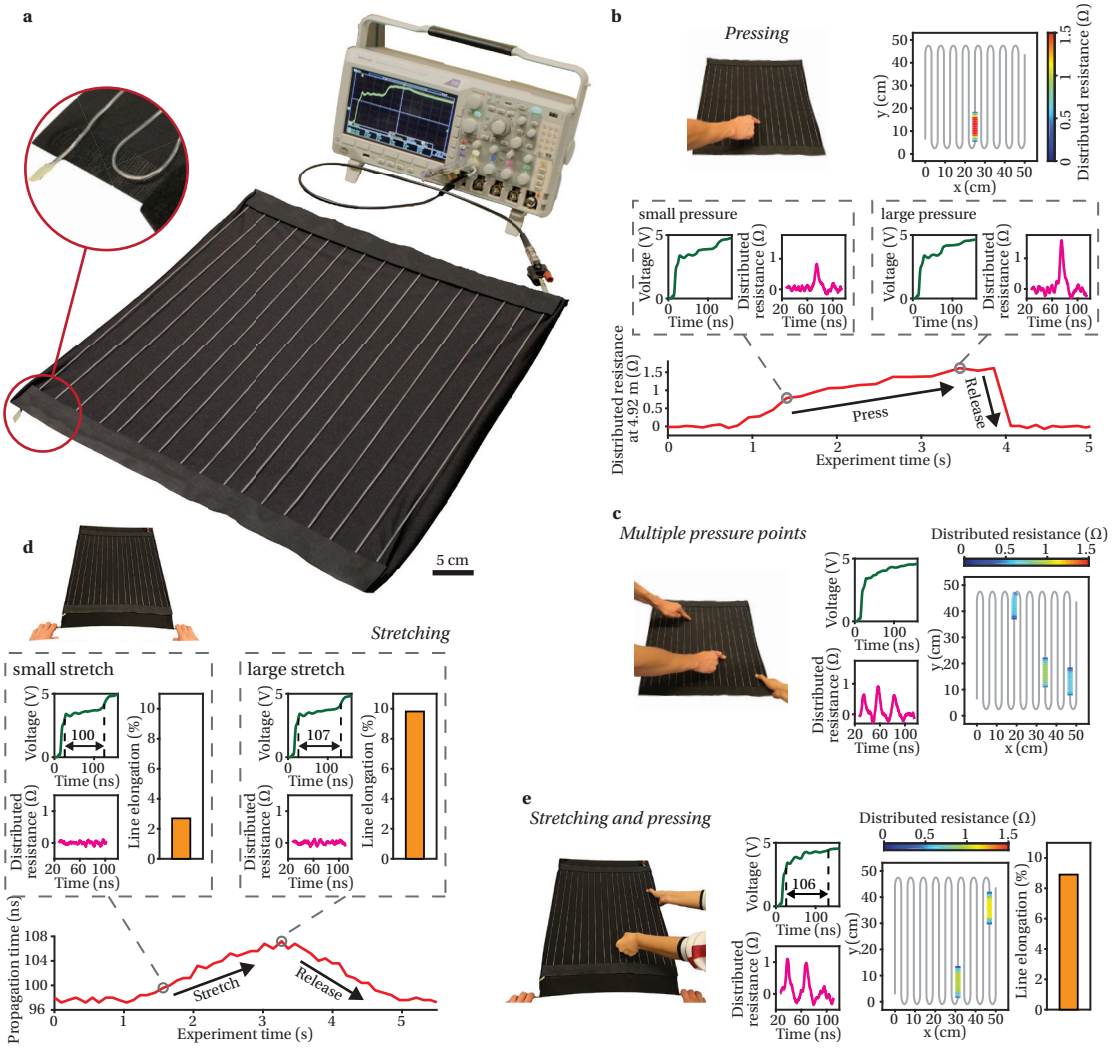

Figure 4.9 – Electronic textile for multiplexed deformation sensing. a) A 10 m-long triangular liquid metal transmission line probe is integrated in a serpentine pattern on a stretchable fabric and is interfaced through a single contact point. The inset shows the open circuit termination and one of the line loops that is fixed in the textile by Velcro strips. A custom pulse generator of small footprint and low cost coupled with a standard oscilloscope are used to interrogate the textile. b) An increasing pressure is applied by a finger on the textile. The waveform and distributed resistance are shown for a small and large pressure. The peak resistance values are laid out in a two-dimensional color-coded spatial map according to the arrangement of the line on the textile, on which the location of the pressure event is accurately represented. c) Three pressure points are simultaneously applied on the textile, and their magnitude and position extracted from the waveform, as shown by the three peaks in the distributed resistance profile and the highlighted sections in the map. d) The entire textile is stretched in the longitudinal line direction. Two snapshots in a stretching event are shown by the waveform, on which the propagation time in the line is highlighted, the distributed resistance profile, which remains unchanged, and the line elongation that is directly calculated from a change in propagation time. The continuous measure of the propagation time is shown for a complete stretching cycle. e) The textile is simultaneously exposed to the two modes of deformation, stretching and pressing. The configuration of the textile is reconstructed based on waveform and visualized in the map, which shows the elongated shape of the textile as well as pressure points.

applied on the probe. In the application, we limit ourselves to pressing and stretching, because these two modes of deformation represent the most relevant mechanical stimuli in functional textile applications and cause easily distinguishable responses in time-domain reflectometry. First, an individual pressure point is applied by a finger (Figure 4.9b), generating a step in the waveform and a peak in the distributed resistance profile, the height of which corresponds to the applied pressure. The peak value is shown for a complete cycle of pressing and releasing, demonstrating the continuity and reversibility of the measure. The waveform and resistance profile for two snapshots, corresponding to a small and large pressure are shown in the main figure. The time in the spectrum at which the resistance peak occurs reveals the position of the pressure point, determined here to be 4.92 m from the interrogated line end. As an intuitive visualization, the peak resistance values are laid out in a color-coded map, indicating the position and magnitude of pressure events. Next, multiple pressure points are simultaneously applied on the functional textile to test the multiplexing capability of the probe (Figure 4.9c). Indeed, the three applied pressure points appear as distinct peaks in the resistance profile and are accurately positioned on the spatial map. As a second mode of deformation, we stretch the fabric in the longitudinal line direction (Figure 4.9d). Unlike pressing, this stimulation does not generate a local discontinuity in the waveform but increases the propagation time, quantified by a positive time-shift of the open circuit reflection. We display the line propagation time for a cycle of stretching and releasing, as well as two snapshots corresponding to a small and large strain. In a final test, we aim at the simultaneous detection of pressing and stretching based on the disparate responses of the two modes of deformation. Indeed, the signals can be successfully decoupled, and the two pressure points are accurately resolved as well as the elongation quantified (Figure 4.9e).

All loading scenarios displayed here are extracted from one experiment and the video and data stream can be found at https://www.nature.com/articles/s41928-020-0415-y. The experiment underlines how the actual configuration of the large electronic textile, which may undergo convoluted changes in the form of pressures and stretches, can be reconstructed based on the time-domain reflectometry measure of a single probe interfaced through a single contact point.

4.6 Conclusion

We have reported a class of soft and stretchable transmission lines consisting of liquid metal microchannels arranged within a thermoplastic elastomer dielectric. Our fabrication technique uses thermal drawing, where a soft material preform is converted into a fibre in a regime dominated by viscous forces. Thanks to diverse possible architectures and uniform cross-sections over extended lengths, the fibres can perform as soft transmission lines with controlled impedances, shielding, and losses. The experimental and theoretical exploration of the mechanisms of electromechanical coupling, where both soft and hard–soft hybrid structures are studied, illustrate the capabilities of liquid metal lines for use as distributed probes of multimodal deformations through interrogation by time-domain reflectometry. These

capabilities include high sensitivity, complete reversibility, and large deformation ranges. Our sensing approach enables the functionalization of large, flexible, and stretchable areas of various substrates and form factors with a single sensor unit interfaced through a single contact point, which includes a continuous measurement of magnitude and position of pressures and stretches. From the range of outputs that the soft transmission lines produce, convoluted mechanical stimulation could be reconstructed in electronic textiles, wearable devices, and robotic skins.

4.7 Experimental Section

Fabrication and connections of soft transmission lines

Liquid metal microchannel fibers. Granules of SEBS (Kraton) were filled in a custom mold of the desired shape (cylindrical or rectangular), which included cylindrical cores of variable diameter fixed to the base plate, and the assembly was hot-pressed at 0.5 bar, 180 °C for 6 h. The polymer preforms were thermally drawn into fibers using a custom draw tower at a maximum temperature of 160 °C and at variable take-up speeds, thus controlling the fiber diameter and length. The liquid metal Ga-In-Sn (Indium Corporation) was injected with a syringe into the structure before the drawing step for channels diameters smaller than 1 mm in the preform and directly into the fibers for larger preform channel diameters. Steel wires were inserted into the liquid metal channels at the fiber ends, and the connection point was sealed with an adhesive.

Solid metal wire fibers. The polymer preform was prepared as stated in the previous section. For the drawing process, Cu wires of diameter 250 μm (McMaster) were fed into the empty channels of the suspended preform, and the assembly thermally drawn at a temperature of 200 °C. As the polymer flowed into a fiber, the wires were caught by the narrowing channels and continuously unspooled as the polymer was drawn. Note that in our technique the wires do not melt or change shape otherwise. For connection, the wires at the fiber ends were stripped of the encapsulating polymer.

Direct current characterizations

Pressing response test. Fibers of length 1 m with liquid metal microchannels in the triangular configuration were short-circuited at the far end and connected to an electrometer (Keithley Sourcemeter 2400) at the near end with the center and outer conductors connected to the positive and negative pole, respectively. The fibers were locally and repeatedly compressed under controlled forces (3 $N.min^{-1}$) in a dynamic mechanical analysis setup (DMA, TA Instrument DMA Q800), where a steel rod of diameter 6 mm positioned perpendicularly to the fibers served as an indenter. During the test, the direct current resistance, pressing force, and indenter displacement were continuously recorded.

Stretching response test. Fibers of length 15 cm with liquid metal microchannels in the two-wire configuration were short-circuited on one end and connected to the electrometer on the other end. Fiber sections of length 8 cm were repeatedly stretched in a custom linear motion drive setup and the direct current resistance monitored continuously.

Analysis of loss

The impedance of 1 m-long transmission lines was measured at a voltage amplitude of 1 V using an impedance analyzer (Zurich Instruments HF2LI Lock-in Amplifier). In this test, lines were interfaced to the instrument through a wire-to-BNC adapter on the near end, where the center and outer conductors were coupled to the positive and negative pole, respectively, and left in open circuit or short circuit configuration on the far end. The attenuation coefficient was calculated based on the short circuit impedance and the open circuit admittance, corresponding to the series resistive and inductive or shunt conductive and capacitive contributions, respectively, as described in reference [146]. The measurements were carried out over the frequency range 10 kHz - 10 MHz, as higher frequencies could not be realized due to instrument limitations. While this frequency range does not encompass the entire bandwidth of the employed step in the time-domain, which for a 100 ps risetime extends into the GHz region, it allows to gain an insight into attenuation contributions and compare transmission line designs.

Time-domain reflectometry analysis

General setup. The near end of the transmission lines was connected to a wire-to-BNC adapter, and the far line end was terminated in an open circuit. The transmission lines were interrogated through a BNC interface by a digital sampling oscilloscope (Tektronix 11801C). Using the instrument, a voltage step of amplitude 0.5 V and with a rise time of approximately 100 ps was sent down the transmission lines and the resulting voltage transient across the lines recorded. An alternative setup for less time-sensitive measurements consisted of a pulse generator (Leo Bodnar) coupled to a standard oscilloscope (Tektronix MDO3014), yielding a voltage step of amplitude 1 V and recorded rise time of approximately 2 ns.

Shield characterization. The performance of the shield in soft transmission lines was evaluated by recording the time-domain reflectometry waveforms of 1 m-long lines, which were successively submersed in ethanol and deionized water for line sections 40 cm – 60 cm.

Pressing response test. For characterizing the response to pressing force magnitude, the triangular liquid metal transmission lines of length 1 m were compressed locally at a position of 50 cm using the same setup and configuration as in the direct current measurements, and the waveforms recorded continuously. Due to larger necessary forces, the triangular solid metal lines were compressed using a motorized force tester (Mecmesin Multitest 2.5-I stand with Mecmesin Basic Force Gauge load cell) at a controlled displacement of 1 $mm.min^{-1}$,

where also a steel rod of diameter 6 mm served as an indenter. The force-dependent induced reflections in the waveforms were quantified by a series resistance and a shunt capacitance for the liquid metal and solid metal lines, respectively. In the pressing force orientation test, the experiment was repeated after rotating the lines around the axial direction in 30° increments. For characterizing the response to pressure position, 1 m-long triangular liquid metal transmission lines were manually compressed at predetermined positions using the steel rod at a force that induced a reflection of amplitude 0.1 V, and the respective waveforms recorded. For the test involving multiple pressure points, vices were used to compress a 1 m-long line at positions 33 cm and 66 cm at a force magnitude that induced 50 mV reflections in the waveform, which was used to calculate the distributed resistance. The spatial resolution of the pressure sensing was assessed by applying two pressure points resulting in 50 mV reflections with the vices on a 6 m-long triangular line. The position, corresponding to the distance from the interrogated line end to the first pressure point, and the spacing between the two pressure points were varied. The position-dependent spatial resolution was defined as the spacing for which the corresponding resistance distribution exhibited a valley between the two peaks equal to 70 % of the higher of the peaks.

Stretching response test. Triangular liquid metal transmission lines of length 1 m were elongated in a custom linear translation stage and the waveforms recorded for controlled displacements. For the localized strain test, the 1 m-long lines were locally compressed by custom clamps at positions 33 cm and 66 cm at a force magnitude that resulted in 50 mV reflections. The line sections were selectively stretched by hand and the waveforms recorded.

Twisting response test. Triangular liquid metal transmission lines of length 1 m were clamped on either end in an extended configuration to maintain a constant end-to-end distance. One line end remained fixed while the other one was rotated around the axial direction by controlled amounts of up to 100 revolutions. The waveforms were recorded continuously during the entire test.

Bending response test. A 4 cm-long section of triangular liquid metal transmission lines of length 1 m was placed in between two parallel plates, forming a bend. The plates were approached to one another in controlled increments, resulting in bending radii of the lines from 12 to 2 mm, and the waveforms were recorded.

Electronic textile

Assembly. A 10 m-long triangular liquid metal transmission line was placed in a serpentine pattern with a spacing of 3 cm on a stretchable fabric of size 50 cm x 50 cm. The line loops were fixed in place using Velcro strips that were glued on two sides of the fabric. The line was interfaced through a wire-to-BNC adapter on one end and left in open circuit configuration on the other end. A custom square wave generator in conjunction with a standard oscilloscope (Tektronix MDO3014) were used to interrogate the line. The recorded waveforms were transferred to a PC, where they were processed in real time by an algorithm (MathWorks MATLAB)

to extract the variable line length and distributed resistance. Since the propagation speed is known for the dielectric SEBS, no calibration for the localization of stimuli is necessary.

Testing. For approximating the spatial resolution, the line was locally compressed in 25 cm steps for the entire length, and the overlap of distributed resistance peaks assessed. For the pressing test, fingers were firstly placed at arbitrary positions along the line without applying pressure to underline that the sensor only reacts to a mechanical deformation rather than changes in its environment. Afterwards, pressure was progressively increased by the fingers, demonstrating the continuity in pressure location and magnitude measurement. For the stretching test, metal rods were fixed on two sides of the textile orthogonally to the line, and pulled apart and brought back together. The captured waveforms were continuously recorded and processed at an average frequency of 7.4 Hz, enabling real-time deformation visualizations in the electronic textile during all the tests.

5 Soft robotic fibers with optical, electrical, and fluidic functionality

Thus far, we have investigated several strategies for mechanical sensing in soft functional fibers. In this Chapter, we address actuation to generate targeted movements with the fibers. Coupled with sensing, the actuation functionality promotes the resulting fibers to capable robots.

5.1 Motivation

Soft robots hold great potential in applications involving the human body because they can safely conform and interact with fragile and dynamic environments [3]. In such compliant and deformable robotic systems, movement is enacted by one of numerous possible actuation mechanisms, based on tendons [147], pneumatics [148], hydraulics [149] , shape memory effects [150], or electrical [151] or magnetic [152] activation — each with their own strengths and weaknesses [1, 153–155]. To accomplish meaningful tasks, actuation is often coupled with additional functionalities, such as sensing [81], imaging [156], optical [157] or electrical [158] transmission, and drug delivery [159].

Multi-functional soft robots are particularly promising in tubular form to act as steerable catheters and endoscopes in minimally invasive procedures [160–162]. However, creating the soft multi-material assemblies, which are necessary for dexterous movement and embedded functionality [1, 153], at relevant diameters (< 3 mm) and lengths (>300 mm) is a feat that cannot be accomplished to date, neither by conventional extrusion-based techniques [163, 164], nor by approaches adopted from macroscopic soft robotics relying on molding [165], stereolithography [166], 3D printing [167], and manual processing [168].

We hypothesized that such high-aspect-ratio materials constructs could be realized by the thermal drawing process, which is conventionally employed for the fabrication of optical fibers and typically yields fibers of diameter 125 µm and length 1000 km [8]. Beyond simple optical fibers, advancements in process technology have resulted in the scalable manufacture of fibers incorporating intricate microstructures and a myriad of materials [6]. Recently, the breadth

of compatible materials has been extended to soft thermoplastic elastomers [9], acting as an enabling technology for fiber-based sensors [15, 16] and energy harvesters [99]. However, the potential of thermal drawing as a platform for soft robotics has thus far remained untapped.

In this Chapter, we present soft robotic fibers with diameters as thin as 700 µm that can accurately accomplish extensive 3-dimensional motion driven by fiber-embedded tendons. Fabrication via thermal drawing enables direct incorporation of active elements in precise architectures within the thermoplastic-elastomer-clad fibers, including optical guides, metallic wires, and microfluidic channels, giving rise to a wide range of functionalities beyond mere actuation. The soft robotic fibers can perceive their environments and autonomously adapt to changes thereof, as well as probe electrical properties, and deliver fluids and mechanical tools to spatially distributed targets.

5.2 Design, fabrication, and actuation mechanism

Our fabrication and actuation concept is illustrated in Figure 5.1a. The thermal drawing process relies on the viscous flow of material under heat and tension to convert a macroscopic materials assembly, termed preform, into a long fiber. In the process, the cross-sectional design is maintained from the preform to the fiber and is merely uniformly scaled down — at ratios of 10 to 30 in this work. At the level of the macroscopic preform, complex geometrical features are readily realized using standard compression molding, such as holes that become microchannels in the fibers. We selected poly(styrene-b-(ethylene-co-butylene)-b-styrene), SEBS, as the supporting cladding material of the fibers, which is distinguished by its process-relevant rheological profile (Figure 1.3a), and its elastomeric properties in applications (100 %-modulus = 1.7 MPa, elongation at break 470 %, see Figure 1.4a). By extending the thermal drawing process with a feeding mechanism, inert 1-dimensional elements, such as optical guides or metallic wires, can also be integrated in the fiber. Their placement within the fiber architecture is dictated by specifically arranged holes in the preform. During the process, the holes shrink alongside the whole cross-sectional structure, allowing the surrounding material to capture the fed element within it and pulling it along.

Based on this materials and fabrication platform we explored a variety of different fiber designs (Figure 5.1b). However, they all share the structural feature that enables actuation in the fibers: three lumens, arranged at 120° angles, each hosting a tendon consisting of a nylon line or metallic wire with diameters of 70 to 200 µm. Note that the tendons can be incorporated during thermal drawing using the feeding mechanism for large required fiber lengths, or inserted in the lumens in post-processing for smaller sections. To assure free translation of the tendons within the lumens at minimum friction, we introduce ethanol as a lubricant. By fixing the tendons at the distal fiber end and concertedly pulling on them at the proximal end, the fibers bend in a controlled fashion with two degrees of freedom. We qualitatively demonstrate the range of bending angles and directions using a fiber of diameter 1.5 mm and length 80 mm (Figure 5.1c). Moreover, we illustrate the adaptability of the fibers, as well as their mechanical

compatibility with the human body, arising from the softness and deformability of SEBS, by having a robotic fiber of diameter 700 µm safely wrap around a finger (Figure 5.1d).

5.3 Peripheral control unit

Actuation of the soft robotic fibers is driven by three embedded tendons. To accurately control the bending angle and bending direction of the fibers, the three tendons are fixed at the distal end of the fibers and pulled by specific amounts. This translation as well as the interfacing with the diverse additional embedded functionalities are accomplished with the peripheral control unit. Its design can be separated into hardware and software. Both parts are shown in Figure 5.2.

On the hardware side, the proximal end of the robotic fiber is clamped in a dedicated vise. From the vise, the tendons are led into a distributor element, which contains three Teflon-coated channels, one for each tendon. The purpose of the distributor is to spatially separate the tendons, which are very close in the thin fibers and thus difficult to actuate individually. From the distributor, each tendon is fixed to the arm of a servo motor. The servo motors are fixed on rails and can thus be translated, allowing the tension of the tendons at the zero position to be controlled. The three servos are interfaced to a microcontroller, which allows the angle to be precisely set. The motion commands are sent to the microcontroller via a PC. Besides controlled translation of the tendons, the control unit also serves as an interface to additional functionalities in the fibers. For optical functionality, photoemitters and detectors are included, which allow optical guides from the fibers to be inserted. The control unit includes three differently colored LEDs (red, green, blue) as well as a photodarlington, each embedded into suitable electronic circuits and continuously addressed by the microcontroller. For electronic functionalities, the unit also features a wire terminal, into which individual thin wires can be inserted. The lines from the terminal can be connected to a dedicated electrometer for electrical characterization. Finally, fluidic functionality is supported by syringe tips that can be inserted in the microchannels of the fiber at the proximal end. On the other side, the syringe tips are connected to a syringe for manual injection and suction or a peristaltic pump for automized fluidic tasks. To analyze experiments in the aftermath, a camera is also connected to the control unit.

The actuation and additional functionalities are coordinated by the PC, which runs a custom graphical user interface. The program is written in Python 3 and includes the modules Numpy, Matplotlib, Serial, Tkinter, and OpenCV for multi-dimensional array operation, real-time plotting and visualization, communication with the microcontroller, providing a graphical user interface, and recording images and videos, respectively. The actuation controls are eased by the implementation of a kinematic model, which is discussed below. The movement of the robotic fiber can be instructed using different ways: (i) The absolute arm angles for each servo can directly be input. (ii) In addition to unique values, each servo can also be instructed to execute a servo angle ramp, where starting and end position as well as step size

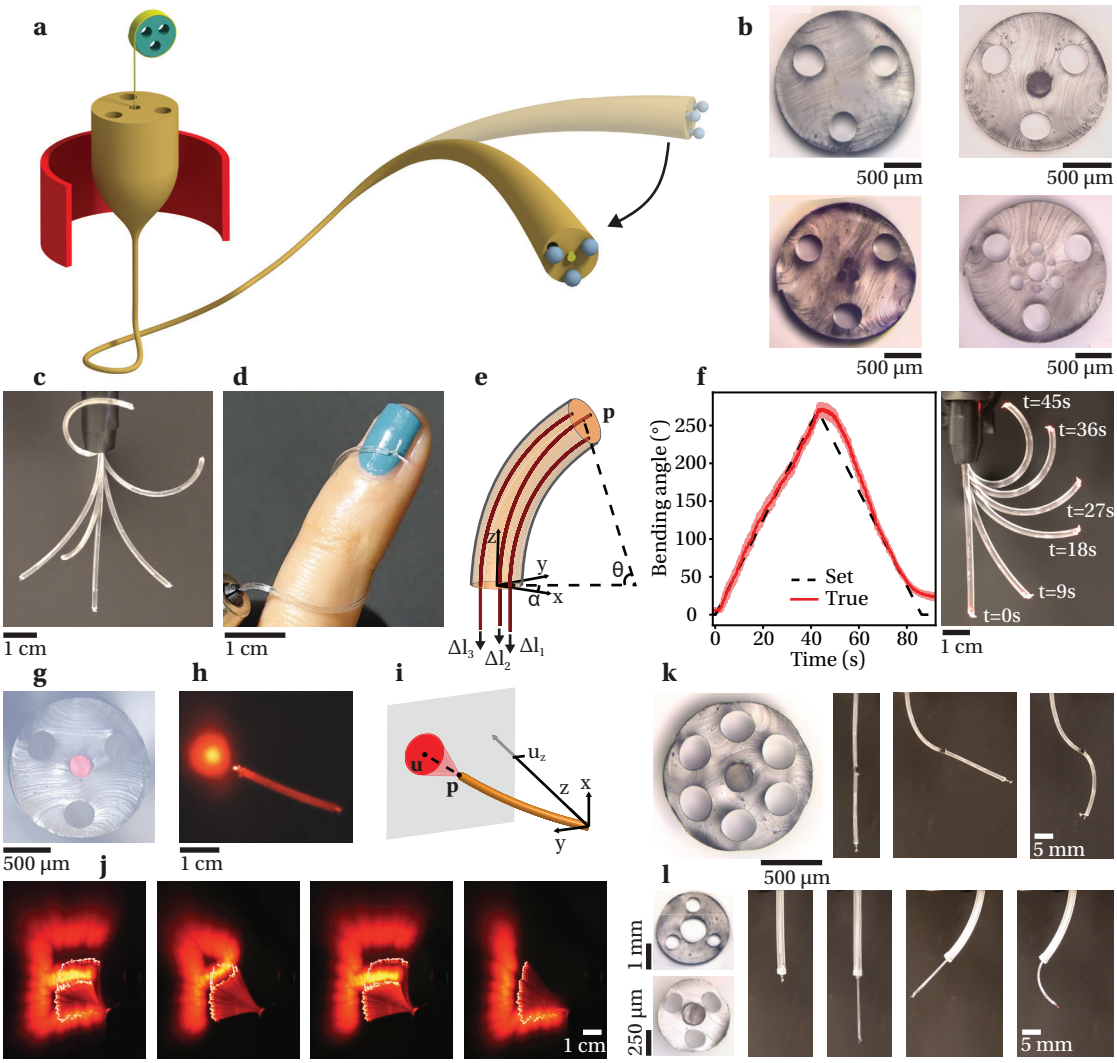

Figure 5.1 – Soft robotic fibers fabrication, structure, and actuation. a) Schematic of the fabrication technique and the actuation driven by integrated tendons. b) Optical micrographs of several produced fiber cross-sections. The SEBS fiber structure features three lumens to host the tendons and can integrate optical guides, metallic wires, or microchannels. c) Merged sequence of photographs of a soft robotic fiber, illustrating the range and complexity of motion. d) Photograph of a soft robotic fiber of diameter 700 µm that wraps around a finger through actuation. e) Schematic of the fiber configuration, parameterized by its length, bending angle θ and bending direction α. The configuration is set through the controlled displacement of the tendons Δl_i, and defines the end effector position **p**. f) Bending angle ramp with constant bending direction angle, shown as a comparison of set and true bending angle as well as a merged sequence of photographs. g) Optical microscope of the cross-section of a soft robotic fiber integrating a light guide that emits red light. h) Photograph of the robotic fiber emitting light out of the distal end onto a screen. i) Schematic of the light projection, parameterized by the center of the lit disk on the screen **u**. j) Merged sequence of photographs of predefined motion patterns executed by the soft robotic fiber. k) Optical micrograph of the cross-section and sequence of photographs of different configurations for a fiber integrating two sets of three tendons, where one set is terminated halfway along the length and one at the end point. l) Another strategy of high-degree-of-freedom motion, achieved by inserting a thinner robotic fiber within a larger.

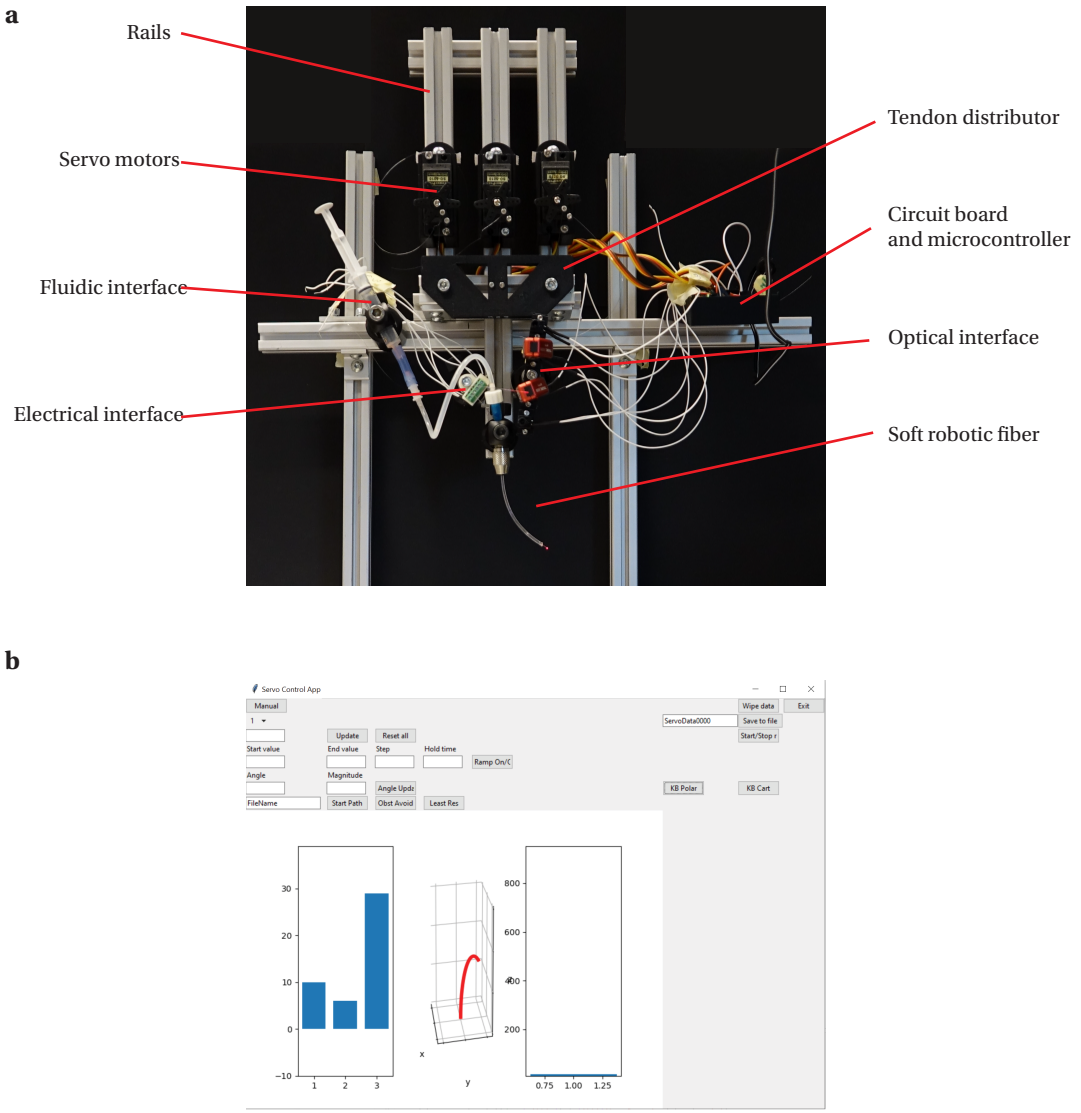

Figure 5.2 – Peripheral control unit. a) Experimental setup to control and interface with the soft robotic fibers. b) Screenshot of the graphical user interface.

and step time are set. (iii) The desired bending angle and bending direction of the robotic fiber can be input, which are automatically converted to servo angle instructions. (iv) With the keyboard direction buttons the fiber can be intuitively moved in the desired direction, based on cartesian or polar coordinate systems according to user preference. (v) Previously planned trajectories can also be executed. The trajectories are input as sequences of bending angle and bending direction in the form of a text file. Upon initiation, the program consecutively runs through the coordinates in the sequence, automatically enacting the planed trajectory. (vi) The fiber can also be controlled without specific user input. In this case, the proximity sensor signal is used as a feedback in a closed-loop controller. Depending on the implemented controller, such as on-off control using a threshold value, the fiber autonomously adjusts its configuration based on the measured signal.

Regardless of the chosen actuation control, the graphical user interface displays essential information of the system to the user in real-time. This includes a bar chart of the absolute servo arm angles, a 3-dimensional visualization of the current fiber configuration, and a bar chart of collected signals, such as photodarlington voltage in the proximity sensing device. Finally, the software also features the possibility of saving all collected data, including time, set servo angles, set fiber configurations, measured signals, and a synchronized video stream from the camera.

5.4 Kinematic model and motion control

At the heart of the controls system lies our kinematic model, formulated upon the constant-curvature approximation. With this framework, the high dimensionality of the soft robot is reduced to a 3-dimensional configuration space, parameterized by the fiber length l, bending angle θ, and direction angle α (Figure 5.1e). In the kinematic model, the four operation spaces are decomposed and sequentially mapped: (i) the actuator space specific to the setup, (ii) the joint space with the variables tendon displacements Δl_i, (iii) the configuration space, and finally (iv) the task space, described by the 3-dimensional coordinates of the end effector $\mathbf{p}$. The model is presented in its inverse form, as in most application we aim at calculating the inputs to achieve a set end effector position.

The first mapping consists of relating the task space, parameterized by the end effector coordinates $\mathbf{p} = (p_x, p_y, p_z)$, to the configuration space defined by the parameters fiber length l, bending angle θ, and bending direction α, as defined in Figure 5.3a. It can be expressed as [169]:

$$\alpha = \arctan\left(\frac{p_y}{p_x}\right) \tag{5.1}$$

$$\theta = \arccos\left(\frac{1 - \frac{p_y^2}{p_z \cdot \sin^2(\alpha)}}{\frac{p_y^2}{p_z \cdot \sin^2(\alpha)} + 1}\right) \tag{5.2}$$

The second mapping relates the configuration space to the joint space, parameterized by the displacements of the three tendons Δl_i with $i = 1,2,3$. As a robot-dependent mapping, the structural parameters eccentricity e and tendon angle ϕ_i, shown in Figure 5.3b, must be included [170]:

$$\Delta l_i = e \cdot \theta \cdot \cos\left(\alpha - \phi_i\right) \tag{5.3}$$

In practical experiments, we extended this ideal case by two terms. First, we included an additional term to avoid tendon slacking, which causes a compression of the fiber and thus a slight shortening of length, but does not alter the bending angle or bending direction. Second,

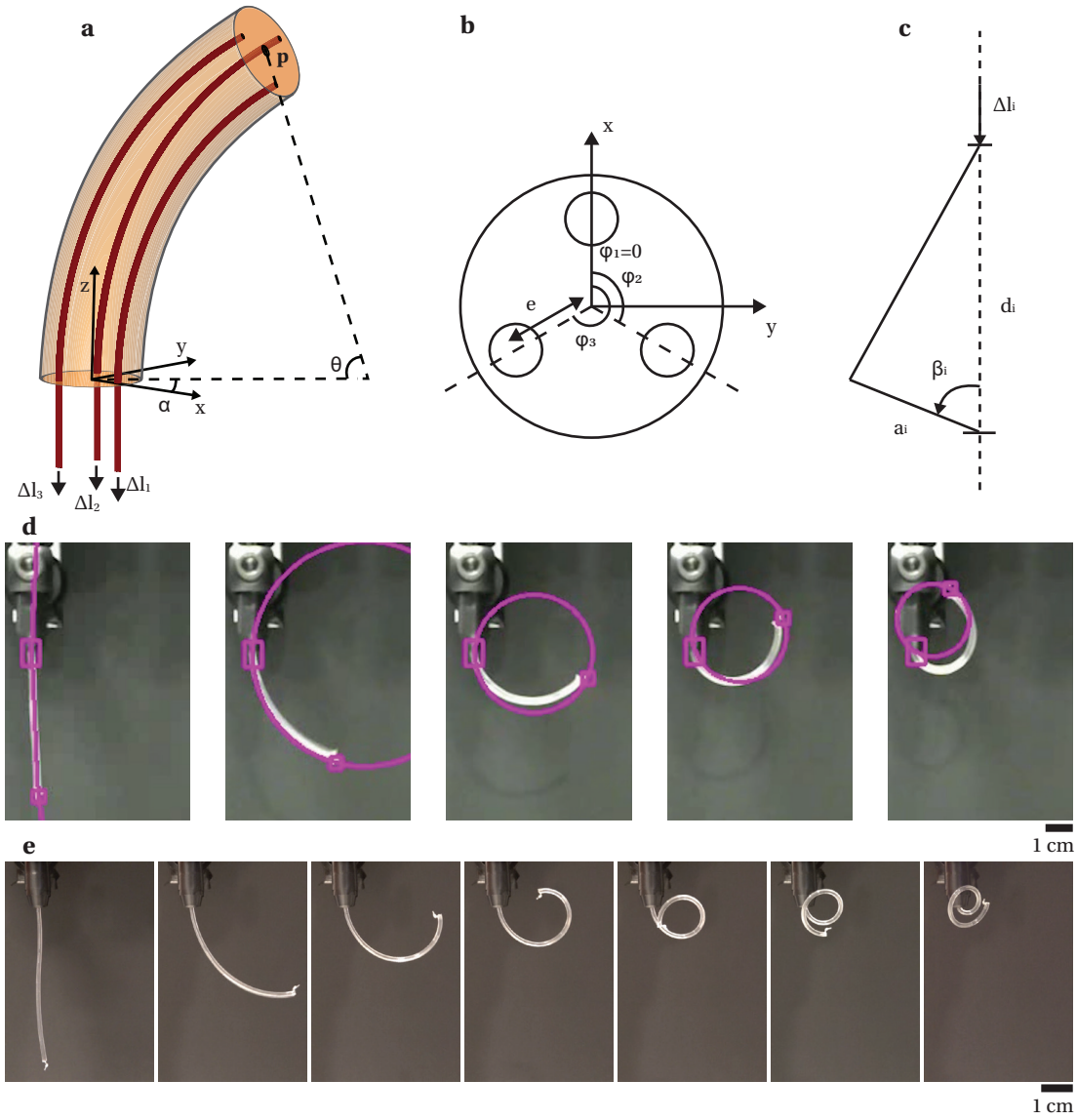

Figure 5.3 – Kinematic model and motion analysis. a) Schematic outlining the 3-dimensional bending of the fiber. The end effector coordinates **p** depend on the bending angle θ and bending direction α. The configuration of the fiber is set by controlled displacements of the tendons Δl_i at the proximal end. b) Schematic of the fiber cross-section. How much each tendon must be pulled depends on the structural parameters of the fiber, including the eccentricity e. The bending direction α is indicated to emphasize that the tendon displacements depend on their placement in the fiber relative to the bending direction. c) Schematic to outline the relationship between tendon displacement and set servo arm angle β_i through the setup parameters arm length a_i and servo distance from tendon distributor d_i. d) Sequence of images of the soft robotic fiber as the bending angle is continuously increased. The two extremities of the soft robotic fiber are selected as objects that are tracked throughout the experimental video. A circle is fitted based on the coordinates of the two points. As shown, it corresponds to the curvature of the fiber. e) Additional curvature ramp with a maximum bending angle of 540°.

we added a correction factor f_i for each tendon to account for slightly different zero positions during setup. The correction factor was obtained through a one-angle visual calibration,

typically at a bending angle of 90°.

$$\Delta l_i = f_i \cdot \left(e \cdot \theta \cdot \cos\left(\alpha - \phi_i\right) + e \cdot \theta\right) \tag{5.4}$$

The third and final mapping connects the joint space to the actuator space, which depends on the setup geometrical parameters servo arm length a_i and servo distance d_i, and yields the servo arm angle β_i, shown in Figure 5.3c:

$$\beta_i = \arccos\left(\frac{a_i^2 + d_i^2 - \left(l_{i,0} + \Delta l_i\right)^2}{2 \cdot a_i \cdot d_i}\right) \tag{5.5}$$

where $l_{i,0}$ is the initial length of the tendon segment between the distributor element and the point on the servo arm where the tendon is fixed. It depends on the initial servo arm angle setting:

$$l_{i,0} = \sqrt{a_i^2 + d_i^2 - 2 \cdot \cos\left(\beta\right) \cdot a_i \cdot d_i} \tag{5.6}$$

With these three mappings, the coordinates of the end effector are converted to the direct inputs of the peripheral control units in the form of the arm angles of the three servos. We firstly validate our inverse kinematics in a 1-dimensional experiment, where a bending angle sequence at constant bending direction is input into the system. In parallel, we capture the true bending angle with a camera and computer vision. As shown in Figure 5.1f, the soft robotic fiber follows the set bending angle ramp closely. Based on the visual analysis, we also find that the constant-curvature approximation holds (Figure 5.3d). A hysteresis effect is observed on the return path, which is a common occurrence in soft systems due to the material's viscoelastic nature. The highest deviation between set and true bending angle is observed close to the initial configuration, where the bending angle is zero and the tension of the tendons is at a minimum. Note that in this experiment, we limited the bending angle to a maximum of 270°, which we deem beyond requirements of most applications, although our robotic fibers can bend to significantly larger extents, as high as 540° (Figure 5.3e).

Next, we validate our controls in two dimensions by varying the bending direction in addition to the bending angle. We employ a soft robotic fiber equipped with an optical guide at its core (Figure 5.1g) and aim to deliver light to spatially predefined areas. Light from a source connected at the proximal end is emitted out of the distal end onto a screen (Figure 5.1h). Thus, the inverse kinematics are extended by an additional level consisting of the coordinates of the center of the light spot **u** (Figure 5.1i). In the experiment, we compile a sequence of **u** coordinates into a script similar to a G-code, which is commonly employed for the controls of CNC machines or 3-D printers. The list is input into the system in the form of a text file, upon which the robotic fiber automatically executes the trajectories, successfully tracing the shape of predefined letters (Figure 5.1j). The shown images are created by superimposing the frames of a video of the experiment by areas of highest intensity. Note that the small bright spot, visible besides the light projected onto the screen, is caused by the scattering interface at

the light guide's emitting end.

In a concluding remark regarding motion control, we present two strategies for increasing the degrees of freedom, currently limited to bending about two axes in the basic fiber design. In the first approach, the cross-sectional structure is altered to include six rather than three lumens, allowing two sets of three tendons to be distributed in the structure (Figure 5.1k). By terminating the first set of tendons halfway along the length and the second at the fiber end, the fiber is essentially separated in two segments that can each be separately actuated. In the second approach, a thinner basic robotic fiber is introduced within a larger robotic fiber featuring a large lumen at its center (Figure 5.1l). In addition to decoupled bending of both fibers, the thinner fiber can be advanced and retracted within the larger fiber, adding another translational degree of freedom. These examples illustrate the complexity of motion that can be achieved as well as the modularity of our soft robotic fibers.

5.5 Proximity sensing with soft robotic fibers

An important ability in robots is the perception of their surroundings, particularly so in medical robots where the environments are fragile and dynamic. We seek to accomplish exteroception in our soft robotic fibers through optical displacement sensing. We introduce three parallel optical guides in the core of the fiber, which are decoupled from one another (Figure 5.4a). The sensor configuration consists of one guide connected to a light source and one to a photodetector at the proximal end, acting as transmitting and receiving lines (Figure 5.4b). The intensity of light reflected at an obstructing surface depends sensitively on the distance and decreases monotonically beyond a peak at approximately 0.5 mm (Figure 5.4c). Based on a spectroscopic analysis (Figure 5.5a, b), we found an optimum in measurement sensitivity and range at a wavelength of approximately 650 nm, which corresponds to one of the attenuation minima of PMMA light guides. At this wavelength, distances can be measured at submillimeter resolution up to 18 mm. In subsequent experiments, we employed an LED with peak wavelength 645 nm and a photodarlington to improve the practicality of the device and increase the signal collection and analysis rate. We also tested the sensor in deionized water and water with an absorbing agent (Figure 5.5e, d). Besides a shift of the intensity-distance curve, which can be resolved by recalibration upon operation in a medium of different refractive index, the sensor performance remains unchanged.

We introduce the measure of proximity as an exteroceptive feedback to close the control loop, setting the stage for autonomous movement and obstacle avoidance. In a first experiment, we implement an on–off algorithm whereby the bending angle is increased when a threshold value of reflected intensity is exceeded due to near-impact proximity of an obstacle, and reduced again when the condition is not met. As shown in Figure 5.4d, stages 1-4, the soft robotic fiber adjusts its configuration according to the continuous measure of reflected intensity, successfully avoiding contact, as well as returning to its initial position when the disturbance is removed. Note that the oscillation close to the threshold could be resolved through more

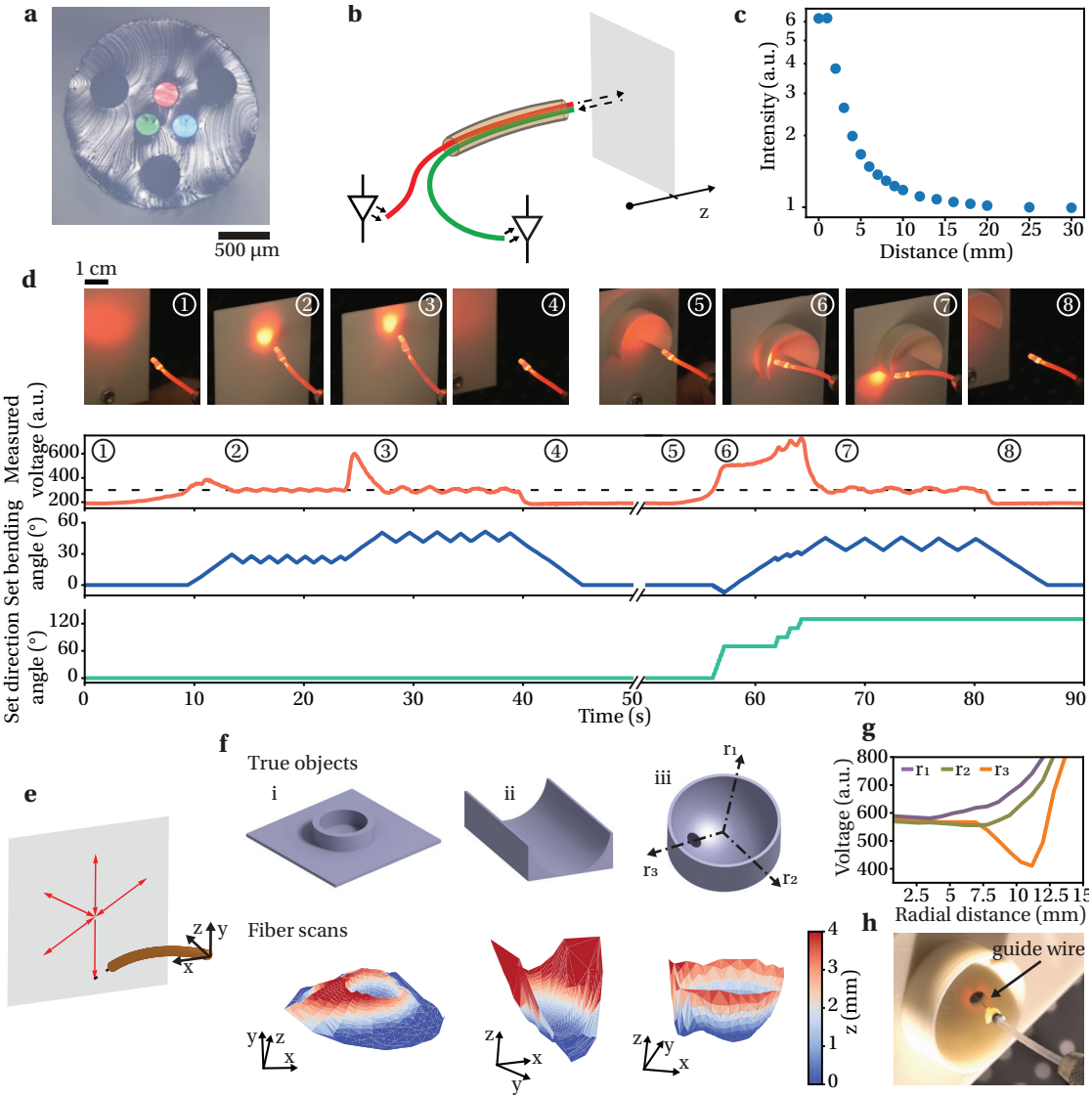

Figure 5.4 – Proximity sensing with soft robotic fibers. a) Optical micrograph of the cross-section of a fiber integrating three optical guides, each emitting a differently colored light. b) Schematic of the working principle of the proximity sensing. c) Intensity of received light as a function of distance to the reflecting obstacle. d) The continuously measured intensity is used as a feedback signal to control the configuration of the robotic fiber. The experiment is shown by a sequence of photographs, as well as a plot of the measured photodarlington voltage and set bending angle and direction as function of experiment time. The encircled numbers relate the photographs to the corresponding times in the plot. e) Schematic of the fiber motion pattern to scan over the surface of an unknown object. f) Comparison between the true objects, shown as 3-dimensional models that are printed, and the reconstructions obtained trough the proximity signals and fiber configurations during the scan. The fiber scan reconstructions are color-coded by the z-coordinate, defined in panel (e). g) Measured proximity signals for three exemplary radial scan orientations as indicated on object iii in panel (f). h) Photograph of the fiber facing the hole in the object, which was autonomously executed based on collected proximity signals. A metallic guide wires is manually advanced through one of the fiber lumens right into the targeted hole.

advanced controllers, such as a PID. In a second test, we increase the complexity of the task by introducing an obstacle that cannot be avoided through 1-dimensional bending. We take advantage of the omnidirectional bending capability of our robotic fibers and extend the algorithm by an additional condition: When an increase in bending angle causes a decrease in proximity rather than the expected increase, the step is reversed threefold and the bending direction is altered. Also in this case, the robotic fiber could autonomously find a configuration to avoid an impact with the approaching obstacle (Figure 5.4d, stages 5-8).

Next, we show that the soft robotic fibers can also act as imaging devices, where the proximity signals are used in conjunction with the known fiber configurations to reconstruct the 3-dimensional spatial surroundings. To obtain a large number of sample points, we plan a radial scanning sequence that is automatically executed by the fiber (Figure 5.4e). For each fiber position, we implement the measure of distance in the forward kinematic model to compute the spatial coordinates of a point on the obstructing surface.

This is done by recording the photodarlington voltages for specific distances of a reflecting white surface to the tip of the robotic fiber. An example of a calibration curve is shown in Figure 5.5e.

We find that the relationship between the measured voltage V and the distance d can be best described using a function of the form:

$$d = a_0 + \frac{a_1}{V} + \frac{a_2}{V^2} + \frac{a_3}{V^3} \tag{5.7}$$

The parameters a_i, $i = 0,1,2,3$ are found by fitting the function to the calibration data. Based on this calibration curve, a distance can be directly calculated from a measured photodarlington voltage signal.

Next, we must determine the kinematic relationship between, on one hand, the coordinates $\mathbf{u}$ of the targeted point on the reflecting surface, and, on the other hand, the measured distance and set fiber configuration. We first derive in two dimensions using the schematic shown in Figure 5.5f:

$$\mathbf{u} = \begin{bmatrix} \frac{l}{\theta} \cdot (l - \cos\theta) + \sin\theta \cdot d \\ 0 \\ \frac{l}{\theta} \cdot \sin\theta + \cos\theta \cdot d \end{bmatrix} \tag{5.8}$$

We extend the expression to three dimensions by applying the rotation matrix around the

z-axis by the bending direction angle:

$$\begin{aligned}\mathbf{u} &= \begin{bmatrix} \cos\alpha & -\sin\alpha & 0 \\ \sin\alpha & \cos\alpha & 0 \\ 0 & 0 & 1 \end{bmatrix} \cdot \begin{bmatrix} \frac{l}{\theta}\cdot(l-\cos\theta)+\sin\theta\cdot d \\ 0 \\ \frac{l}{\theta}\cdot\sin\theta+\cos\theta\cdot d \end{bmatrix} \\ &= \begin{bmatrix} \cos\alpha\cdot\left(\frac{l}{\theta}\cdot(1-\cos\theta)+\sin\theta\cdot d\right) \\ \sin\alpha\cdot\left(\frac{l}{\theta}\cdot(1-\cos\theta)+\sin\theta\cdot d\right) \\ \frac{l}{\theta}\cdot\sin\theta+\cos\theta\cdot d \end{bmatrix}\end{aligned} \tag{5.9}$$

Using this expression, every set of configuration angles and distance, which is determined using the intensity of reflected light and the calibration curve, yields the coordinates of a point on the surface. Finally, all the points from the scan are plotted, resulting in the 3-dimensional reconstruction.

To test our 3-dimensional mapping concept, we print three objects with defined geometries and initiate the scanning protocol upon them (photographs of all objects are shown in Figure 5.5g). As shown in Figure 5.4f, the computed representations based on the fiber scans closely match the true shapes. The spatial resolution of recorded points on the surface is limited by the area defined by the overlapping acceptance cones of the two light guides, which is why sharp features of the objects appear washed out. The resolution could be improved through light guides with smaller numerical apertures as well as different numbers and arrangements of emitting and receiving guides. Additionally, a source of error is the discrepancy of set fiber configuration to true configuration. Nonetheless, with our first-generation device, particular areas of interests in the surroundings are readily identified and can be used as reference points for autonomous task completion. We demonstrate this capability with the cup-shaped object, which features a hole. The intensity values collected for radial scans in three orientations are shown in Figure 5.4g. In contrast to the other two orientations, the intensity profile obtained for the path crossing over the hole exhibits a distinctive minimum. Once the scan is completed, the robotic fiber automatically moves to the position of minimum intensity, as it was instructed to do before the experiment. The resulting fiber configuration provides an ideal access for subsequent navigation and manipulation, which we illustrate by manually advancing a guide wire through one of the lumens of the fiber directly into the targeted opening (Figure 5.4h). Note that in this scheme of identifying and implementing an optimum configuration, unlike the imaging concept, the fiber simply recreates a previous configuration with specific settings and it thus irrelevant how closely the true configuration matches the set position.

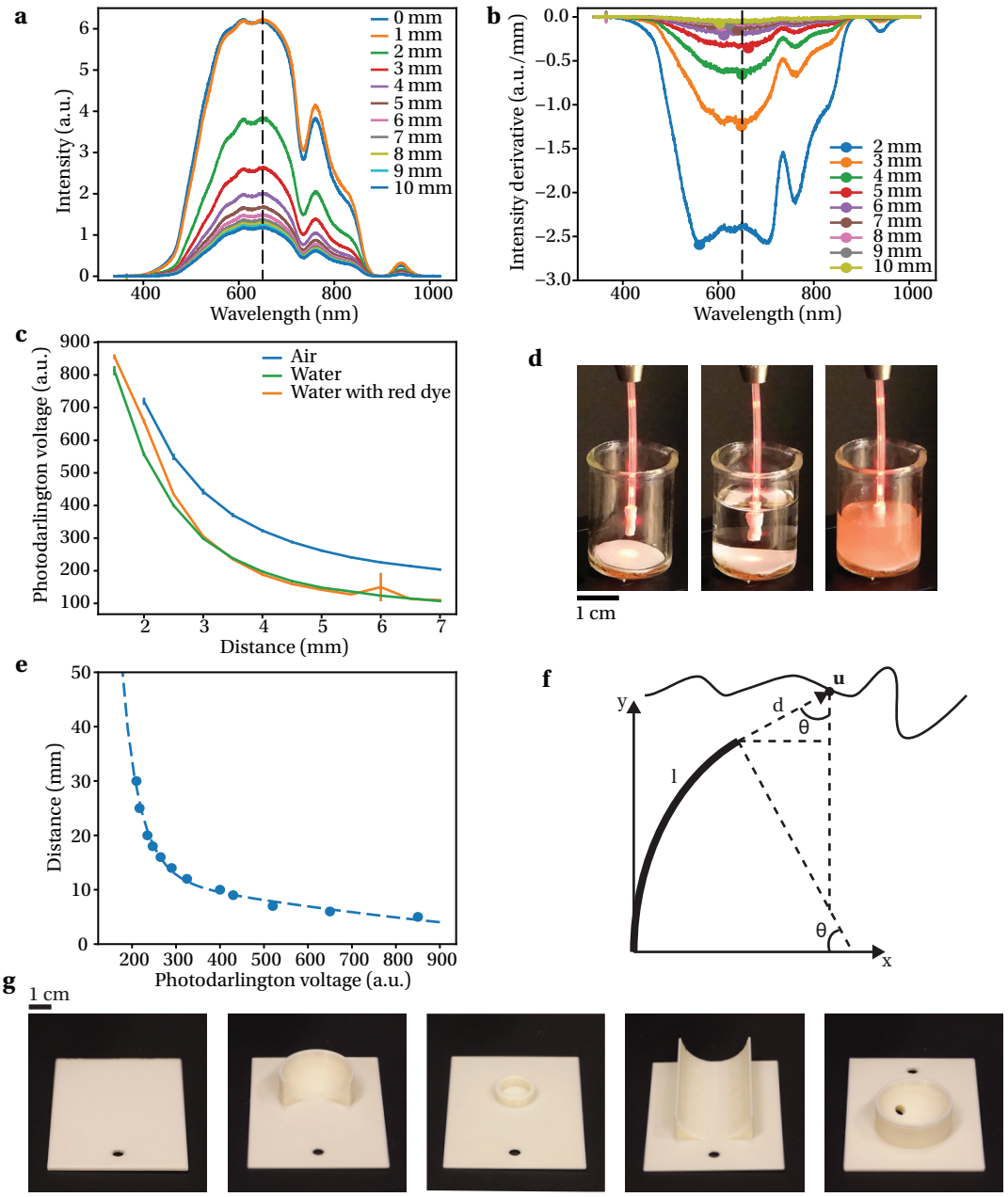

Figure 5.5 – Additional analysis of proximity sensor. a) Spectrum of the reflected light for different distances of the fiber tip to the reflecting surface. The wavelength 650 nm is indicated as a dashed line. b) Spectrum of derivative of intensity with respect to distance for different distances. The negative peak for each curve is indicated by a solid marker. c) A reflective surface is translated respective to the fiber tip in different media. The shown voltage of the photodarlington corresponds to the reflected light intensity from a red LED. d) Photograph of the three different media. e) Calibration curve obtained by fitting a function to the data obtained from a calibration experiment. f) Schematic outlining the relevant geometrical parameters to calculate the coordinates **u** on the surface of an object from the measured distance d and fiber bending angle θ. g) Photographs of all 3-dimensionally printed objects employed in the experiments of the proximity sensor.

5.6 Electrical probing and fluidic delivery

In addition to optical guides, the soft robotic fibers can also host metallic wires to electrically stimulate and record spatially distributed targets. As shown in Figure 5.6a, we integrate three super-elastic Nitinol wires of diameter 76 µm at the center of the fiber. The wires are connected to an electrometer on the proximal end and left exposed at the distal end of the fiber. Thus, if the fiber tip comes in contact with a conducting surface, the circuit between two of the three wires is closed and samples can be electrically characterized through current measurements. To test this functionality, we aim at electrically probing two different conductive hydrogels with admittivities, 1.1 $mS.m^{-1}$ and 0.3 $mS.m^{-1}$. Rather than relying on predetermined trajectories, we demonstrate our manual control technique, where the movement of the robotic fiber is instructed directly by a user via the direction keys of the computer keyboard. As illustrated in Figure 5.6b, the fiber readily bends from the initial configuration towards any desired point on the samples. Moreover, sufficient force can be applied to create a stable electrical contact, as underlined by the current that is measured in parallel. Indeed, the measured signal corresponds to the conductivity of the sample.

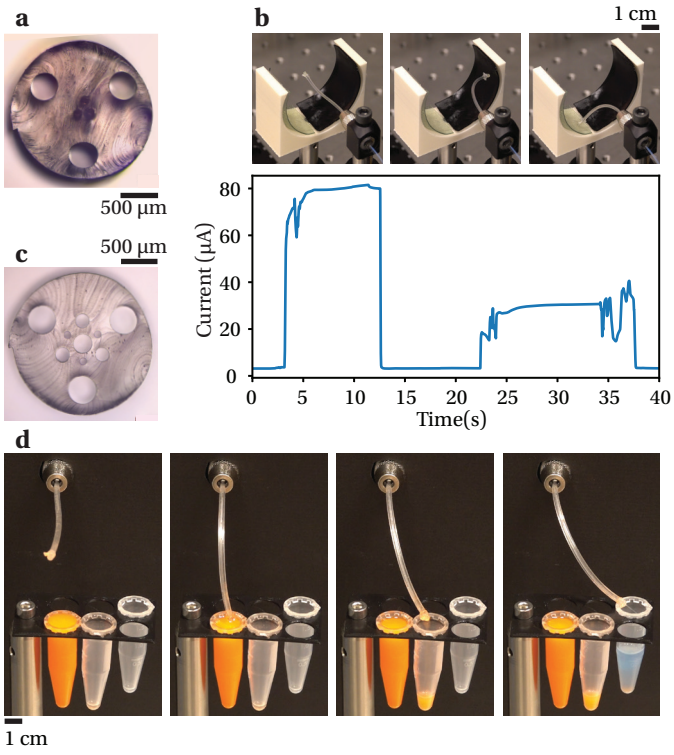

Figure 5.6 – Electrical and fluidic functionality in soft robotic fibers. a) Optical micrograph of the cross-section of a fiber integrating three metallic wires. b) Sequence of photographs and measured current during an electrical probing experiment. The robotic fiber comes consecutively in contact with two different samples, thus assessing the electrical properties. c) Optical micrograph of the cross-section of a fiber integrating seven microchannels at its center. d) Sequence of photographs of the fluidic experiment. The robotic fiber sucks fluid out of the first vial, and pumps it into a second vial. Subsequently, it pumps a different liquid into a third vial.

As a final functionality, we incorporate several fluidic channels in the soft robotic fibers that can be addressed individually. Through the use of pumps connected at the proximal end, the channels can serve as tools for the targeted delivery or suction of fluids. We demonstrate this capability with a soft robotic fiber that integrates seven differently sized channels (Figure 5.6c). In the fluidic experiment shown in Figure 5.6d, we rely once again on the manual controls to move the robotic fiber and accurately address several spatially distributed vials. In a first step, we use one of the channels to suck fluid out of one of the vials and deliver it to the vial next to it. Subsequently, with one of the other channels, we fill a third vial with a separate fluid to highlight the multiplexing capability.

5.7 Conclusion

The thermally drawn thermoplastic elastomer-based fibers set the stage for soft robotic devices with extreme aspect ratios and integrating multiple materials. Complex and accurate motion is achieved by a tendon-driven mechanism and additional modular functionalities are evoked by embedded light guides, electrical wires, or fluidic channels. The soft robotic fibers are particularly promising in minimally invasive procedures, where they can perceive, image, and autonomously adapt according to their spatial environments, as well as probe electric properties and deliver fluids and tools to spatially distributed targets.

5.8 Experimental section

Soft robotic fiber fabrication and preparation

To fabricate the preform, granules of the cladding material poly(styrene-b-(ethylene-co-butylene)-b-styrene) (SEBS Kraton), were filled into custom steel molds, which featured the desired outer shape as well as interior mold cores. The material was compression-molded at 0.5 bar, 180 °C for 6 h. Next, the preforms were thermally drawn into fibers using a custom draw tower at a set middle-zone-temperature of 200 °C and at a feed speed of 1 $mm.min^{-1}$ and take-up speeds ranging from 100 to 900 $mm.min^{-1}$, resulting in diameter scale-down ratios of 10 to 30. For fibers featuring additional functional elements such as optical guides, a feeding mechanism was employed as an extension to the thermal drawing process. Before starting the process, the 1-dimensional elements were introduced in designated holes within the preform. The significant decrease in size of the cross-section during the process, led to the fed elements being caught within the narrowing holes by the flowing cladding material and being continuously unspooled. Fed elements included tendons (bend-and-stay multipurpose 304 stainless steel wires, super-elastic nitinol wire, or clear nylon line, McMaster-Carr), optical guides (optical grade plastic optical fiber unjacketed, Edmund Optics), electric wires (bend-and-stay multipurpose 304 stainless steel wires, super-elastic nitinol wire, McMaster-Carr), and Teflon tubing (high-temperature tube sleeving, McMaster-Carr). The fabricated fibers were assessed using optical microscopy (microscope, Leica). In fiber post-processing, the

fibers were first cut into suitable segment lengths. The tendons and other functional elements were exposed at the ends through a solvent (toluene, Sigma-Aldrich) or mechanical treatment. On one end, the tendons were fixed by tying knots or applying epoxy glue. On the other end, the tendons and other functional elements were interfaced with the peripheral control unit. Finally, a drop of ethanol was applied on the tip of the fiber, where it was sucked into the lumens of the tendons by capillary effect, acting as a lubricant during actuation.

Motion characterization

The soft robotic fibers were fixed and actuated with the peripheral control unit. For the 1-dimensional bending, a camera (C270, Logitech) was orientated perpendicularly to the bending direction of the fiber. During the bending angle ramp, the time, set bending angle, and camera images were continuously recorded. In post-processing, the video feed was analyzed using computer vision (OpenCV in Python), where the coordinates of the two fiber extremities were extracted, yielding the fiber's true bending angle. To characterize the motion in 2 dimensions, a soft robotic fiber with a light guide at its center was employed, where the light guide was connected to a red light-emitting diode (IF E96E, Industrial Fiber Optics) at the proximal end. Light emitted out of the distal end of the light guide was projected onto a screen. The experiment, consisting of executing planed trajectories, was recorded by a camera (RX100, Canon). The cumulative light path was visualized in post-processing using frame blending by maximum intensity in video editing software (Premiere Pro, Adobe).

Proximity sensor characterization

A soft robotic fiber featuring three light guides at its center was used for proximity sensing experiments. In the spectroscopic analysis, one light guide was connected to a white light source (HL-2000, Ocean Optics) and another light guide to a photodetector (USB2000+VIS-NIR-ES, Ocean Optics). A white surface orthogonal to the fiber was displaced in a controlled fashion and the spectrum of reflected light recorded at every increment at a constant integration time of 1000 ms. In subsequent experiments, a practical light source (IF E96E, Industrial Fiber Optics) and photodetector (IF D93, Industrial Fiber Optics) were employed. For testing different media, the fiber tip was submersed in a beaker, which was displaced in a direction parallel to the fiber using a translation stage. In the obstacle avoidance test, 3-dimensionally printed objects of white polylactic acid were displaced relative to the fiber and the measured intensity signal and set fiber configuration were continuously recorded. For the fiber scanning experiment, 3-dimensionally printed objects were kept at a constant distance while the fiber moved atop them. The scan involved a bending angle step size of 2° and range of 2° - 34° and a bending direction step size of 10° and range of 0° - 360°, resulting in a total 612 points that can be used for the reconstruction of the shape. For the experiment involving the guide wire, a fiber was used where one of the light guides was mechanically extracted and replaced by a stiff metallic wire (spring-back multipurpose 304 stainless steel wire, McMaster-Carr). Once the scan procedure was completed and the fiber automatically moved to the desired position

angled at the targeted hole, the steel wire was manually moved forward, penetrating the hole.

Electrical probing test

The electrical probing experiment was performed using a soft robotic fiber featuring three metallic electrodes at its center (super-elastic nitinol wire, McMaster-Carr). The wires were mechanically exposed at both extremities. On the proximal end, the wires were interfaced to an electrometer (HF2LI lock-in amplifier, Zurich Instruments), where two wires were connected conjointly at the first pole and the third wire at the second pole. The current was continuously recorded under an electrical stimulation of frequency 100 kHz and amplitude 1 V, while the fiber motion was conducted using the keyboard control. The tested samples consisted of conductive hydrogels composed of gelatine-glycerol, where the conductivity was tuned by a controlled amount of polypyrrole resulting in two types of samples with admittivities 1.1 $mS.m^{-1}$ and 0.3 $mS.m^{-1}$.

Microfluidic channels test

The fluidic experiment was performed using a soft robotic fiber featuring seven channels distributed in the cross-section. On the proximal end, the two of the channels were connected by inserting syringe tips, leading through tubing to syringes. Water with differently colored dyes was used as an illustrative fluid. The fiber motion was conducted using the keyboard control, and fluid suction and delivery was achieved by manually operating the syringes.

Conclusion

In this Thesis, the fabrication of soft multi-material fibers with the thermal drawing technique was studied. Based on this materials and processing platform, several mechanical sensors and actuators in fiber form were developed, which featured innovative materials, structural designs, and transduction mechanisms. Indeed, the soft devices could effectively solve a diverse set of tasks in biomedical applications and human-machine interaction.

The material class of thermoplastic elastomers constitutes the foundation of the work, based on which the soft fiber-based devices are developed. It was found that several thermoplastic elastomers exhibit the necessary rheological profile for the thermal drawing technique, more specifically the predominantly viscous rather than elastic thermomechanical behavior. In contrast to glasses and thermoplastics, which were until recently the only process-compatible material groups, thermoplastic elastomers can reversibly deform to large extents (100s of percent of strain) under low loads (on the order of kPa to MPa). Most importantly, they can be co-processed with other materials that have particular properties of their own. The focus was set on electrical materials in particular, including conductive polymer composites as well as solid and liquid metals. In terms of processing, composites retain their structural integrity during the drawing and can be placed on surfaces, whereas both solid and liquid metals must be fully enclosed by viscous materials. As for electrical properties, it was found that polymer composites have higher resistivities, on the order of 10 Ω.m, and feature pronounced piezoresistive behaviors that can, at extreme strain levels, lead to the irreversible loss of conduction. Solid and liquid metals with resistivities on the order of 10^{-7} Ω.m, however, are conductive enough to guide currents and voltages at high frequencies where wave phenomena are observed. Moreover, liquid metals follow faithfully and reversibly all deformations applied to the enclosing material. In conclusion, diverse multi-material assemblies of thermoplastic elastomers and functional materials can be realized within fibers with the thermal drawing process.

Several concepts of mechanical sensing and actuation were explored by relying on such multi-material fibers. The functionalities were evoked by leveraging the various materials' properties, their arrangement in fiber-internal structures, as well as the interfacing with peripheral devices that could interact with the fibers in specific ways. In terms of sensing, a special emphasis was put on the amount and the quality of information that could be extracted from the fibers. Since the fibers act as distributed sensors, adapted schemes were developed

to obtain information not only about the presence and intensity of an applied stimulation, as is the case in typical 0-dimensional sensors, but also about its type and location along the fiber, as well as the distinction between multiple simultaneously applied stimuli. While this is a significant challenge that often necessitates the exclusive selection of one mode of deformation to be measured, or the loss of one piece of information in favor of another, it also represents an opportunity because a single fiber-based sensor with few contact points can provide an immense wealth of information. When considering actuation, the mechanism triggering the movement must be adapted to the high-aspect-ratio nature of the fibers. Special emphasis was put here on the interaction of integrated actuation and sensing, which converts the fibers to capable robots when suitable control schemes are employed.

In the following, we summarize the specific fiber-based devices that were developed:

Pressure-sensing fibers. The fibers integrate an asymmetric elastomer architecture that features several electrodes separated by an air gap. Compressive loads on the meter-long fibers result in the selective contacting of the electrodes within the deformed fiber structure, triggering pronounced electrical signals at distinct pressure levels. Thanks to advanced mechanical analysis, involving a hyperelastic material model and finite-element analysis, the fiber microstructure is tailored to respond in a predictable and reversible fashion to different pressure ranges and locations. This developed pressure-sensing concept enables the facile functionalization of large surfaces, demonstrated by a fiber-augmented gymnastic mat for the monitoring of human body position, posture, and motion.

Stretchable nanocomposite fibers. A polymer nanocomposite is engineered based on the rheological, mechanical, and electrical requirements originating from the thermal drawing technique as well as application in electromechanical sensing. Embedded in a thermoplastic elastomer cladding, the resulting nanocomposite fibers are found to be soft and stretchable, as well as electrically conductive, a property that can be tuned by the processing temperature when the fiber incorporates a process-supporting spine. Along with the intricate multimaterial cross-sectional designs, the programmable resistivity and linked piezoresistivity make the thermally drawn nanocomposite fibers a versatile platform for mechanical sensors. This potential is demonstrated with several fiber-based devices, which are each targeted at a specific mode of mechanical stimulation and rely on a different sensing scheme. They include a robotic fiber with an integrated bending mechanism that is monitored with a piezoresistive feedback signal, a pressure sensing fiber based on a variable path length of the electrical current, and a stretch sensing fiber based on measures of capacitance.

Transmission line fibers. The elastomeric fibers integrate specifically arranged liquid metal conductors and have the length and cross-sectional integrity necessary to guide signals at radio frequencies, enabling interrogation by electrical time-domain reflectometry. The reflected electrical waves, triggered by multimodal deformations of the fiber structure, yield a large amount of information about the applied stimulation. This unprecedented physical mechanism enables multiplexed measurements of the mode, magnitude, and position of

multiple simultaneous pressing and stretching events. By integrating a single soft transmission line with a single interface port into a larger fabric, the technique can be used to create an electronic textile that can decipher convoluted mechanical stimulation.

Soft robotic fibers. Both actuation and sensing schemes are combined, resulting in robotic fibers that can accurately accomplish extensive 3-dimensional motion driven by fiber-embedded tendons. Additional modular functionalities are evoked by embedded light guides, electrical wires, or fluidic channels. The soft robotic fibers can perceive, image, and autonomously react according to their spatial environments, as well as probe electrical properties and deliver fluids and tools to spatially distributed targets.

As was shown in these works, the use of soft material in functional fibers does indeed enable a wide range of methods for sensing and actuation, most of which would not have been possible with hard materials. Additionally, as demonstrated by the various prototypes, the soft fibers are ideally suited to safely interact with the human body, opening the door to numerous applications in the biomedical domain and human-machine interactions. However, the concepts developed in this Thesis must be optimized according to the targeted application and some bottlenecks remain to resolved. First, regarding the manufacturing, the soft materials can still not be processed at the scale of hard materials, neither in terms of minimum fiber diameter nor maximum length from one draw. However, thermoplastic elastomers provide an opportunity to lessen this inferiority because the rheological properties can be tuned by polymer synthesis techniques, for instance by altering the ratio of hard to soft segments or the polymer chain lengths. Likewise, the critical parameters related to the viscous flow of the composites were identified, which can be used as waypoints for changes in formulation and preparation of nanocomposites specifically for the thermal drawing process. Additionally, the process technology is far from optimized and detailed heat transfer and flow mechanics analyses should result in improved yields. Functional fibers with diameters and lengths comparable to standard fibers employed in the textile industry would ease the augmentation of textiles. Secondly, considering the design and mechanism, it was found that it is difficult to realize a one-size-fits-all solution and generally concessions must be made in terms of the stimulation that is to be captured or generated. However, the design freedom is immense and specialized fibers can be combined if additional complexity is desired. An ever-present drawback of the soft materials in deformable devices was their viscoelastic nature, which introduced a hindering hysteresis behavior in sensing and actuation applications. However, it can often be circumvented by changes to the design, by limiting the range of stimulation in applications, or, as was recently shown [81], the use of advanced computational methods, such as machine learning. Finally, regarding the implementation and application, the main difficulty arises from the necessity of interfacing the fibers with peripheral devices. However, by selecting the right strategy for functionality, the number of contact points can be significantly reduced, comparing favorably to existing methods of arrays of 0-dimensional devices. A particularly interesting direction for future work is the detailed investigation of the interplay of sensing and actuation. Particularly when coupled with dedicated peripherals and optimized control algorithms, which reduce the required supervision for accomplishing desired tasks,

the technology could lead to truly ‘smart’ fibers and textiles.

Bibliography

1. Laschi, C., Mazzolai, B. & Cianchetti, M. Soft robotics: Technologies and systems pushing the boundaries of robot abilities. *Science Robotics* **1,** eaah3690 (2016).
2. Majidi, C. Soft Robotics: A Perspective—Current Trends and Prospects for the Future. *Soft Robotics* **1,** 5–11 (2014).
3. Rus, D. & Tolley, M. T. Design, fabrication and control of soft robots. *Nature* **521,** 467–475 (2015).
4. Whitesides, G. M. Soft Robotics. *Angewandte Chemie International Edition* **57,** 4258–4273 (2018).
5. Bayindir, M. *et al.* Metal–insulator–semiconductor optoelectronic fibres. *Nature* **431,** 826–829 (2004).
6. Yan, W. *et al.* Advanced Multimaterial Electronic and Optoelectronic Fibers and Textiles. *Advanced Materials* **31,** 1802348 (2019).
7. Xiong, J., Chen, J. & Lee, P. S. Functional Fibers and Fabrics for Soft Robotics, Wearables, and Human–Robot Interface. *Advanced Materials* **33,** 2002640 (2021).
8. Alexander Schmidt, M., Argyros, A. & Sorin, F. Hybrid Optical Fibers - An Innovative Platform for In-Fiber Photonic Devices. *Advanced Optical Materials* **4,** 13–36 (2016).
9. Qu, Y. *et al.* Superelastic Multimaterial Electronic and Photonic Fibers and Devices via Thermal Drawing. *Advanced Materials* **30,** 1707251 (2018).
10. Abouraddy, A. F. *et al.* Towards multimaterial multifunctional fibres that see, hear, sense and communicate. *Nature Materials* **6,** 336–347 (2007).
11. Page, A. G., Bechert, M., Gallaire, F. & Sorin, F. Unraveling radial dependency effects in fiber thermal drawing. *Applied Physics Letters* **115,** 044102 (2019).
12. Ida, N. *Sensors, Actuators, and their Interfaces: A Multidisciplinary Introduction* (SciTech Publishing, Edison, NJ, 2013).
13. Sorin, F., Lestoquoy, G., Danto, S., Joannopoulos, J. D. & Fink, Y. Resolving optical illumination distributions along an axially symmetric photodetecting fiber. *Optics express* **18,** 24264–75 (2010).
14. Romeo, A., Liu, Q., Suo, Z. & Lacour, S. P. Elastomeric substrates with embedded stiff platforms for stretchable electronics. *Applied Physics Letters* **102,** 131904 (2013).

15. Leber, A. *et al.* Compressible and Electrically Conducting Fibers for Large-Area Sensing of Pressures. *Advanced Functional Materials* **30,** 1904274 (2020).

16. Leber, A. *et al.* Soft and stretchable liquid metal transmission lines as distributed probes of multimodal deformations. *Nature Electronics* **3,** 316–326 (2020).

17. Mitschke, F. *Fiber Optics* (Springer Berlin Heidelberg, Berlin, Heidelberg, 2010).

18. Knight, J. C., Birks, T. A., Russell, P. S. J. & Atkin, D. M. All-silica single-mode optical fiber with photonic crystal cladding: errata. *Optics Letters* **22,** 484 (1997).

19. Nguyen-Dang, T. *et al.* Multi-material micro-electromechanical fibers with bendable functional domains. *Journal of Physics D: Applied Physics* **50,** 144001 (2017).

20. Yan, W. *et al.* Semiconducting Nanowire-Based Optoelectronic Fibers. *Advanced Materials* **29,** 1700681 (2017).

21. Khudiyev, T. *et al.* Electrostrictive microelectromechanical fibres and textiles. *Nature Communications* **8,** 1435 (2017).

22. Nguyen-Dang, T. *et al.* Controlled Sub-Micrometer Hierarchical Textures Engineered in Polymeric Fibers and Microchannels via Thermal Drawing. *Advanced Functional Materials* **27,** 1605935 (2017).

23. Koike, Y. *Fundamentals of Plastic Optical Fibers* (Wiley-VCH, 2015).

24. Berghmans, F., Geernaert, T., Baghdasaryan, T. & Thienpont, H. Challenges in the fabrication of fibre Bragg gratings in silica and polymer microstructured optical fibres. *Laser and Photonics Reviews* **8,** 27–52 (2014).

25. Nishii, J. *et al.* Recent advances and trends in chalcogenide glass fiber technology: a review. *Journal of Non-Crystalline Solids* **140,** 199–208 (1992).

26. Saad, M. Fluoride glass fiber: state of the art. *Fiber Optic Sensors and Applications VI* **7316,** 73160N (2009).

27. Zhang, J., Haas, R. M. & Leone, A. M. Polydispersity Characterization of Lipid Nanoparticles for siRNA Delivery Using Multiple Detection Size-Exclusion Chromatography. *Analytical Chemistry* **84,** 6088–6096 (2012).

28. Kalli, K. & Webb, D. J. in *Advanced Fiber Optics* 345–388 (2011).

29. Sordo, F. *et al.* Microstructured Fibers for the Production of Food. *Advanced Materials* **31,** 1807282 (2019).

30. Shadman, S. *et al.* Microstructured Biodegradable Fibers for Advanced Control Delivery. *Advanced Functional Materials* **30,** 1910283 (2020).

31. Yan, W. *et al.* Structured nanoscale metallic glass fibres with extreme aspect ratios. *Nature Nanotechnology* **15,** 875–882 (2020).

32. Guo, J., Niu, M. & Yang, C. Highly flexible and stretchable optical strain sensing for human motion detection. *Optica* **4,** 1285 (2017).

33. Egusa, S. *et al.* Multimaterial piezoelectric fibres. *Nature Materials* **9,** 643–648 (2010).

34. Benoit, G., Hart, S., Temelkuran, B., Joannopoulos, J. & Fink, Y. Static and Dynamic Properties of Optical Microcavities in Photonic Bandgap Yarns. *Advanced Materials* **15,** 2053–2056 (2003).

35. Bayindir, M., Abouraddy, A. F., Arnold, J., Joannopoulos, J. D. & Fink, Y. Thermal-sensing fiber devices by multimaterial codrawing. *Advanced Materials* **18,** 845–849 (2006).

36. Zhang, J. *et al.* Single-Crystal SnSe Thermoelectric Fibers via Laser-Induced Directional Crystallization: From 1D Fibers to Multidimensional Fabrics. *Advanced Materials* **32,** 2002702 (2020).

37. Danto, S., Ruff, Z., Wang, Z., Joannopoulos, J. D. & Fink, Y. Ovonic Memory Switching in Multimaterial Fibers. *Advanced Functional Materials* **21,** 1095–1101 (2011).

38. Taylor, G. F. A Method of Drawing Metallic Filaments and a Discussion of their Properties and Uses. *Physical Review* **23,** 655–660 (1924).

39. Guo, Y. *et al.* Polymer Composite with Carbon Nanofibers Aligned during Thermal Drawing as a Microelectrode for Chronic Neural Interfaces. *ACS Nano* **11,** 6574–6585 (2017).

40. Canales, A. *et al.* Multifunctional fibers for simultaneous optical, electrical and chemical interrogation of neural circuits in vivo. *Nature Biotechnology* **33,** 277–284 (2015).

41. Gorgutsa, S., Gu, J. F. & Skorobogatiy, M. A woven 2D touchpad sensor and a 1D slide sensor using soft capacitor fibers. *Smart Materials and Structures* **21,** 015010 (2012).

42. Knape, H. & Margulis, W. All-fiber polarization switch. *Optics Letters* **32,** 614 (2007).

43. Danto, S. *et al.* Fiber field-effect device via in situ channel crystallization. *Advanced Materials* **22,** 4162–4166 (2010).

44. Callister, W. D. & Rethwisch, D. G. *Materials science and engineering* (Wiley, Salt Lake City, 2011).

45. Drobny, J. G. *Handbook of thermoplastic elastomers* (PDL(Plastics Design Library)/William Andrew Pub., 2014).

46. Krehel, M., Rossi, R., Bona, G.-l. & Scherer, L. Characterization of Flexible Copolymer Optical Fibers for Force Sensing Applications. *Sensors* **13,** 11956–11968 (2013).

47. Bergström, J. *Mechanics of Solid Polymers* (Elsevier, Amsterdam, 2015).

48. Park, S. *et al.* Silicones for Stretchable and Durable Soft Devices: Beyond Sylgard-184. *ACS Applied Materials & Interfaces* **10,** 11261–11268 (2018).

49. Diani, J., Fayolle, B. & Gilormini, P. A review on the Mullins effect. *European Polymer Journal* **45,** 601–612 (2009).

50. Abraham, J. K., Sullivan, S. & Ranganathan, S. *Low-cost and disposable pressure sensor mat for non-invasive sleep and movement monitoring applications* in *2011 Annual International Conference of the IEEE Engineering in Medicine and Biology Society* (IEEE, 2011), 4745–4748.

51. Liu, J. J. *et al.* BreathSens: A Continuous On-Bed Respiratory Monitoring System with Torso Localization Using an Unobtrusive Pressure Sensing Array. *IEEE Journal of Biomedical and Health Informatics* **19,** 1682–1688 (2015).

52. Nishyama, M., Miyamoto, M. & Watanabe, K. Respiration and body movement analysis during sleep in bed using hetero-core fiber optic pressure sensors without constraint to human activity. *Journal of Biomedical Optics* **16,** 017002 (2011).

53. Xu, W., Huang, M. C., Amini, N., He, L. & Sarrafzadeh, M. ECushion: A textile pressure sensor array design and calibration for sitting posture analysis. *IEEE Sensors Journal* **13,** 3926–3934 (2013).

54. Costilla-Reyes, O., Scully, P. & Ozanyan, K. B. Temporal pattern recognition for gait analysis applications using an "intelligent carpet" system. *2015 Ieee Sensors* **16,** 1–4 (2015).

55. Holleczek, T., Ru, A., Harms, H. & Tro, G. *Textile pressure sensors for sports applications* in *2010 IEEE Sensors* (IEEE, 2010), 732–737.

56. Levi, A., Piovanelli, M., Furlan, S., Mazzolai, B. & Beccai, L. Soft, Transparent, Electronic Skin for Distributed and Multiple Pressure Sensing. *Sensors* **13,** 6578–6604 (2013).

57. Park, Y.-L., Tepayotl-Ramirez, D., Wood, R. J. & Majidi, C. Influence of cross-sectional geometry on the sensitivity and hysteresis of liquid-phase electronic pressure sensors. *Applied Physics Letters* **101,** 191904 (2012).

58. Gong, S. *et al.* A wearable and highly sensitive pressure sensor with ultrathin gold nanowires. *Nature Communications* **5,** 3132 (2014).

59. Lin, L. *et al.* Triboelectric Active Sensor Array for Self-Powered Static and Dynamic Pressure Detection and Tactile Imaging. *ACS Nano* **7,** 8266–8274 (2013).

60. Boutry, C. M. *et al.* A stretchable and biodegradable strain and pressure sensor for orthopaedic application. *Nature Electronics* **1,** 314–321 (2018).

61. Lipomi, D. J. *et al.* Skin-like pressure and strain sensors based on transparent elastic films of carbon nanotubes. *Nature Nanotechnology* **6,** 788–792 (2011).

62. Liu, M. *et al.* Large-Area All-Textile Pressure Sensors for Monitoring Human Motion and Physiological Signals. *Advanced Materials* **29,** 1703700 (2017).

63. Park, M., Park, J. & Jeong, U. Design of conductive composite elastomers for stretchable electronics. *Nano Today* **9,** 244–260 (2014).

64. Wang, L. & Cheng, L. Piezoresistive effect of a carbon nanotube silicone-matrix composite. *Carbon* **71,** 319–331 (2014).

65. Chen, Z. *et al.* Flexible Piezoelectric-Induced Pressure Sensors for Static Measurements Based on Nanowires/Graphene Heterostructures. *ACS Nano* **11,** 4507–4513 (2017).

66. Tao, X. *Handbook of Smart Textiles* (ed Tao, X.) (Springer Singapore, Singapore, 2015).

67. Leber, A., Cholst, B., Sandt, J., Vogel, N. & Kolle, M. Stretchable Thermoplastic Elastomer Optical Fibers for Sensing of Extreme Deformations. *Advanced Functional Materials* **29,** 1802629 (2018).

68. Rothmaier, M., Luong, M. P. & Clemens, F. Textile Pressure Sensor Made of Flexible Plastic Optical Fibers. *Sensors* **8,** 4318–4329 (2008).

69. Zhao, H., O'Brien, K., Li, S. & Shepherd, R. F. Optoelectronically innervated soft prosthetic hand via stretchable optical waveguides. *Science Robotics* **1,** eaai7529 (2016).

70. Li, Y. & Shimizu, H. Toward a Stretchable, Elastic, and Electrically Conductive Nanocomposite: Morphology and Properties of Poly[styrene-b-(ethylene-co-butylene)-b-styrene]/Multiwalled Carbon Nanotube Composites Fabricated by High-Shear Processing. *Macromolecules* **42,** 2587–2593 (2009).

71. Zhu, S. *et al.* Ultrastretchable Fibers with Metallic Conductivity Using a Liquid Metal Alloy Core. *Advanced Functional Materials* **23,** 2308–2314 (2013).

72. Zang, Y., Zhang, F., Di, C.-a. & Zhu, D. Advances of flexible pressure sensors toward artificial intelligence and health care applications. *Materials Horizons* **2,** 140–156 (2015).

73. Zeng, H., Zhao, Y., Zeng, H. & Zhao, Y. Sensing Movement: Microsensors for Body Motion Measurement. *Sensors* **11,** 638–660 (2011).

74. Zhang, C., Ma, C.-A., Wang, P. & Sumita, M. Temperature dependence of electrical resistivity for carbon black filled ultra-high molecular weight polyethylene composites prepared by hot compaction. *Carbon* **43,** 2544–2553 (2005).

75. Kenedi, R. M. & Cowden, J. M. *Bed Sore Biomechanics* (The Macmillan Press, 1976).

76. Hohlfeld, E. & Mahadevan, L. Scale and Nature of Sulcification Patterns. *Physical Review Letters* **109,** 025701 (2012).

77. Gao, Y. *et al.* Wearable Microfluidic Diaphragm Pressure Sensor for Health and Tactile Touch Monitoring. *Advanced Materials* **29,** 1701985 (2017).

78. Yamada, T. *et al.* A stretchable carbon nanotube strain sensor for human-motion detection. *Nature Nanotechnology* **6,** 296–301 (2011).

79. Atalay, A. *et al.* Batch Fabrication of Customizable Silicone-Textile Composite Capacitive Strain Sensors for Human Motion Tracking. *Advanced Materials Technologies* **2,** 1700136 (2017).

80. Gerratt, A. P., Michaud, H. O. & Lacour, S. P. Elastomeric Electronic Skin for Prosthetic Tactile Sensation. *Advanced Functional Materials* **25,** 2287–2295 (2015).

81. Thuruthel, T. G., Shih, B., Laschi, C. & Tolley, M. T. Soft robot perception using embedded soft sensors and recurrent neural networks. *Science Robotics* **4,** eaav1488 (2019).

82. Amjadi, M., Kyung, K. U., Park, I. & Sitti, M. Stretchable, Skin-Mountable, and Wearable Strain Sensors and Their Potential Applications: A Review. *Advanced Functional Materials* **26,** 1678–1698 (2016).

83. An, B. W., Heo, S., Ji, S., Bien, F. & Park, J. U. Transparent and flexible fingerprint sensor array with multiplexed detection of tactile pressure and skin temperature. *Nature Communications* **9,** 1–10 (2018).

84. Li, Q. *et al.* Large-Strain, Multiform Movements from Designable Electrothermal Actuators Based on Large Highly Anisotropic Carbon Nanotube Sheets. *ACS Nano* **9,** 409–418 (2015).

85. Park, J. J., Hyun, W. J., Mun, S. C., Park, Y. T. & Park, O. O. Highly Stretchable and Wearable Graphene Strain Sensors with Controllable Sensitivity for Human Motion Monitoring. *ACS Applied Materials & Interfaces* **7,** 6317–6324 (2015).

86. Pruvost, M., Smit, W. J., Monteux, C., Poulin, P. & Colin, A. Polymeric foams for flexible and highly sensitive low-pressure capacitive sensors. *npj Flexible Electronics* **3** (2019).

87. Amjadi, M., Pichitpajongkit, A., Lee, S., Ryu, S. & Park, I. Highly Stretchable and Sensitive Strain Sensor Based on Silver Nanowire–Elastomer Nanocomposite. *ACS Nano* **8,** 5154–5163 (2014).

88. Choi, S. *et al.* Highly conductive, stretchable and biocompatible Ag–Au core–sheath nanowire composite for wearable and implantable bioelectronics. *Nature Nanotechnology* **13,** 1048–1056 (2018).

89. Chen, S., Lou, Z., Chen, D., Jiang, K. & Shen, G. Polymer-Enhanced Highly Stretchable Conductive Fiber Strain Sensor Used for Electronic Data Gloves. *Advanced Materials Technologies* **1,** 1–9 (2016).

90. Park, J. *et al.* Giant Tunneling Piezoresistance of Composite Elastomers with Interlocked Microdome Arrays for Ultrasensitive and Multimodal Electronic Skins. *ACS Nano* **8,** 4689–4697 (2014).

91. Chen, Z., Xi, J., Huang, W. & Yuen, M. M. F. Stretchable conductive elastomer for wireless wearable communication applications. *Scientific Reports* **7,** 10958 (2017).

92. Shintake, J., Piskarev, E., Jeong, S. H. & Floreano, D. Ultrastretchable Strain Sensors Using Carbon Black-Filled Elastomer Composites and Comparison of Capacitive Versus Resistive Sensors. *Advanced Materials Technologies* **3,** 1700284 (2018).

93. Zhou, J., Xu, X., Xin, Y. & Lubineau, G. Coaxial Thermoplastic Elastomer-Wrapped Carbon Nanotube Fibers for Deformable and Wearable Strain Sensors. *Advanced Functional Materials* **28,** 1705591 (2018).

94. Abdullah, S. A., Iqbal, A. & Frormann, L. Melt mixing of carbon fibers and carbon nanotubes incorporated polyurethanes. *Journal of Applied Polymer Science* **110,** 196–202 (2008).

95. Sang, Z., Ke, K. & Manas-Zloczower, I. Effect of carbon nanotube morphology on properties in thermoplastic elastomer composites for strain sensors. *Composites Part A: Applied Science and Manufacturing* **121,** 207–212 (2019).

96. Bilotti, E., Zhang, R., Deng, H., Baxendale, M. & Peijs, T. Fabrication and property prediction of conductive and strain sensing TPU/CNT nanocomposite fibres. *Journal of Materials Chemistry* **20,** 9449 (2010).

97. Probst, H. *et al.* Melt Spinning of Highly Stretchable, Electrically Conductive Filament Yarns. *Polymers* **13,** 590 (2021).

98. Christ, J. F., Aliheidari, N., Ameli, A. & Pötschke, P. 3D printed highly elastic strain sensors of multiwalled carbon nanotube/thermoplastic polyurethane nanocomposites. *Materials & Design* **131,** 394–401 (2017).

99. Dong, C. *et al.* High-efficiency super-elastic liquid metal based triboelectric fibers and textiles. *Nature Communications* **11,** 3537 (2020).

100. Stråat, M., Toll, S., Boldizar, A., Rigdahl, M. & Hagström, B. Melt spinning of conducting polymeric composites containing carbonaceous fillers. *Journal of Applied Polymer Science* **119,** 3264–3272 (2011).

101. Alig, I., Skipa, T., Lellinger, D. & Pötschke, P. Destruction and formation of a carbon nanotube network in polymer melts: Rheology and conductivity spectroscopy. *Polymer* **49,** 3524–3532 (2008).

102. Nilsson, E., Rigdahl, M. & Hagström, B. Electrically conductive polymeric bi-component fibers containing a high load of low-structured carbon black. *Journal of Applied Polymer Science* **132,** 1–9 (2015).

103. Zhang, Q. *et al.* Use of Dynamic Rheological Behavior to Estimate the Dispersion of Carbon Nanotubes in Carbon Nanotube/Polymer Composites. *The Journal of Physical Chemistry B* **112,** 12606–12611 (2008).

104. Saphiannikova, M., Skipa, T., Lellinger, D., Alig, I. & Heinrich, G. Superposition approach for description of electrical conductivity in sheared MWNT/polycarbonate melts. *Express Polymer Letters* **6,** 438–453 (2012).

105. Gupta, T. D., Gacoin, T. & Rowe, A. C. H. Piezoresistive Properties of Ag/Silica Nano-Composite Thin Films Close to the Percolation Threshold. *Advanced Functional Materials* **24,** 4522–4527 (2014).

106. Luheng, W., Tianhuai, D. & Peng, W. Influence of carbon black concentration on piezoresistivity for carbon-black-filled silicone rubber composite. *Carbon* **47,** 3151–3157 (2009).

107. Niu, S. *et al.* A wireless body area sensor network based on stretchable passive tags. *Nature Electronics* **2,** 361–368 (2019).

108. Jung, S. *et al.* Wearable Fall Detector using Integrated Sensors and Energy Devices. *Scientific Reports* **5,** 1–9 (2015).

109. Welch, Harnett & Lee. A Review on Measuring Affect with Practical Sensors to Monitor Driver Behavior. *Safety* **5,** 72 (2019).

110. Markvicka, E. J., Bartlett, M. D., Huang, X. & Majidi, C. An autonomously electrically self-healing liquid metal–elastomer composite for robust soft-matter robotics and electronics. *Nature Materials* **17,** 618–624 (2018).

111. Atalay, O., Kennon, W. R. & Demirok, E. Weft-Knitted Strain Sensor for Monitoring Respiratory Rate and Its Electro-Mechanical Modeling. *IEEE Sensors Journal* **15,** 110–122 (2015).

112. Xu, P. A. *et al.* Optical lace for synthetic afferent neural networks. *Science Robotics* **4,** eaaw6304 (2019).

113. Cooper, C. B. *et al.* Stretchable Capacitive Sensors of Torsion, Strain, and Touch Using Double Helix Liquid Metal Fibers. *Advanced Functional Materials* **27,** 1605630 (2017).

114. Yan, W. *et al.* Thermally drawn advanced functional fibers: New frontier of flexible electronics. *Materials Today* **35,** 168–194 (2020).

115. Furse, C., Chung, Y. C., Lo, C. & Pendayala, P. A critical comparison of reflectometry methods for location of wiring faults. *Smart Structures and Systems* **2,** 25–46 (2006).

116. Smail, M. K., Pichon, L., Olivas, M., Auzanneau, F. & Lambert, M. Detection of Defects in Wiring Networks Using Time Domain Reflectometry. *IEEE Transactions on Magnetics* **46,** 2998–3001 (2010).

117. Zhou, Z., Jiao, T., Zhao, P., Liu, J. & Xiao, H. Development of a Distributed Crack Sensor Using Coaxial Cable. *Sensors* **16,** 1198 (2016).

118. Dowding, C., Su, M. & O'Connors, K. Principles of time domain reflectometometry applied to measurement of rock mass deformation. *International Journal of Rock Mechanics and Mining Sciences & Geomechanics Abstracts* **25,** 287–297 (1988).

119. Dominauskas, A., Heider, D. & Gillespie, J. W. Electric time-domain reflectometry distributed flow sensor. *Composites Part A: Applied Science and Manufacturing* **38,** 138–146 (2007).

120. Roelvink, J., Trabelsi, S. & Nelson, S. O. A planar transmission-line sensor for measuring the microwave permittivity of liquid and semisolid biological materials. *IEEE Transactions on Instrumentation and Measurement* **62,** 2974–2982 (2013).

121. Lin, M. W., Thaduri, J. & Abatan, A. O. Development of an electrical time domain reflectometry (ETDR) distributed strain sensor. *Measurement Science and Technology* **16,** 1495–1505 (2005).

122. Tang, L., Tao, X. & Choy, C. L. Possibility of using a coaxial cable as a distributed strain sensor by time domain reflectometry. *Smart Materials and Structures* **10,** 221–228 (2001).

123. Jung, Y. H. *et al.* Stretchable Twisted-Pair Transmission Lines for Microwave Frequency Wearable Electronics. *Advanced Functional Materials* **26,** 4635–4642 (2016).

124. Wimmer, R. & Baudisch, P. *Modular and deformable touch-sensitive surfaces based on time domain reflectometry* in *UIST'11 - Proceedings of the 24th Annual ACM Symposium on User Interface Software and Technology* (2011), 517–526.

125. Hayes, G. J. *et al.* Microfluidic coaxial transmission line and phase shifter. *Microwave and Optical Technology Letters* **56,** 1459–1462 (2014).

126. Xu, D., Tairych, A. & Anderson, I. A. Localised strain sensing of dielectric elastomers in a stretchable soft-touch musical keyboard. **943025,** 943025 (2015).

127. Zhou, W. & Wang, Z. L. *Scanning Microscopy for Nanotechnology* (2007).

128. Dickey, M. D. Stretchable and Soft Electronics using Liquid Metals. *Advanced Materials* **29,** 1606425 (2017).

129. Hammond, F. L., Kramer, R. K., Wan, Q., Howe, R. D. & Wood, R. J. Soft tactile sensor arrays for force feedback in micromanipulation. *IEEE Sensors Journal* **14,** 1443–1452 (2014).

130. Majidi, C., Kramer, R. & Wood, R. J. A non-differential elastomer curvature sensor for softer-than-skin electronics. *Smart Materials and Structures* **20,** 105017 (2011).

131. Park, Y.-L., Majidi, C., Kramer, R., Bérard, P. & Wood, R. J. Hyperelastic pressure sensing with a liquid-embedded elastomer. *Journal of Micromechanics and Microengineering* **20,** 125029 (2010).

132. Yeo, J. C. *et al.* Triple-State Liquid-Based Microfluidic Tactile Sensor with High Flexibility, Durability, and Sensitivity. *ACS Sensors* **1,** 543–551 (2016).

133. Strickland, J. A., Zimmerman, H. A., Long, G. & Frye, G. *Time-domain Reflectometry Measurements* (Tektronix, Beaverton, 1970).

134. Cataldo, A., De Benedetto, E. & Cannazza, G. *Broadband Reflectometry for Enhanced Diagnostics and Monitoring Applications* (Springer Berlin Heidelberg, Berlin, Heidelberg, 2011).

135. Zandvakili, M., Honari, M. M., Mousavi, P. & Sameoto, D. Gecko-Gaskets for Multilayer, Complex, and Stretchable Liquid Metal Microwave Circuits and Antennas. *Advanced Materials Technologies* **2,** 1700144 (2017).

136. Mohsen-Nia, M., Amiri, H. & Jazi, B. Dielectric Constants of Water, Methanol, Ethanol, Butanol and Acetone: Measurement and Computational Study. *Journal of Solution Chemistry* **39,** 701–708 (2010).

137. Pozar, D. M. *Microwave Engineering* (John Wiley & Sons, Inc., 2012).

138. Rogers, J. A., Ghaffari, R. & Kim, D.-H. *Stretchable Bioelectronics for Medical Devices and Systems* (eds Rogers, J. A., Ghaffari, R. & Kim, D.-H.) (Springer International Publishing, Cham, 2016).

139. Wadell, B. C. *Transmission line design handbook* 513 (Artech House, 1991).

140. Ball, J. Characteristic impedance of unbalanced TDR probes. *IEEE Transactions on Instrumentation and Measurement* **51,** 532–536 (2002).

141. Collier, R. J. *Transmission lines : equivalent circuits, electromagnetic theory, and photons* (Cambridge University Press, 2013).

142. Kaiser, K. L. *Transmission lines, matching, and crosstalk* (Taylor & Francis, 2006).

143. Overvelde, J. T. *et al.* Mechanical and electrical numerical analysis of soft liquid-embedded deformation sensors analysis. *Extreme Mechanics Letters* **1,** 42–46 (2014).

144. Lee, T. H. *Planar Microwave Engineering* (Cambridge University Press, 2004).

145. Wagenaars, P., A. F. Wouters, P., J. M. Van Der Wielen, P. & Steennis, E. Approximation of transmission line parameters of single-core and three-core XLPE cables. *IEEE Transactions on Dielectrics and Electrical Insulation* **17,** 106–115 (2010).

146. Kharraz, M. A. O. *et al. Experimental characterization of outdoor low voltage cables for narrowband power line communication* in *2016 International Symposium on Power Line Communications and its Applications (ISPLC)* (IEEE, 2016), 138–143.

147. Jolaei, M., Hooshiar, A., Dargahi, J. & Packirisamy, M. Toward Task Autonomy in Robotic Cardiac Ablation: Learning-Based Kinematic Control of Soft Tendon-Driven Catheters. *Soft Robotics,* soro.2020.0006 (2020).

148. Paek, J., Cho, I. & Kim, J. Microrobotic tentacles with spiral bending capability based on shape-engineered elastomeric microtubes. *Scientific Reports* **5,** 10768 (2015).

149. Lindenroth, L., Duriez, C., Back, J., Rhode, K. & Liu, H. *Intrinsic force sensing capabilities in compliant robots comprising hydraulic actuation* in *2017 IEEE/RSJ International Conference on Intelligent Robots and Systems (IROS)* **2017-Septe** (IEEE, 2017), 2923–2928.

150. Gul, J. Z., Yang, Y. J., Su, K. Y. & Choi, K. H. Omni Directional Multimaterial Soft Cylindrical Actuator and Its Application as a Steerable Catheter. *Soft Robotics* **4,** 224–240 (2017).

151. Ji, X. *et al.* An autonomous untethered fast soft robotic insect driven by low-voltage dielectric elastomer actuators. *Science Robotics* **4,** eaaz6451 (2019).

152. Kim, Y., Parada, G. A., Liu, S. & Zhao, X. Ferromagnetic soft continuum robots. *Science Robotics* **4,** eaax7329 (2019).

153. Cianchetti, M., Laschi, C., Menciassi, A. & Dario, P. Biomedical applications of soft robotics. *Nature Reviews Materials* **3,** 143–153 (2018).

154. Hines, L., Petersen, K., Lum, G. Z. & Sitti, M. Soft Actuators for Small-Scale Robotics. *Advanced Materials* **29** (2017).

155. Webster, R. J. & Jones, B. A. Design and Kinematic Modeling of Constant Curvature Continuum Robots: A Review. *The International Journal of Robotics Research* **29,** 1661–1683 (2010).

156. Martinez, R. V. *et al.* Robotic tentacles with three-dimensional mobility based on flexible elastomers. *Advanced Materials* **25,** 205–212 (2013).

157. Muramatsu, Y., Kobayashi, T. & Konishi, S. Flexible end-effector integrated with scanning actuator and optical waveguide for endoscopic fluorescence imaging diagnosis. *Proceedings of the IEEE International Conference on Micro Electro Mechanical Systems (MEMS)* **2015-Febru,** 166–167 (2015).

158. Kashyap, V. *et al.* Multilayer fabrication of durable catheter-deployable soft robotic sensor arrays for efficient left atrial mapping. *Science Advances* **6,** eabc6800 (2020).

159. Fusco, S. *et al.* Shape-Switching Microrobots for Medical Applications: The Influence of Shape in Drug Delivery and Locomotion. *ACS Applied Materials & Interfaces* **7,** 6803–6811 (2015).

160. Burgner-Kahrs, J., Rucker, D. C. & Choset, H. Continuum Robots for Medical Applications: A Survey. *IEEE Transactions on Robotics* **31,** 1261–1280 (2015).

161. Hu, X., Chen, A., Luo, Y., Zhang, C. & Zhang, E. Steerable catheters for minimally invasive surgery: a review and future directions. *Computer Assisted Surgery* **23,** 21–41 (2018).

162. Runciman, M., Darzi, A. & Mylonas, G. P. Soft Robotics in Minimally Invasive Surgery. *Soft Robotics* **6,** 423–443 (2019).

163. Cho, S., Lee, E., Jo, S., Kim, G. M. & Kim, W. Extrusion Characteristics of Thin Walled Tubes for Catheters Using Thermoplastic Elastomer. *Polymers* **12,** 1628 (2020).

164. Jin, G.-B., Wang, M.-J., Zhao, D.-Y., Tian, H.-Q. & Jin, Y.-F. Design and experiments of extrusion die for polypropylene five-lumen micro tube. *Journal of Materials Processing Technology* **214,** 50–59 (2014).

165. Gorissen, B., De Volder, M. & Reynaerts, D. Chip-on-tip endoscope incorporating a soft robotic pneumatic bending microactuator. *Biomedical Microdevices* **20,** 73 (2018).

166. Ikuta, K., Ichikawa, H., Suzuki, K. & Yajima, D. Multi-degree of freedom hydraulic pressure driven safety active catheter. *Proceedings - IEEE International Conference on Robotics and Automation* **2006,** 4161–4166 (2006).

167. Tan, N., Gu, X. & Ren, H. Design, characterization and applications of a novel soft actuator driven by flexible shafts. *Mechanism and Machine Theory* **122,** 197–218 (2018).

168. Stilli, A., Wurdemann, H. A. & Althoefer, K. Shrinkable, stiffness-controllable soft manipulator based on a bio-inspired antagonistic actuation principle. *IEEE International Conference on Intelligent Robots and Systems,* 2476–2481 (2014).

169. Qi, F., Ju, F., Bai, D., Wang, Y. & Chen, B. Kinematic analysis and navigation method of a cable-driven continuum robot used for minimally invasive surgery. *International Journal of Medical Robotics and Computer Assisted Surgery* **15** (2019).

170. Dalvand, M. M., Nahavandi, S. & Howe, R. D. An Analytical Loading Model for n-Tendon Continuum Robots. *IEEE Transactions on Robotics* **34,** 1215–1225 (2018).

Curriculum Vitae

ANDREAS LEBER

Lausanne 1003, Switzerland
+41 21 693 2907
andreas.leber@epfl.ch

andreas-leber

Andreas Leber

PROFILE

Extensive scientific background and experienced in driving cross-disciplinary R&D projects from early conception all the way to implementation. Developer of mechanical, electronic, and optical systems by leveraging materials properties. Communication skills founded on a trilingual education in English, French, and German in four countries.

Date of birth	20/08/1992
Nationality	German, Swiss resident permit B since 2017
Civil Status	Single

Scientific interests: mechanics, optics, electronics, sensors, actuators, functional materials, soft materials, polymers, composites, multi-material fibers, large-scale processing, smart skins and textiles, robotics, medical devices

EDUCATION

- **École polytechnique fédérale de Lausanne (EPFL), Switzerland** PhD in Materials Science | expected in 2021
- **University of Erlangen-Nuremberg (FAU), Germany** MS (Hons) in Materials and Chemical Engineering | 2017
- **Oregon State University (OSU), USA** BS in Mechanical Engineering (Double Bachelor Atlantis) | 2014
- **Saarland University (UdS), Germany** BS in Materials Science (Double Bachelor Atlantis) | 2013

RESEARCH EXPERIENCE

École polytechnique fédérale de Lausanne (EPFL), Switzerland | PhD research | since 09/2017

Developed the materials and fabrication methodology for a new generation of soft functional fibers.
Conceived mechanical sensing techniques based on the materials, structure, or electrical signaling.
Created fully integrated solutions for industrial partners involving smart textiles for Internet-of-Things.
Supervised 6 semester projects and 1 master's thesis, and published several high-impact papers.
My research led to a successful grant application valued at > CHF 100,000 for the transfer of technology.

Massachusetts Institute of Technology (MIT), USA | Master's thesis and subsequent work | 09/2016 - 07/2017

Developed an extrusion process for the fabrication of elastic optical fiber at large scale and low cost.
Created sensors based on the optical fibers and implemented them in health monitoring prototypes.
The publication of my project was recognized by a cover page in the journal Advanced Functional Materials.

University of Erlangen-Nuremberg, Germany | Semester projects during master's studies | 04/2015 - 03/2016

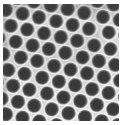

Institute of Particle Technology: Fabricated ordered nanohole metal films through colloidal lithography and characterized the optical transmission and electrical conductivity.

Institute of Biomaterials: Optimized the fabrication of chitosan/bioactive glass composite coatings by electrophoretic deposition and characterized the degradation and drug delivery functionality.

Saarland University, Germany | Bachelor's thesis | 04/2013 - 08/2013

Investigated the synergy of two friction-reducing methods applied to nickel: the reinforcement with carbon nanotubes and the patterning of the surface by means of interfering laser beams.
Characterized the composite materials by SEM, FIB, EBSD, and Raman spectroscopy.

Fraunhofer Institute for Non-destructive Testing, Germany | Inspection Robotics assistant | 07/2011 - 04/2013

Oversaw the data processing of 3 other assistants, successfully completing 2 infrastructure inspection pilots.
Developed an adaptive structure for an unmanned aerial vehicle with optimized aerodynamics based on genetic algorithm, FEA, and CFD, with the goal to increase inspection speed.

ADDITIONAL EXPERIENCE

- Stryker Corporation, Germany | Advanced Operations Craniomaxillofacial intern | 04/2016 - 09/2016

Studied the technical and economic feasibility of the anodization process of a new titanium implant.
Developed monitoring methods for the process, raising interest across several plants.
Initiated a collaborative project with Stryker France on anodization, including a two-week stay at the plant in Bordeaux.

- Oregon State University, USA | Global Formula Racing team member | 09/2013 - 08/2014

Designed and tested the carbon fiber sandwich structure of the monocoque of the car according to requirements of high mechanical integrity and low weigth.
Defended the chassis design to judges at the Formula Student competition 2014 at the Red Bull Ring.
Our team won 4 international Formula Student competitions involving hundreds of universities.

SELECTED HONORS AND AWARDS

2021 Best Talk Award at the EPFL EDMX research day ("Soft fibers for mechanical sensing").
Appearance in radio interview with RTS ("La vie secrète des matériaux").
Among top 5 EPFL PhD students and PostDocs selected for the Global Young Scientist Summit.

2020 Work highlighted in several news outlets, including EPFL News ("Smart textiles powered by soft transmission lines") and 20min ("Des textiles intelligents capables de fournir des données sur notre corps").

2019 Poster Award at the EPFL EDMX research day ("Pressure-sensing fibers").

2018 Cover page in Advanced Functional Materials ("Stretchable optical fibers").

2017 Poster Award at the International Congress Engineering of Advanced Materials in Erlangen ("Stretchable optical fibers")
SPIE Best Thesis Award at FAU ("Stretchable optical fibers").

2016 Scholarship of the German Academic Exchange Service (DAAD PROMOS) for master's thesis at MIT.
Linn Award for highest grade point average of master's program at FAU.

2014 Drucilla Shepard Smith Award for 4.00 grade point average at OSU.

SELECTED PUBLICATIONS

1. **A. Leber**, C. Dong, R. Chandran, T. Das Gupta, N. Bartolomei & F. Sorin, "Soft and stretchable liquid metal transmission lines as distributed probes of multimodal deformations" *Nat. Electron.* 3, 316–326 (2020).
2. C. Dong, **A. Leber**, T. Das Gupta, R. Chandran, M. Volpi, Y. Qu, T. Nguyen-Dang, N. Bartolomei, W. Yan & F. Sorin, "High-efficiency super-elastic liquid metal based triboelectric fibers and textiles" *Nat. Commun.* 11, 1–9 (2020).
3. S. Shadman, T. Nguyen-Dang, T. Das Gupta, A. G. Page, I. Richard, **A. Leber**, J. Ruza, G. Krishnamani & F. Sorin "Micro-structured Biodegradable Fibers for Advanced Control Delivery" *Adv. Funct. Mater.* 1910283, 1–9 (2020).
4. **A. Leber**, A. G. Page, D. Yan, Y. Qu, S. Shadman, P. Reis & F. Sorin "Compressible and Electrically Conducting Fibers for Large-Area Sensing of Pressures" *Adv. Funct. Mater.* 30, 1904274 (2020).
5. **A. Leber**, B. Cholst, J. Sandt, N. Vogel & M. Kolle "Stretchable Thermoplastic Elastomer Optical Fibers for Sensing of Extreme Deformations" *Adv. Funct. Mater.* 29, 1802629 (2018).

SELECTED CONFERENCES

Global Young Scientists Summit in Singapore (2021).
Materials Research Society Fall Meeting in Boston, USA (2019 and 2020).
Boston Photonics Centennial Conference in Cambridge, USA (2017).
International Micro Air Vehicle Conference and Flight Competition in Braunschweig, Germany (2012).

REVIEWER DUTIES

Advanced Optical Materials
Advanced Engineering Materials
Light: Science & Applications

LANGUAGES

ENGLISH bilingual - C2

FRENCH bilingual - C2

GERMAN native

SKILLS

Design	Mechanics/ electronics, prototyping, analysis, CAD, FEA
Materials	Selection, characterization, processing, polymers, metals
Characterization	mechanical, electrical, Rheometer, DMA, SEM, FIB, EBSD, AFM, Raman, UV Vis spectroscopy, FTIR, optical profilometer
Manufacturing	Extrusion, 3D printing, standard machining, surface treatments
Programming	General-purpose: Python, data analysis: Matlab, firmware: C++